

# Active Disturbance Rejection Control: Applications, Stability Analysis, and Tuning Method

By

**Zhengrong Chu**

A thesis submitted to the Faculty of Graduate Studies in partial fulfillment of the  
requirements for the degree of

**Doctor of Philosophy**

Department of Mechanical Engineering

The University of Manitoba

© Copyright 2018 by Zhengrong Chu

# Abstract

Active disturbance rejection control (ADRC), an emerging control technique, not only has a simple control structure but also has the advantage of being robust against plant uncertainties and external disturbances. In this thesis, the application of the ADRC is extended to two new areas: automated steering control for lane keeping in autonomous vehicles, and position control of hydraulic actuators. The thesis addresses two challenges in the above applications. The first is the stability analysis of the vehicle system controlled by the ADRC. Because the vehicle model is nonlinear and complex, using Lyapunov's second method to study the stability is challenging. The second challenge is the tuning of the ADRC for controlling hydraulic actuators. It is found that the ADRC tuned by the widely used bandwidth tuning method cannot provide the desired tracking performance of hydraulic actuators. To solve these challenges, the concept of Lyapunov exponents is used to investigate the stability of the ADRC system, and the quantitative feedback theory (QFT) is adopted in a novel manner to tune the ADRC for the position control of hydraulic actuators.

With respect to the automated steering controller design, the models describing the vehicle dynamics are first developed. Second, the ADRC steering controller is designed and the stability of the ADRC system is investigated using the concept of Lyapunov exponents. Third, simulations and experiments are conducted to validate the effectiveness of the ADRC controller. It is shown that the vehicle controlled by the ADRC controller

performs the lane keeping successfully. The ADRC controller is simple, without requiring complex calculations and real-time measurements, and it is easy to implement in practice.

On the position controller design for the two hydraulic actuators, including the electro-hydrostatic actuator and the electro-hydraulic actuator, the ADRC is first transformed from the state space to the frequency domain. Then, the decomposed controller and prefilter are tuned in the framework of the QFT to meet the prescribed design specifications for reference tracking and stability. Both the simulation and experimental results demonstrate that the actuators track the desired positions closely. The proposed tuning method for the ADRC provides an easy-to-use and effective tool for controller design in practical applications.

*To My Family*

# Acknowledgments

I would like to thank my advisor, Dr. Christine Wu, for her support and guidance during my Ph. D. study at the Nonlinear Systems Research Laboratory. Dr. Wu provided me a very comfortable learning and research environment. She offered me a number of opportunities to practice my communication and presentation skills. Whatever problems I confronted in life or in research, she was always ready to be my great and strongest supporter. I am deeply grateful for her trust and encouragement.

I sincerely appreciate my co-advisor, Dr. Nariman Sepehri, for his constructive advice and support on my research. Dr. Sepehri gave me a valuable opportunity to work in the Fluid Power and Telerobotics Laboratory, which broadened my research experience and made me have a deeper understanding of control theory and applications. Discussions with him were always the source of my inspirations.

I wish to express my sincere appreciation to my internal examiners, Dr. Balakrishnan and Dr. Annakkage, and my external examiner, Dr. Yang Shi, for their careful review, comments, and suggestions to my research. I also would like to thank all my lab mates for creating this warm and comfortable environment. I thank Dr. Yuming Sun of Mechanical Engineering and Paul White of Computer Engineering for their valuable help on my research.

Last, I express my deepest gratitude to my parents and brother. Without their love and support, this wonderful journey can only be imagined. I thank my wife for joining me in this unforgettable journey. Her love and support are the source of my motivation. Thank you for being with me.

# Table of Content

<b>Abstract.....</b>	<b>I</b>
<b>Acknowledgments .....</b>	<b>IV</b>
<b>Table of Content.....</b>	<b>V</b>
<b>List of Figures.....</b>	<b>VII</b>
<b>List of Tables .....</b>	<b>XI</b>
<b>Nomenclature .....</b>	<b>XII</b>
<b>Chapter 1 Introduction .....</b>	<b>1</b>
<b>Chapter 2 Literature Review.....</b>	<b>6</b>
2.1 Steering Control of Autonomous Vehicles.....	6
2.2 Position Control of Hydraulic Actuators .....	8
2.3 Overview of Active Disturbance Rejection Control (ADRC).....	10
2.4 Stability Analysis of ADRC System .....	12
2.5 Tuning of ADRC .....	13
<b>Chapter 3 Mathematical Preliminaries .....</b>	<b>16</b>
3.1 Active Disturbance Rejection Control.....	16
3.2 Linear Active Disturbance Rejection Control .....	20
3.3 Concept of Lyapunov Exponents .....	24
3.4 Calculation of Lyapunov Exponents Based on Model .....	26
3.5 Quantitative Feedback Theory (QFT) .....	28
<b>Chapter 4 Automated Steering Control for Vehicle Lane Keeping.....</b>	<b>34</b>
4.1 Vehicle Model .....	34
4.1.1 Nonlinear Vehicle model .....	34
4.1.2 Linear Vehicle Model .....	38
4.2 Controller Design .....	40
4.3 Stability Analysis.....	43

4.4	Simulations .....	45
4.5	Experimental Validation.....	48
4.5.1	Experimental Setup .....	48
4.5.2	Experimental Results .....	63
4.6	Summary.....	68
<b>Chapter 5</b>	<b>Position Control of Hydraulic Actuators .....</b>	<b>70</b>
5.1	Quantitative Feedback Theory Design of ADRC.....	70
5.1.1	Laplace Transform of ADRC.....	70
5.1.2	Tuning of ADRC.....	74
5.2	Position Control of Electro-Hydrostatic Actuator.....	75
5.2.1	Controller Design .....	77
5.2.2	Bounded-Input Bounded-Output Stability .....	81
5.2.3	Simulations and Experiments.....	83
5.3	Position Control of Electro-Hydraulic Actuator.....	89
5.3.1	Controller Design .....	90
5.3.2	Simulations and Experiments.....	93
5.4	Summary.....	97
<b>Chapter 6</b>	<b>Conclusions .....</b>	<b>99</b>
6.1	Contributions of This Thesis .....	99
6.2	Future Work.....	101
<b>References</b>	<b>.....</b>	<b>103</b>

# List of Figures

Figure 2.1 Automated steering for lane keeping in autonomous vehicles [39] .....	8
Figure 2.2 Position control of hydraulic actuators: (a) electro-hydrostatic actuator; (b) electro-hydraulic actuator .....	9
Figure 2.3 Two applications of hydraulic actuators: (a) aircraft; (b) excavator .....	9
Figure 3.1 Block diagram of ADRC .....	17
Figure 3.2 Block diagram of linear ADRC .....	21
Figure 3.3 Evolution of two-dimensional dynamic system .....	25
Figure 3.4 Orthonormalization for $\delta x_1^j$ and $\delta x_2^j$ of the two-dimensional sphere at the jth integration step .....	28
Figure 3.5 Two degree-of-freedom feedback system .....	28
Figure 3.6 QFT bounds, the initial and acceptable nominal open-loop transfer functions in the Nichols chart .....	31
Figure 3.7 Effect of the prefilter $H(s)$ on the frequency responses of the closed-loop transfer function (1: $ GP(jw)/(1 + GP(jw)) $ ), 2: $ HGP(jw)/(1 + GP(jw)) $ ) .....	33
Figure 4.1 Four-wheel nonlinear vehicle model .....	35
Figure 4.2 Look-ahead sensing estimation .....	38
Figure 4.3 Two-wheel linear vehicle model .....	39
Figure 4.4 Steering control system for lane keeping .....	40
Figure 4.5 Time histories of Lyapunov exponents .....	44
Figure 4.6 State trajectories converging to the equilibrium points .....	45
Figure 4.7 Simulations of the ADRC system with parameter variations and external disturbances: (a) overall view; (b) handling of the initial condition; (c) effect of the wind force; (d) effect of the road curvature during the cornering .....	47
Figure 4.8 1/5th scaled vehicle .....	49
Figure 4.9 Remote controller and automatic/manual switch .....	52
Figure 4.10 Circuit for switching control signals between the software and the user ...	52



Figure 4.11 Flow charts of the automated steering control for lane keeping: (a) scheme A; (b) scheme B .....	53
Figure 4.12 Voltage regulator circuit.....	55
Figure 4.13 Power supply diagram for the retrofitted scaled vehicle .....	55
Figure 4.14 Steering mechanism of the scaled vehicle.....	56
Figure 4.15 3D model of the steering mechanism in the scaled vehicle .....	57
Figure 4.16 Web browser-based user interface .....	58
Figure 4.17 High-level system software overview .....	58
Figure 4.18 Backend software architecture .....	59
Figure 4.19 Retrofitted scaled vehicle: (a) adopting scheme A; (b) adopting scheme B .....	60
Figure 4.20 Arrangement of the line sensors underneath the beams in scheme A.....	61
Figure 4.21 Hardware diagram of the retrofitted scaled vehicle using computer vision.....	63
Figure 4.22 Estimation of the road centerline via computer vision in the experiment..	63
Figure 4.23 Lane keeping performances of the scaled vehicle controlled by the ADRC controller and the PID controller on path one.....	65
Figure 4.24 Lane keeping performances of the scaled vehicle controlled by the ADRC controller and the PID controller on path two ( $\rho=0.04 \text{ m}^{-1}$ ) .....	67
Figure 4.25 Lane keeping performances of the scaled vehicle controlled by the ADRC controller and the PID controller on path three ( $\rho=0.05 \text{ m}^{-1}$ ) .....	67
Figure 4.26 Steering angle, lateral acceleration and yaw rate of the scaled vehicle controlled by the ADRC controller during lane keeping on path three ( $v_x=9 \text{ km/h}$ , $\rho=0.05 \text{ m}^{-1}$ ) .....	68
Figure 4.27 Straight and curved lane keeping results and each subfigure contains five separate tests conducted a period of time: (a) straight lane keeping; (b) curved lane keeping ( $\rho=0.04 \text{ m}^{-1}$ ); (c) curved lane keeping ( $\rho=0.05 \text{ m}^{-1}$ ) ...	69
Figure 5.1 Test bed: (a) electro-hydrostatic circuit; (b) electro-hydraulic circuit; (c) hydraulic actuator .....	75
Figure 5.2 Schematic of the EHA.....	76
Figure 5.3 Templates of the EHA model at selected frequencies.....	78

Figure 5.4	Bounds $B(w)$ , and the acceptable nominal open-loop transfer functions $L_n(s)$ for the fourth-order ADRC (solid line) and the second-order ADRC (dash-dotted) .....	79
Figure 5.5	Frequency responses of the control system with parametric uncertainties ..	80
Figure 5.6	Step responses of the control system with parameter variations in the simulations: (a) fourth-order ADRC tuned by the proposed tuning method; (b) second-order ADRC tuned by the proposed tuning method; (c) fourth-order ADRC tuned by the bandwidth tuning method ( $w_o=75$ rad/s, $w_c=71$ rad/s) .....	84
Figure 5.7	Pole-zero maps of the ADRC control system (with parameter variations) tuned by the bandwidth tuning method: (a) $w_o=75$ rad/s, $w_c=71$ rad/s; (b) partial enlargement of (a); (c) $w_o=76$ rad/s, $w_c=71$ rad/s; (d) partial enlargement of (c). .....	85
Figure 5.8	Experimental responses of 0.01 m square-wave reference against 125 kN/m spring and increasing leakage flow: (a) position; (b) control signal; (c) leakage rate. (Solid line: fourth-order ADRC tuned by the proposed tuning method; dashed: second-order ADRC tuned by the proposed tuning method; dash-dotted: fault-tolerant controller) .....	87
Figure 5.9	Partial enlargements of the position responses shown in Figure 5.8 (a): (a) fourth-order ADRC tuned by the proposed tuning method; (b) second-order ADRC tuned by the proposed tuning method; (c) fault-tolerant controller. ....	88
Figure 5.10	Schematic of the electro-hydraulic actuator .....	89
Figure 5.11	Templates of the model of the electro-hydraulic actuator at selected frequencies .....	91
Figure 5.12	Bounds $B(w)$ and the acceptable nominal open-loop transfer function $L_n(s)$ .....	92
Figure 5.13	Frequency responses of the control system with parametric uncertainties ..	92
Figure 5.14	Step responses of the control system with parameter variations in simulations: (a) third-order ADRC tuned by the proposed tuning method; (b) fifth-order ADRC tuned by the bandwidth tuning method ( $w_o=4000$ rad/s, $w_c=210$ rad/s) .....	94

Figure 5.15 Step responses of the control system with nominal parameter values in simulations: (a) step response; (b) partial enlargement of (a); (c) control signal; (d) partial enlargement of (c). (Solid line: third-order ADRC tuned by the proposed tuning method; dashed: fifth-order ADRC tuned by the bandwidth tuning method, $w_o=4000$ rad/s, $w_c=210$ rad/s; dash-dotted: fifth-order ADRC tuned by the bandwidth tuning method, $w_o=4100$ rad/s, $w_c=215$ rad/s) .....	95
Figure 5.16 Experimental responses of 0.01 m square-wave reference against 125 kN/m spring and increasing leakage flow: (a) position; (b) control signal; (c) leakage rate. (Solid line: third-order ADRC tuned by the proposed tuning method; dashed: fault-tolerant controller) .....	96
Figure 5.17 Partial enlargements of the position responses shown in Figure 5.16 (a): (a) third-order ADRC tuned by the proposed tuning method; (b) fault-tolerant controller .....	97

## List of Tables

Table 4.1 Vehicle parameters and nominal values used in stability analysis and simulations .....	36
Table 4.2 Lyapunov exponents pertaining to the nonlinear vehicle system controlled by the ADRC steering controller .....	44
Table 4.3 Parameter variations in six simulations .....	46
Table 4.4 Electronic devices used for sensing and controlling in the scale vehicle .....	51
Table 4.5 Additional electronics needed for the look-ahead sensing systems .....	54
Table 4.6 Specifications of paths used in the experiments: straight lane keeping (Path one); curved lane keeping (Paths two and three).....	64
Table 5.1 Parameters of the EHA model .....	77
Table 5.2 Parameters of the model of the electro-hydraulic actuator .....	90

# Nomenclature

$m$	Mass
$I_z$	Vertical inertial moment
$L$	Distance from the look-ahead point to the center of gravity (CG)
$\rho$	Road curvature
$f_w$	Wind force
$l_w$	Position of the wind force
$l_f$	Distance from the front axis to the CG
$l_r$	Distance from the rear axis to the CG
$s_b$	Wheel-base width
$b_i$	Magic Formula parameter
$c_i$	Magic Formula parameter
$d_i$	Magic Formula parameter
$e_i$	Magic Formula parameter
$c_f$	Cornering stiffness of the front wheel
$c_r$	Cornering stiffness of the rear wheel
$n_t$	Tire-road length contact
$v_x$	Longitudinal velocity
$v_y$	Lateral velocity
$r$	Yaw rate
$f_{x_i}$	Longitudinal force of the $i$ th tire
$f_{y_i}$	Lateral force of the $i$ th tire
$\alpha_i$	Sideslip angle of the $i$ th tire
$v_i$	Absolute velocity of the $i$ th wheel
$\delta$	Steering angle of the front wheels
$y_L$	Lateral offset between the vehicle and the road centerline at the look-ahead point
$\varepsilon_L$	Angle between the tangent to the road and the longitudinal axis of the vehicle at the look-ahead point.

# Chapter 1

## Introduction

As a general theory for design, analysis, and implementation of feedback control systems, control theory has undergone tremendous development over the last few decades. Classical control theory deals with single-input and single-output systems and provides useful tools such as the Bode plot and Nyquist criterion to design and analyze control systems in the frequency domain [1]. In contrast, modern control theory applies to the state space. Because state space models provide a more complete description of dynamic systems [2], modern control theory not only deals with multiple-input and multiple-output systems, but also introduces performance and robustness specifications into the control analysis and synthesis [1, 3]. On the basis of modern control theory, a series of nonlinear control strategies have been developed to explicitly deal with nonlinearities in the mathematical models of dynamic systems; these include the Lyapunov stability method, sliding mode control, and adaptive control.

Despite the profusion of newly emerging strategies in modern control theory, the classical proportional-integral-derivative (PID) control, first proposed by Minorsky in 1922, is still dominant in over 90% of industrial applications [4]. The relatively simple

structure of the PID controller and the well-established methods for tuning the controller parameters explain why PID control is still extensively used by control engineers [5].

A PID controller is normally designed empirically and a mathematical model of the dynamic system is not necessarily required [4]. On the contrary, in order to be robust against plant uncertainties and external disturbances, the controller design in modern control theory requires detailed mathematical models. The reliance on accurate models provides great insight into how and why the control system works. However, for many systems, owing to a lack of knowledge of certain physical properties, obtaining detailed mathematical models is challenging. In addition, some techniques used in modern control theory, such as real-time system identification, optimization, and measurements of external disturbances, are difficult to implement in practice. Therefore, a question must be asked: Is there a control method that not only tolerates plant uncertainties and attenuates external disturbances, but also maintains the simplicity of the classical PID control?

Active disturbance rejection control (ADRC), based on the extended state observer (ESO), is believed to be an answer to the above question [6-10]. Within the framework of modern control theory, the ADRC is a further development of PID control, aiming at retaining its simplicity and overcoming its limitations [10]. The ADRC actively estimates and compensates for plant uncertainties and external disturbances. It is simple and easy to implement in practical applications, as well as being robust against unmodeled physical properties and external disturbances. In this thesis, for the first time, the ADRC is employed to two areas: automated steering control for vehicle lane keeping, and position control of hydraulic actuators.

In recent years, the ever-growing needs of driving safety, energy-saving, and environmental protection have greatly promoted the development of autonomous vehicles (also called self-driving cars) [11]. Among various techniques used in autonomous vehicles, automated steering control for lane keeping is an important component and has been studied for decades [11-25]. When designing a steering controller, one should consider that the lane keeping performance is easily influenced by plant uncertainties and external disturbances. Plant uncertainties usually come from parameter variations and unmodeled vehicle dynamics. External disturbances include wind forces, road adhesion, and road surface conditions. Furthermore, when implementing a steering controller for a vehicle, one should consider the system reliability and ease of use. Generally, a simple control algorithm that requires fewer measurements and calculations improves the system reliability and is easier to implement in practice. Therefore, owing to its simple and robust properties, the ADRC is a great potential candidate for steering controller design.

In the design of the ADRC steering controller for lane keeping, the stability analysis of the nonlinear vehicle system controlled by the ADRC controller is challenging. Lyapunov's second method, as a general stability analysis method, has been used to study the stabilities of ADRC systems [26-28]. However, as there is no constructive rule for Lyapunov functions, these stability analyses are limited to generalized justifications of the convergences of ADRC systems in which specific models of the dynamic systems are not required. That is, for a specific system, a stability analysis of the ADRC system is unable to determine whether it could be stabilized by a set of controller parameters. Therefore, to address the problem, the concept of Lyapunov exponents is used to



investigate the stability of a nonlinear vehicle system controlled by an ADRC steering controller.

Another focus of this thesis is the application of the ADRC to the position control of hydraulic actuators. Hydraulic actuators are driven by pressurized hydraulic fluid. They have been widely used in vehicles, vessels, airplanes, construction and manufacturing tools. In practice, hydraulic actuators can suffer from various faults caused by the failure of components [29]. In particular, a failure of the piston seal that causes internal leakage between the two chambers reduces the position control precision of the actuator [30]. Plant uncertainties and varying external loads acting on the actuator also affect the tracking performance of the actuator. Therefore, to improve the reliability and availability, the position control strategy must be robust against faults, plant uncertainties and external load variation [31]. Based on the ESO, the ADRC applied to the position control of hydraulic actuators is capable of actively estimating and compensating for faults and plant uncertainties.

The bandwidth tuning method is widely used in tuning the controller and observer gains of the ADRC [32-34]. It ensures the stability of the control system and works well for tuning the ADRC applied to first- and second-order systems [32]. However, for the position control of hydraulic actuators described by high-order systems, the bandwidth tuning method is found to be conservative [33], i.e., the tracking specification cannot be satisfied. Obviously, there is a need to develop a practical method to tune the ADRC for high-order systems. The aim is to ensure that both the stability and tracking requirements are met. The quantitative feedback theory (QFT) has been shown to be an effective tool

in designing controllers under certain design specifications [35-38]. There is potential to use this technique for tuning the ADRC applied to high-order systems.

Given the above discussions, the objectives of this thesis are threefold. The first objective is to design the ADRC steering controller for lane keeping. The steering controller must be reliable and easy-to-use in practice. The second objective is to investigate the stability of the ADRC system. The stability analysis is able to determine whether a set of gains of the ADRC can stabilize the control system. The third objective is to develop a methodology to tune the ADRC for the position control of hydraulic actuators. The ADRC tuned by the proposed tuning method must meet the stability and desired tracking specifications.

This thesis is organized as follows. In Chapter 2, the literature regarding steering control of autonomous vehicles, position control of hydraulic actuators, development of the ADRC, stability analysis of the ADRC control system, and tuning of the ADRC is reviewed. In Chapter 3, mathematical preliminaries related to the ADRC, concept and calculation method of Lyapunov exponents, and QFT are given. In Chapter 4, the ADRC is applied to automated steering control for lane keeping in autonomous vehicles. The stability of the ADRC system is investigated using the concept of Lyapunov exponents. Both simulations and experiments are conducted to validate the effectiveness of the ADRC steering controller. Chapter 5 describes the application of the ADRC to the position control of hydraulic actuators. A tuning method is proposed to tune the ADRC in the frequency domain. Both simulations and experiments are performed to validate the effectiveness of the ADRC position controllers. In Chapter 6, conclusions outlining the contributions of the thesis and future work are presented.

# Chapter 2

## Literature Review

In this chapter, a literature review of steering control of autonomous vehicles, position control of hydraulic actuators, development of the ADRC, stability analysis of the ADRC system, and tuning of the ADRC, is conducted. The problems addressed in this thesis are also formulated.

### **2.1 Steering Control of Autonomous Vehicles**

The automated steering control for lane keeping is one of the important components used in autonomous vehicles. The aim is to keep the vehicle within the designated lane, as shown in Figure 2.1. Various steering control methods have been developed in the past two decades [11-25]. A steering control method that consists of a nonlinear damping controller and an augmented observer was developed in [12]. This method is robust against vehicle uncertainties, but the controller structure is complicated and tuning a large number of controller parameters is required. A state feedback controller based on a linear quadratic regulator was proposed to minimize the errors between the estimated vehicle states and desired vehicle states [13]. Online optimization and measurements of the

vehicle states are needed in this method. A steering control method was developed to control the steering of both the front and rear axles simultaneously [14]. Rear axle steering is beneficial to the lane keeping performance but is not a practical solution for most vehicles. A steering controller based on a sliding-mode observer and super-twisting algorithm was proposed for heavy vehicles [15]. This method was not experimentally validated. A steering control approach based on a linear matrix inequality and bilinear matrix inequality was proposed to constrain the vehicle states within the prescribed limits [16]. This approach requires an accurate system identification of the vehicle. A fuzzy steering controller was proposed in [11], which performs well but is heuristic owing to a lack of stability proof [17]. Adaptive and  $H$ -infinity steering controllers were developed in [17]. These two controllers function well; however, the structure of the adaptive controller is complicated, and the  $H$ -infinity controller requires the precise vehicle model [17]. In [18, 19], a nested PID control method was developed for lane keeping by synchronously regulating the yaw rate and the lateral offset. The numerous parameters of the PID controllers were tuned by trial and error, which causes difficulty in practical applications. A lead-lag steering controller was proposed in [20], which was validated experimentally but requires estimation of the road curvature. In [21], a PD steering controller combined with a second-order lead-compensator was designed using a look-down sensing system. This controller is simple, but the look-down sensing system is less practical than the look-ahead sensing system. A steering control method that coupled the vehicle to the environment [22], and methods that used the magnet-magnetometer system to estimate the lateral offset [23-25], are difficult to implement in practice.

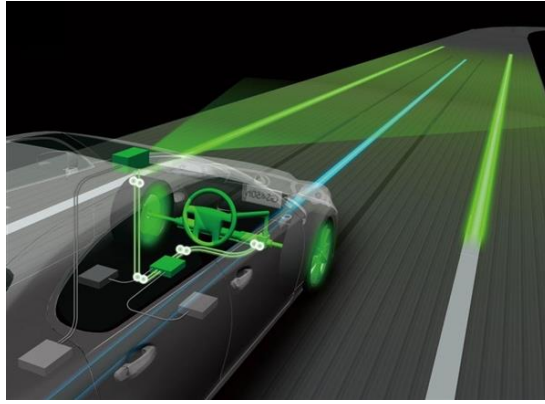


Figure 2.1 Automated steering for lane keeping in autonomous vehicles [39]

From the above literature review, it is evident that a steering controller that requires fewer measurements and calculations as well as being robust against vehicle uncertainties and external disturbances, improves the system reliability and is easier to implement in practice. In the aforementioned control methods, the PID control is easy to implement owing to its simple structure, but it presents the largest errors [17]. Other methods are robust but require either quite a few measurements or complex calculations, which increase the difficulties in practical implementations and reduce the system reliability. Therefore, there is a need for a steering controller that has simple structure while is robust against to vehicle uncertainties and external disturbances.

## 2.2 Position Control of Hydraulic Actuators

The goal of position control of hydraulic actuators is to track the desired positions of the actuators, as shown in Figure 2.2. Two typical applications of hydraulic actuators are shown in Figure 2.3. Over the last few decades, to improve the reliability and availability of hydraulic actuators, two different strategies have been developed to deal with faults occurring in hydraulic actuators, namely, the fault detection and isolation (FDI) and fault-

tolerant control (FTC) strategies. The FDI strategy is useful for signaling abnormal faulty behavior and assisting in troubleshooting of hydraulic actuators [40, 41]. However, they are incapable of maintaining the desired system performance in the presence of faults. In contrast, the FTC strategy aims at tolerating the faults of hydraulic actuators and maintaining the system performance within an acceptable range, as well as being robust against plant uncertainties [31]. Various techniques have been proposed to develop fault-tolerant controllers, such as observer-based control [42], sliding mode control [43], fuzzy predictive control [44], and QFT.

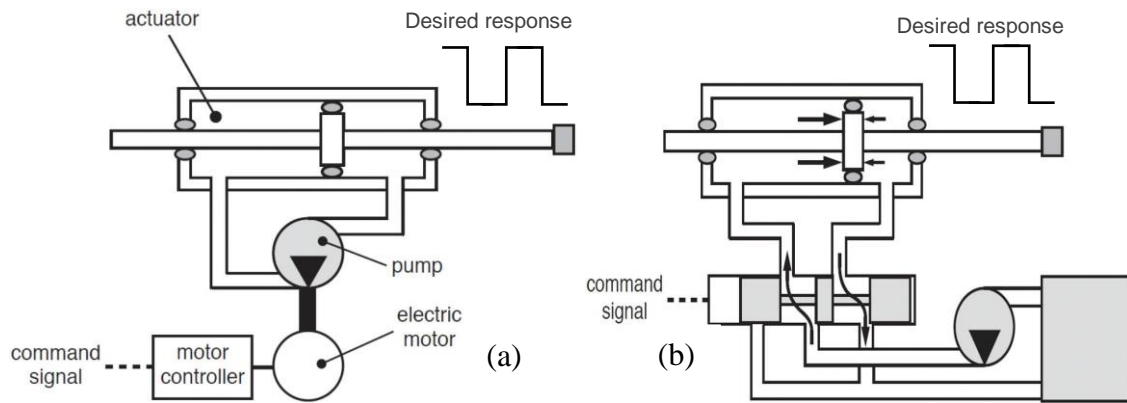


Figure 2.2 Position control of hydraulic actuators: (a) electro-hydrostatic actuator; (b) electro-hydraulic actuator

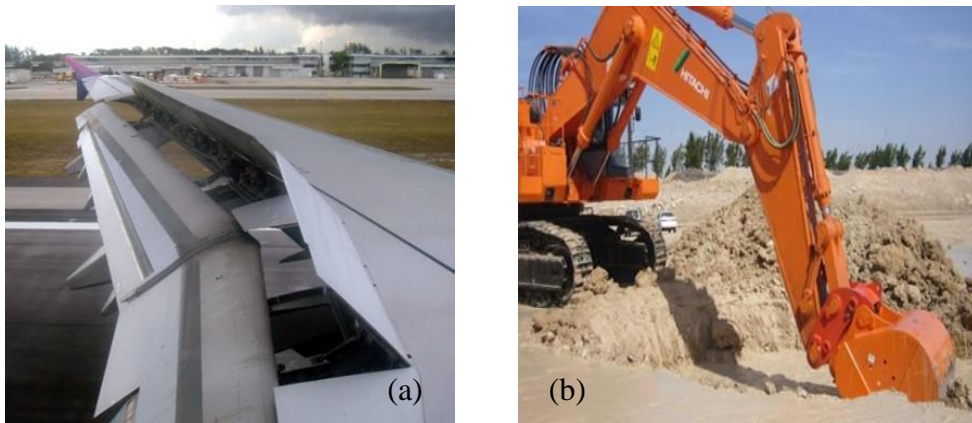


Figure 2.3 Two applications of hydraulic actuators: (a) aircraft; (b) excavator

The QFT is a theory devoted to designing robust controllers despite plant uncertainties owing to faults or unknown dynamics. It provides an effective way to maintain balance between controller complexity and system performance. With respect to the development of fault-tolerant controllers in the QFT framework, a position controller [29] and a pressure controller [30] were developed for an electro-hydraulic actuator experiencing internal leakage. Two position controllers based on the QFT were designed for an electro-hydraulic actuator with faulty actuator position leakage [31, 45]. A QFT-based force controller was designed for a hydraulic system with system and environmental uncertainties [37]. A self-tuning strategy was proposed for the QFT-based force and position control of an electro-hydraulic actuator [46, 47]. The above literature illustrates the effectiveness of the QFT strategies for the tolerance of faults and plant uncertainties. However, within the QFT framework, the controllers are designed by adding poles and zeros. Because of the lack of a constructive rule to determine the structure of the controller, the design process is based on experience. Therefore, having a predetermined controller structure could accelerate the controller design process and be beneficial for industrial applications.

### **2.3 Overview of Active Disturbance Rejection Control (ADRC)**

The ADRC was originally proposed by Han [6-10] twenty years ago and has attracted more and more research attention in recent years. It is a combination of the state observer in modern control theory and the classical PID control. It consists of three parts: transient profile generator (TPG), nonlinear weighted sum (NWS), and extended state observer

(ESO) [10]. The TPG generates a transient profile for the plant to follow according to the desired system response. The ESO estimates plant uncertainties and external disturbances in real-time. The NWS employs a nonlinear combination of the errors between the transient profiles and the outputs of the ESO. The significant difference between the ADRC and other control methods is that the ADRC not only estimates plant uncertainties and external disturbances in the ESO, but also actively compensates for them in the NWS. Therefore, the ADRC becomes a potential candidate for controlling dynamic systems with plant uncertainties and external disturbances. The ADRC has been applied to a two-mass drive system [5], a magnetic rodless pneumatic cylinder [26], a flywheel energy storage system [48], and a compliant micro-/nanopositioning piezostage with dual mode [49].

However, owing to the usage of nonlinear functions in all three parts of the ADRC, the complicated controller structure and a large number of tuning parameters pose challenges in practical applications. To simplify the structure of the ADRC, a linear ADRC was proposed in [32], where the TPG is removed and the nonlinear functions used in the ESO and NWS are replaced by linear functions. To date, the application of the linear ADRC has been widely extended to many different fields, such as disturbance decoupling control [28], tandem control of a laboratory helicopter [50], voltage stabilization control in open-cathode fuel cells [51], internal permanent-magnet synchronous motor control [52, 53], underactuated control of vehicle lateral path tracking [54], steering control by wire haptic systems [55], MEMS gyroscopes [56], and trajectory tracking control of the Delta robot [57]. More developments of the ADRC can be seen in [58-68].



## 2.4 Stability Analysis of ADRC System

Generally, when a closed-loop control system is linear, the stability can be easily analyzed by determining the eigenvalues of the control system. All the eigenvalues that have negative real parts indicate that the control system is stable. When the control system is nonlinear, Lyapunov's second method is the most general method to study the stability. In [26], the stabilities of the nonlinear ESO and the ADRC system were analyzed based on Lyapunov's second method. It was shown that: 1) there exist appropriate observer gains, the estimation errors between the ESO and the system states are convergent; 2) there exist proper gains of the NWS, the ADRC system is stable, i.e., the estimation errors between the transient profiles and the system outputs are convergent. Similarly, the stability analyses of the linear ESO and the ADRC system based on Lyapunov's second method were presented in [27, 28]. It was shown that there exist appropriate gains of the linear ESO and the linear weighted sum, the linear ESO and the ADRC system are stable, and the estimation errors are bounded.

The aforementioned stability analyses based on Lyapunov's second method are the generalized justifications of the convergences of the ADRC systems, where the models of the controlled systems are not required. However, for a specific controlled system, these generalized justifications are unable to determine whether a set of gains of the ADRC controller can stabilize the controlled system. The main reason why there is no stability justification of the ADRC for a specific, controlled system can be attributed to the fact that constructing the Lyapunov functions for nonlinear and complex dynamic systems is very challenging, because no constructive rule exists in the Lyapunov stability

theory. Therefore, to address this challenge, an alternative means to study the stability of the ADRC system is desirable.

In this thesis, the concept of Lyapunov exponents, as a powerful tool for the stability analyses of complicated and nonlinear dynamic systems, is introduced to investigate the stability of the ADRC system consisting of a nonlinear vehicle model. The Lyapunov exponents describe the long-term evolution of a dynamic system with an initial condition [69]. The signs of the Lyapunov exponents describe the stability property of the dynamic system [70]. Compared to Lyapunov's second method, the methods for calculating the Lyapunov exponents are constructive, either based on a model of the dynamic system or a time series [71]. The concept of Lyapunov exponents has been applied to the stability analyses of the PD control for a biped [72-74] and a nonlinear vehicle model in plane motion [75, 76].

## **2.5 Tuning of ADRC**

The linearization of the nonlinear ADRC generates a simple control structure and reduces the number of tuning parameters. Within the framework of the linear ADRC, the number of tuning parameters  $n_t$  is proportional to the order of the dynamic system  $n$ :  $n_t=2n+1$  [34]. That is, for a second-order dynamic system, the number of tuning parameters is five. To further facilitate the tuning process, a bandwidth tuning method was proposed to reduce the number of tuning parameters to two, i.e., the observer bandwidth and the controller bandwidth [32]. This is realized by expressing all parameters of the linear ESO as functions of the observer bandwidth, and expressing all

parameters of the linear weighted sum as functions of the controller bandwidth. Most applications of the ADRC mentioned above were based on this tuning method.

The bandwidth tuning method ensures the stability of the ADRC system and works well for tuning the ADRC for controlled systems described by first- and second-order mathematical models [32]. However, it is found to be conservative in tuning the ADRC for controlling hydraulic actuators described by fourth- and fifth-order systems, because a large number of tuning parameters determined by only two bandwidths cannot meet the desired tracking performance [33]. There has been little research on tuning the ADRC. In [34], a tuning method similar to the bandwidth tuning method was proposed. In [33], a method was proposed by incorporating the known system dynamics into the ADRC. This method works for systems for which accurate models are available but not for complicated systems with plant uncertainties and faults.

In order to address the difficulties when tuning the ADRC for controlling hydraulic actuators, a tuning method is developed in the frequency domain. In this method, the ADRC is first decomposed into two parts: the controller and the prefilter. Then, the controller and prefilter are tuned in the framework of the QFT. With the aid of the QFT, the proposed tuning method considers the plant uncertainties during the tuning stage and tunes the ADRC in the frequency domain according to the reference tracking and the stability specifications. This gives a new tool to practitioners to design suitable robust controllers for hydraulic actuators and also extends the application of the ADRC to high-order systems.

An analysis of a second-order ADRC in the frequency domain was presented in [77]. The idea was applied to the analysis of an electric-power-assisted steering system in [78]. However, the focus of these studies was limited to the performance analysis of the ADRC system in the frequency domain, and the parameters were tuned by the bandwidth tuning method.

# Chapter 3

## Mathematical Preliminaries

In this chapter, the mathematical preliminaries of the ADRC, concept and calculation method of Lyapunov exponents, and QFT, which are the fundamental components of knowledge for this thesis, are presented.

### 3.1 Active Disturbance Rejection Control

The ADRC consists of three parts: the transient profile generator (TPG), nonlinear weighted sum (NWS), and extended state observer (ESO) [10, 26]. As shown in Figure 3.1, the TPG is used to generate continuous smooth profiles for the controlled system to follow to avoid sudden jumps of the control signal. The ESO is used to estimate the internal dynamics and external disturbances in real-time. The NWS is used to apply a nonlinear combination of the errors between the outputs of the ESO and the profiles.

Consider the dynamic system represented by the following equation:

$$\ddot{y}(t) = F(y(t), u(t), d(t)) + bu(t) \quad (3.1)$$

where  $y$  is the system response,  $u$  is the control signal,  $b$  is the control signal gain, and  $d$  is an external disturbance.  $F$ , considered as the generalized disturbance, is a multivariable function of the internal dynamics and the external disturbance.

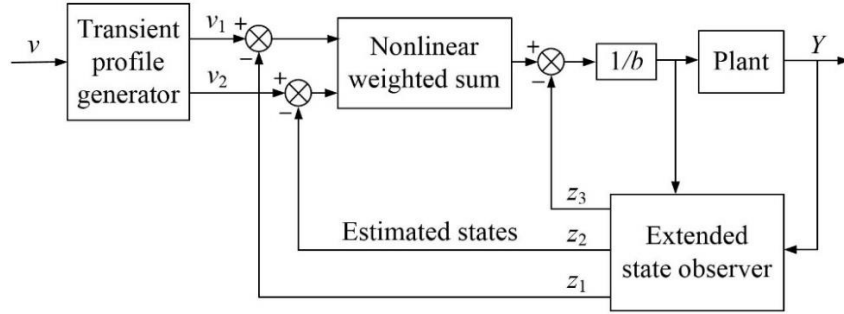


Figure 3.1 Block diagram of ADRC

Let  $x_1 = y$ ,  $x_2 = \dot{x}_1$ , and  $x_3 = F$ . Assuming that  $F$  is differentiable and  $h = \dot{F}$ , (3.1)

can be expressed in the state space form:

$$\begin{cases} \dot{x}_1 = x_2 \\ \dot{x}_2 = x_3 + bu \\ \dot{x}_3 = h \end{cases} \quad (3.2)$$

with the system state  $x = [x_1, x_2, x_3]^T$  and  $x_3$  being the argument state.

Considering  $v$  as the reference input, the TPG is designed to generate smooth profiles for the controlled system to follow:

$$\begin{cases} \dot{v}_1 = v_2 \\ \dot{v}_2 = fhan(\eta, v_2, r_0, h_0) \end{cases} \quad (3.3)$$

where  $v_1$  and  $v_2$  are the output profiles of the TPG. In the function  $fhan(\bullet)$ ,  $\eta = v_1 - v$ ;

$r_0$  and  $h_0$  are parameters. The function  $fhan(\bullet)$  is defined as [10]:

$$fhan(\eta, v_2, r_0, h_0) = -r_0 a g_2 / d - r_0 \text{sign}(a)(1 - g_2) \quad (3.4)$$

where

$$\begin{cases} d = r_0 h_0^2, a_0 = h_0 v_2, a_1 = \eta + a_0 \\ a_2 = \sqrt{d(d + 8|a_1|)} \\ a_3 = a_0 + \text{sign}(a_1)(a_2 - d) / 2 \\ g_1 = \text{sign}(a_1 + d) / 2 - \text{sign}(a_1 - d) / 2 \\ a = (a_0 + a_1)g_1 + a_3(1 - g_1) \\ g_2 = \text{sign}(a + d) / 2 - \text{sign}(a - d) / 2 \end{cases}$$

Because there is no constructive tuning method, tuning the parameters  $r_0$  and  $h_0$  is mostly based on experience [26]. Generally,  $r_0$  and  $h_0$  can be tuned individually according to the desired tracking performance [10].

The ESO for (3.2) can be designed as:

$$\begin{cases} \dot{z}_1 = z_2 + l_1 e \\ \dot{z}_2 = z_3 + l_2 \text{fal}(e, \sigma_1, \delta_1) + bu \\ \dot{z}_3 = l_3 \text{fal}(e, \sigma_2, \delta_2) \end{cases} \quad (3.5)$$

where  $e = x_1 - z_1$ .  $l_1$ ,  $l_2$ , and  $l_3$  are the observer gains.  $\sigma_1$ ,  $\sigma_2$ ,  $\delta_1$ , and  $\delta_2$  are the parameters of the function  $\text{fal}(\bullet)$ . With properly tuned observer gains and parameters of  $\text{fal}(\bullet)$ , the observer states  $z_1$ ,  $z_2$ , and  $z_3$  track the system states  $x_1$ ,  $x_2$ , and  $x_3$ , respectively. The function  $\text{fal}(\bullet)$  is defined as [10]:

$$\text{fal}(e, \sigma, \delta) = \begin{cases} e / \delta^{1-\sigma}, & |e| \leq \delta \\ |e|^\sigma \text{sign}(e), & |e| > \delta \end{cases} \quad (3.6)$$

where  $\sigma$  is within the range of  $(0, 1)$ , and  $\delta$  is a multiple of the sampling period [10]. The sampling period depends on the specific system. Note that for the linear ADRC presented in the following section  $fal(\bullet)$  is replaced by a linear function.

The NWS is designed as:

$$u = \frac{-z_3 + k_1 fal(e_1, \sigma_3, \delta_3) + k_2 fal(e_2, \sigma_4, \delta_4)}{b} \quad (3.7)$$

where  $e_1 = v_1 - z_1$  and  $e_2 = v_2 - z_2$ .  $k_1$  and  $k_2$  are the controller gains.  $\sigma_3$ ,  $\sigma_4$ ,  $\delta_3$ , and  $\delta_4$  are the parameters of the function  $fal(\bullet)$ .

Substituting (3.7) into (3.1), we have:

$$\ddot{y} = F - z_3 + k_1 fal(e_1, \sigma_3, \delta_3) + k_2 fal(e_2, \sigma_4, \delta_4) \quad (3.8)$$

The result of  $(F - z_3)$  is negligible if the ESO is tuned properly [28]. Therefore, (3.8) can be written as:

$$\ddot{y} \approx k_1 fal(e_1, \sigma_3, \delta_3) + k_2 fal(e_2, \sigma_4, \delta_4) \quad (3.9)$$

In summary, combining the ESO, NWS and TPG, the second-order ADRC is given as:

$$\left\{ \begin{array}{l} \text{ESO:} \\ \dot{z}_1 = z_2 + l_1 e \\ \dot{z}_2 = z_3 + l_2 fal(e, \sigma_1, \delta_1) + bu \\ \dot{z}_3 = l_3 fal(e, \sigma_2, \delta_2) \\ \text{NWS:} \\ u = \frac{-z_3 + k_1 fal(e_1, \sigma_3, \delta_3) + k_2 fal(e_2, \sigma_4, \delta_4)}{b} \\ \text{TPG:} \\ \dot{v}_1 = v_2 \\ \dot{v}_2 = fhan(\eta, v_2, r_0, h_0) \end{array} \right.$$



Similar to the tuning of the TPG, because there is no constructive tuning method, the parameters of the ESO and NWS are tuned by trial and error in order to obtain the best system response. This is done by giving a set of initial parameter values; if the system response is not acceptable, the parameter values should be adjusted such that a better system response is obtained. This tuning process continues until the optimal system response is achieved.

### 3.2 Linear Active Disturbance Rejection Control

Owing to the usage of nonlinear functions in all three parts of the ADRC, the complicated control structure and large number of tuning parameters cause difficulties in practical applications. To simplify the ADRC, the linear ADRC was proposed by Gao in [32]. The linear ADRC can be easily extended to  $n$ th-order systems. Consider the dynamic system represented by the following equation:

$$y^{(n)}(t) = F(y(t), u(t), d(t)) + bu(t) \quad (3.10)$$

where  $y$  is the system output,  $n$  is the order of the dynamic system,  $u$  is the control signal,  $d$  is the external disturbance, and  $b$  is the control signal gain.  $F$ , considered as the generalized disturbance, is a multivariable function of the internal dynamics and the external disturbance. The block diagram of the linear ADRC is shown in Figure 3.2.

Assuming that  $F$  is differentiable with  $h = \dot{F}$ , (3.10) can be written in the state space form as:

$$\begin{cases} \dot{x} = Ax + Bu + Eh \\ y = Cx \end{cases} \quad (3.11)$$

with

$$A = \begin{bmatrix} 0 & 1 & 0 & \cdots & 0 \\ 0 & 0 & 1 & \cdots & 0 \\ \vdots & \vdots & \vdots & \ddots & \vdots \\ 0 & 0 & 0 & \cdots & 1 \\ 0 & 0 & 0 & \cdots & 0 \end{bmatrix}_{(n+1) \times (n+1)}$$

$$B = [0 \ 0 \ \cdots \ b \ 0]^T_{(n+1) \times 1}$$

$$E = [0 \ 0 \ \cdots \ 0 \ 1]^T_{(n+1) \times 1}$$

$$C = [1 \ 0 \ \cdots \ 0 \ 0]_{1 \times (n+1)}$$

where  $x_1 = y$ ,  $x_2 = \dot{y}$ , ...,  $x_n = y^{(n-1)}$ ,  $x_{n+1} = F$ , and the system state vector

$x = [x_1 \ x_2 \ \cdots \ x_n \ x_{n+1}]^T$ .  $x_{n+1} = F$  is the augmented state.

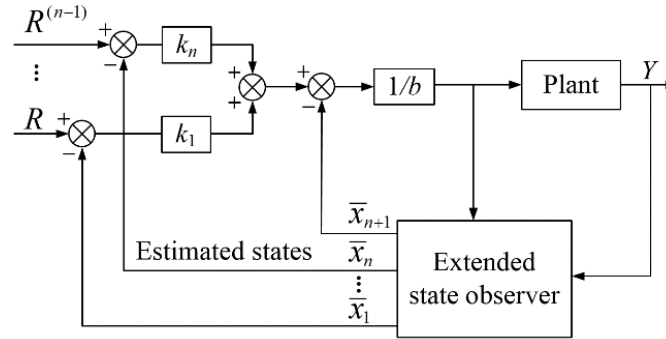


Figure 3.2 Block diagram of linear ADRC

The ESO for (3.11) is designed as:

$$\begin{cases} \dot{\bar{x}} = A\bar{x} + Bu + L(y - \bar{y}) \\ \bar{y} = C\bar{x} \end{cases} \quad (3.12)$$

where the observer state vector is  $\bar{x} = [\bar{x}_1 \ \bar{x}_2 \ \cdots \ \bar{x}_n \ \bar{x}_{n+1}]^T$  and the observer gain vector

is  $L = [l_1 \ l_2 \ \cdots \ l_n \ l_{n+1}]^T$ . The tuning of the observer gains is to make the observer states

in (3.12) track the system states in (3.11).

The control law is designed to compensate the effect of the generalized disturbance  $F$  tracked by  $\bar{x}_{n+1}$  on the dynamic system:

$$u = \frac{k_1(R - \bar{x}_1) + k_2(\dot{R} - \bar{x}_2) + \dots + k_n(R^{(n-1)} - \bar{x}_n) - \bar{x}_{n+1}}{b} \quad (3.13)$$

where  $k_1, k_2, \dots, k_n$  are the controller gains and  $R$  is the reference input.

Substituting (3.13) into (3.10), the controlled dynamic system becomes:

$$y^{(n)} = F - \bar{x}_{n+1} + k_1(R - \bar{x}_1) + k_2(\dot{R} - \bar{x}_2) + \dots + k_n(R^{(n-1)} - \bar{x}_n) \quad (3.14)$$

The value of  $(F - \bar{x}_{n+1})$  is negligible if the ESO is tuned properly. Therefore, the right side of (3.14) becomes a PD controller.

It can be seen from the ESO (3.12) and the control law (3.13) that, the number of tuning gains in the ADRC is  $2n+1$ , which is the sum of  $n+1$  observer gains and  $n$  controller gains. This shows that the number of tuning gains increases proportionally as the order of the controlled system increases. To reduce the number of tuning parameters, the bandwidth tuning method was proposed to parameterize the observer and controller gains [32]. In this method, the observer gains are chosen such that the roots of the characteristic polynomial of  $(A - LC)$  are at  $-w_o$ , i.e.,

$$\lambda_o(s) = s^{n+1} + l_1 s^n + \dots + l_n s + l_{n+1} = (s + w_o)^{n+1}$$

This makes  $\lambda_o(s)$  become Hurwitz, and  $w_o$ , known as the observer bandwidth, becomes the only tuning parameter for the ESO [28]. Similarly, the controller gains are

chosen such that the poles of the approximate closed-loop characteristic polynomial  $\lambda_c(s)$  of (3.14) are at  $-w_c$ , i.e.,

$$\lambda_c(s) = s^n + k_n s^{n-1} + \dots + k_2 s + k_1 = (s + w_c)^n$$

This makes  $\lambda_c(s)$  become Hurwitz, and  $w_c$ , known as the controller bandwidth, becomes the only tuning parameter for the control law [28]. Assuming  $h$  is bounded, there exist positive  $w_o$  and  $w_c$  such that the ADRC system is stable [27, 28]. Generally, increasing the observer bandwidth reduces the estimation errors of the ESO but increases the noise sensitivity. An appropriate observer bandwidth should be tuned in a trade-off between the tracking performance and the noise tolerance [56]. Furthermore, as the controller bandwidth increases, the speed of the transient response increases but the stability margin decreases. A proper controller bandwidth should be tuned in a compromise between the transient response and the robustness [56]. The bandwidth tuning method reduces the number of tuning parameters and works well for first- and second-order controlled systems. However, because the gains of the ESO and the control law are functions of the two bandwidths, the bandwidth tuning method could deteriorate the tracking performance in tuning the ADRC for high-order systems.

In summary, combining the ESO and the control law, the linear ADRC is given as:

$$\left\{ \begin{array}{l} \text{ESO:} \\ \dot{\bar{x}} = A\bar{x} + Bu + L(y - \bar{y}) \\ \bar{y} = C\bar{x} \\ \text{Control law :} \\ u = \frac{k_1(R - \bar{x}_1) + k_2(\dot{R} - \bar{x}_2) + \dots + k_n(R^{(n-1)} - \bar{x}_n) - \bar{x}_{n+1}}{b} \end{array} \right.$$

In this thesis, the linear ADRC is applied to the automated steering control for vehicle lane keeping and position control of hydraulic actuators. The details of the controller design can refer to Chapters 4 and 5.

### 3.3 Concept of Lyapunov Exponents

Lyapunov's second method is the general way to study the stability of a dynamic system. However, constructing the Lyapunov functions becomes very challenging when system dynamics are complicated. Therefore, the concept of Lyapunov exponents, as an alternative and powerful tool for the stability analysis of complicated and nonlinear dynamic systems, is used to investigate the stability of the ADRC system.

We monitor the long-term evolution of an infinitesimal  $n$ -sphere of an initial condition. As time goes on, the sphere will turn into a  $n$ -ellipsoid owing to the local deforming nature of the flow [69]. The  $i$ th Lyapunov exponent is defined as follows:

$$\lambda_i = \lim_{t \rightarrow \infty} \frac{1}{t} \ln \frac{P_i(t)}{P_i(t_0)}, \quad i = 1, 2, \dots, n \quad (3.15)$$

where  $P_i(t)$  and  $P_i(t_0)$  represent the lengths of the  $i$ th principal axis of the ellipsoid at times  $t$  and  $t_0$ , respectively.

According to the above definition, the  $i$ th Lyapunov exponent  $\lambda_i$  represents the average rate of change of the principal axis  $P_i(t)$  over a long-term period. In practical applications, finite-time exponents instead of infinite-time exponents are calculated for the sake of time, which are defined as follows:

$$\lambda_i = \frac{1}{t} \ln \frac{P_i(t)}{P_i(t_0)}, \quad i = 1, 2, \dots, n \quad (3.16)$$

The long-term evolution of a two-dimensional sphere with two principal axes helps to understand the transformation process, as shown in Figure 3.3.

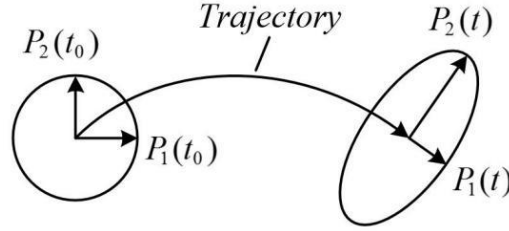


Figure 3.3 Evolution of two-dimensional dynamic system

Compared to the classical stability analysis, which linearizes the dynamic system in a small region around the equilibrium point, the concept of Lyapunov exponents performs the linearization around the points on the trajectory. The Lyapunov exponents are global properties of dynamic systems and are independent of the initial conditions from the same stability region [70]. The number of Lyapunov exponents is equivalent to the dimension of the dynamic system. The stability property of the dynamic system could be described by the signs of the Lyapunov exponents [69]: for a continuous autonomous dynamic system, 1) if all the Lyapunov exponents are negative, the dynamic system is exponentially stable around the equilibrium point; 2) if one of the Lyapunov exponents is zero but the others are negative, the system has a limit cycle attractor; 3) for third- or higher-order systems, positive Lyapunov exponents indicate a chaotic behavior.

### 3.4 Calculation of Lyapunov Exponents Based on Model

According to the definition, the Lyapunov exponents are determined numerically because it is infeasible to determine them analytically [71]. Generally, the Lyapunov exponents can be calculated based on a mathematical model of the dynamic system or from a time series measured experimentally. In this thesis, the Lyapunov exponents of the ADRC system are calculated based on a mathematical model using the algorithm developed in [69]. To calculate the Lyapunov exponents, consider a continuous autonomous dynamic system in an  $n$ -dimensional state space:

$$\dot{x} = f(x(t)) \quad (3.17)$$

where the state vector  $x = [x_1, x_2, \dots, x_n]^T \in \mathbb{R}^n$ , and  $f(x(t))$  is a continuously differentiable vector function.

A fiducial trajectory of the sphere center is defined by the nonlinear motion equations (3.17) on an initial condition. The evolutions of the principal axes are described by the linearized motion equations of an initially orthonormal vector frame anchored to the fiducial trajectory [72] as follows:

$$\dot{\psi} = J(x(t))\psi \quad (3.18)$$

where  $\psi$  is defined as the state transition matrix of the linearized system  $\delta x(t) = \psi \delta x(0)$ .

$J(x(t))$  is the Jacobian matrix:

$$J(x(t)) = \left. \frac{\partial f(x)}{\partial x^T} \right|_{x=x(t)} \quad (3.19)$$

Equations (3.17) and (3.18) are combined as follows:

$$\begin{cases} \dot{x} = f(x(t)) \\ \dot{\psi} = J(x(t))\psi \end{cases} \quad (3.20)$$

with the initial condition:

$$\begin{cases} x(0) = x_0 \\ \psi(0) = I \end{cases}$$

where  $I$  is the identity matrix.

During each integration step, the Gram-Schmidt Reorthonormalization (GSR) method is used to orthonormalize  $\delta x_1, \delta x_2, \dots, \delta x_n$  to avoid misalignment along the direction of the maximal expansion [72]. The GSR generates an orthonormal set  $\{u_1, u_2, \dots, u_n\}$ , which spans the same subspace of  $\{\delta x_1, \delta x_2, \dots, \delta x_n\}$ :

$$\begin{cases} u_1 = \frac{\delta x_1}{\|\delta x_1\|} \\ u_2 = \frac{\delta x_2 - \langle \delta x_2, u_1 \rangle u_1}{\|\delta x_2 - \langle \delta x_2, u_1 \rangle u_1\|} \\ \vdots \\ u_n = \frac{\delta x_n - \langle \delta x_n, u_{n-1} \rangle u_{n-1} - \dots - \langle \delta x_n, u_1 \rangle u_1}{\|\delta x_n - \langle \delta x_n, u_{n-1} \rangle u_{n-1} - \dots - \langle \delta x_n, u_1 \rangle u_1\|} \end{cases}$$

where  $\langle \delta x_2, u_1 \rangle$  denotes the inner product of  $\delta x_2$  and  $u_1$ , and so on.

The orthonormalization for  $\delta x_1^j$  and  $\delta x_2^j$  of the two-dimensional sphere at the  $j$ th ( $j=1, 2, \dots, p$ , and  $p$  is the total integration times) integration step is shown in Figure 3.4. The  $\delta x_1^j$  and  $\delta x_2^j$  are first orthogonalized to  $v_1^j$  and  $v_2^j$ , and then normalized to  $u_1^j$  and  $u_2^j$ .



If the integration times  $p$  is large enough, at the final  $p$ th integration step, the Lyapunov exponents can be estimated by:

$$\lambda_i \approx \frac{1}{pq} \sum_{j=1}^p \ln \|u_i^{(j)}\| \quad (3.21)$$

where  $q$  is the time-step.

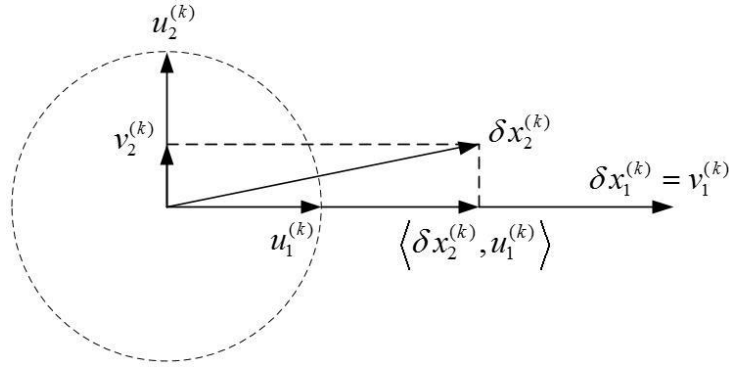


Figure 3.4 Orthonormalization for  $\delta x_1^j$  and  $\delta x_2^j$  of the two-dimensional sphere at the  $j$ th integration step

### 3.5 Quantitative Feedback Theory (QFT)

The design procedure of the conventional QFT includes four basic steps: generating plant templates, calculating bounds, loop shaping, and prefilter design [35]. In the following, these steps are presented in detail. Consider an uncertain plant  $P(s)$  in the two degree-of-freedom feedback system shown in Figure 3.5,

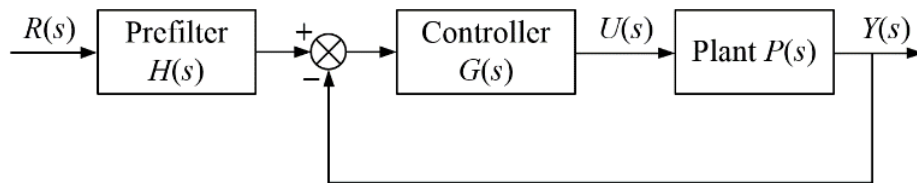


Figure 3.5 Two degree-of-freedom feedback system

described by a parametric family  $\{P\}$ ; for example:

$$\{P\} = \left\{ P(s) = \frac{k}{(s+a)(s+b)} : k \in [1, 10], a \in [1, 5], b \in [20, 30] \right\} \quad (3.22)$$

### 1) *Generating Templates:*

The first step in QFT design is to generate the plant templates at the selected frequencies in the Nichols chart. Each template represents the collection of the frequency responses of  $\{P\}$  at a selected frequency. Therefore, the plant dynamics is defined by these templates in the frequency domain [36]. The selected frequencies are generally the frequencies where the shapes of the templates vary significantly compared to those at other frequencies [35]. To calculate the bounds and perform the loop shaping in the next steps, it is required to designate a nominal plant element from  $\{P\}$ , i.e.,  $P_n(s)$ . Considering the open-loop transfer function  $L(s)=G(s) \cdot P(s)$ , the nominal open-loop transfer function is defined as  $L_n(s)=G(s) \cdot P_n(s)$ .

### 2) *Performance specifications*

The controller  $G(s)$  and the prefilter  $H(s)$  are designed to meet the performance specifications in the frequency domain shown as follows:

- a) Closed-loop stability specification: To guarantee the stability of the closed-loop control system, the following inequality must be satisfied for all  $P(s) \in \{P\}$ :

$$\left| \frac{G(j\omega)P(j\omega)}{1+G(j\omega)P(j\omega)} \right| \leq \delta_s \quad \forall \omega \in [0, \infty) \quad (3.23)$$

which ensures that the gain margin equals to  $20\log[(\delta_s + 1)/\delta_s]$  and the phase margin equals to  $2\sin^{-1}(1/2\delta_s)$  [36].

b) Reference tracking specification: If the control system involves tracking reference signal, the transfer function of the closed-loop control system:

$$T(s) = H(s) \frac{G(s)P(s)}{1 + G(s)P(s)} \quad (3.24)$$

should satisfy the following inequality to meet the tracking requirement:

$$|T_L(jw)| \leq |T(jw)| \leq |T_U(jw)| \quad \forall w \in [0, \infty) \quad (3.25)$$

where  $|T_L(jw)|$  and  $|T_U(jw)|$  are the lower and upper bounds of  $|T(jw)|$ . These are determined by the designer according to the desired transient response of the system [38]. In this thesis, the settling time and the percentage overshoot are used to describe the transient response.

### 3) *Generating bounds and loop-shaping*

The performance specifications are converted to constraints on the nominal open-loop transfer function. These constraints are presented as certain QFT bounds in the Nichols chart. Because the closed-loop stability specification represents the exteriors of circles in the complex plane, the corresponding QFT bounds are closed curves in the Nichols chart. For the reference tracking specification, the QFT bounds are open curves in the Nichols chart. After converting all the bounds from the performance specifications, these bounds should be combined into the grouped bounds.

The next step involves the loop shaping of the nominal open-loop transfer function. The nominal open-loop transfer function should be shaped to lie outside of the closed QFT bounds, and should be located above the open QFT bounds at the selected frequencies [36]. Because the nominal open-loop transfer function  $L_n(s)$  is the product of the nominal plant  $P_n(s)$  and the controller  $G(s)$ , after the loop shaping, the resulting  $G(s) = L_n(s)/P_n(s)$  can be obtained, where  $L_n(s)$  is the acceptable nominal open-loop transfer function. As an example, Figure 3.6 shows the QFT bounds, the initial nominal open-loop transfer function, and the acceptable nominal open-loop transfer function. The initial nominal open-loop transfer function only contains the nominal plant, whereas the acceptable nominal open-loop transfer function contains the nominal plant and the controller. It can be seen that the acceptable nominal open-loop transfer function is located above the open QFT bounds and lies outside of the closed QFT bounds at the selected frequencies.

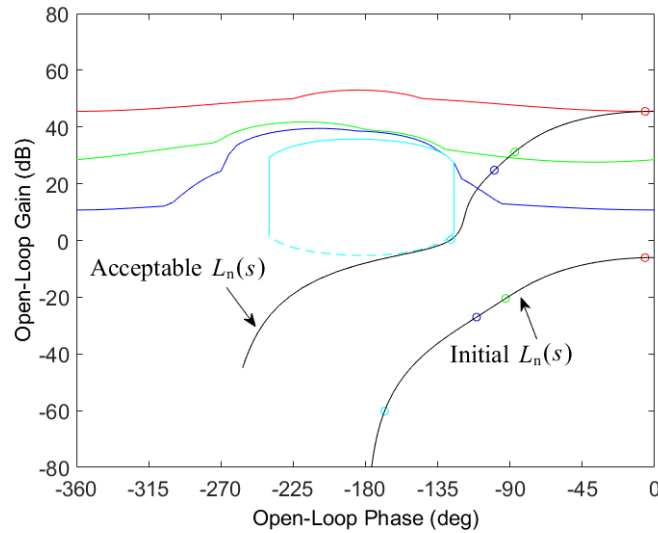


Figure 3.6 QFT bounds, the initial and acceptable nominal open-loop transfer functions in the Nichols chart

4) *Prefilter design*

In addition to the controller  $G(s)$ , the prefilter  $H(s)$  should be embedded within the closed-loop control system such that the reference tracking specification is satisfied.

From inequality (3.25), we have:

$$|T_L(j\omega)| \leq \left| \frac{H(j\omega)G(j\omega)P(j\omega)}{1+G(j\omega)P(j\omega)} \right| \Rightarrow \log |T_L(j\omega)| \leq \log |H(j\omega)| + \min \log \left| \frac{G(j\omega)P(j\omega)}{1+G(j\omega)P(j\omega)} \right| \quad (3.26)$$

$$\left| \frac{H(j\omega)G(j\omega)P(j\omega)}{1+G(j\omega)P(j\omega)} \right| \leq |T_U(j\omega)| \Rightarrow \log |H(j\omega)| + \max \log \left| \frac{G(j\omega)P(j\omega)}{1+G(j\omega)P(j\omega)} \right| \leq \log |T_U(j\omega)| \quad (3.27)$$

Inequalities (3.26) and (3.27) can be combined as follows:

$$\max \log \left| \frac{G(j\omega)P(j\omega)}{1+G(j\omega)P(j\omega)} \right| - \min \log \left| \frac{G(j\omega)P(j\omega)}{1+G(j\omega)P(j\omega)} \right| \leq \log \frac{|T_U(j\omega)|}{|T_L(j\omega)|} \quad (3.28)$$

It is noted that the left side of inequality (3.28) depends on the controller  $G(s)$  and the plant  $P(s)$ . Therefore, the job of the controller  $G(s)$  is to reduce the uncertainty of the closed-loop control system, whereas the prefilter  $H(s)$  does not contribute to this end. In fact, the job of the prefilter  $H(s)$  is to shift the frequency responses of the closed-loop control system within the lower and upper tracking bounds, as shown in Figure 3.7.

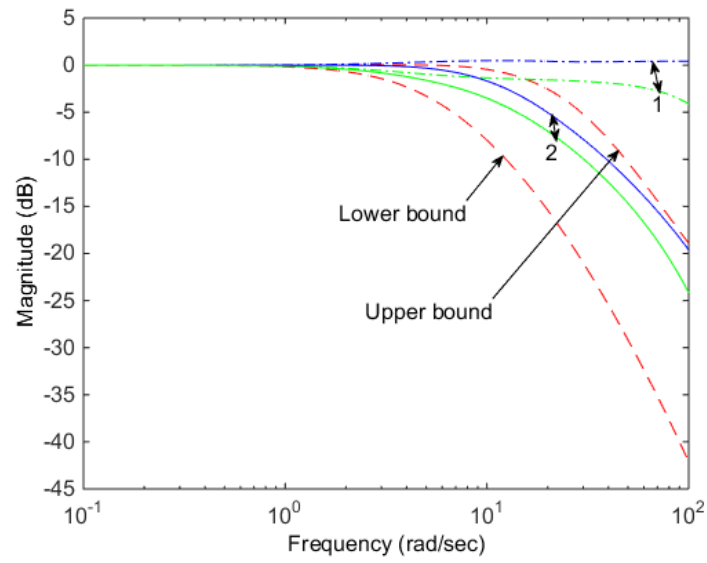


Figure 3.7 Effect of the prefilter  $H(s)$  on the frequency responses of the closed-loop transfer function (1:  $|GP(j\omega)/(1+GP(j\omega))|$ ), 2:  $|HGP(j\omega)/(1+GP(j\omega))|$ )

## Chapter 4

# Automated Steering Control for Vehicle Lane Keeping

In this chapter, the ADRC is applied to automated steering control for lane keeping in autonomous vehicles. First of all, a nonlinear four-wheel vehicle model for stability analysis and simulations, and a linearized two-wheel vehicle model for controller design are developed. Second, an ADRC steering controller is designed and the stability of the control system is investigated based on the concept of Lyapunov exponents. Third, simulations and experimental validation of the ADRC controller are conducted.

### **4.1 Vehicle Model**

#### **4.1.1 Nonlinear Vehicle model**

The dynamics of a passenger vehicle are complicated and could be described by a six or higher degree-of-freedom mathematical model [11]. Because the lateral control is the main concern in the steering controller design, a nonlinear vehicle model that maintains

the longitudinal, lateral, and yaw dynamics, while neglecting the pitch, roll, and heave dynamics, is considered, as shown in Figure 4.1 [79]. The model is presented as follows:

$$\begin{cases} m(\dot{v}_x - v_y r) = f_{xf} \cos \delta + f_{xr} - f_{yf} \sin \delta \\ m(\dot{v}_y + v_x r) = f_{xf} \sin \delta + f_{yr} + f_{yf} \cos \delta + f_w \\ I_z \dot{r} = l_f (f_{xf} \sin \delta + f_{yf} \cos \delta) - l_r f_{yr} + \frac{S_b}{2} (\Delta f_x - \Delta f_{yf} \sin \delta) + l_w f_w \end{cases} \quad (4.1)$$

where

$$\begin{cases} f_{xf} = f_{x1} + f_{x2}; & f_{xr} = f_{x3} + f_{x4} \\ f_{yf} = f_{y1} + f_{y2}; & f_{yr} = f_{y3} + f_{y4} \\ \Delta f_x = (f_{x4} - f_{x3}) + (f_{x2} - f_{x1}) \cos \delta; & \Delta f_{yf} = f_{y2} - f_{y1} \end{cases}$$

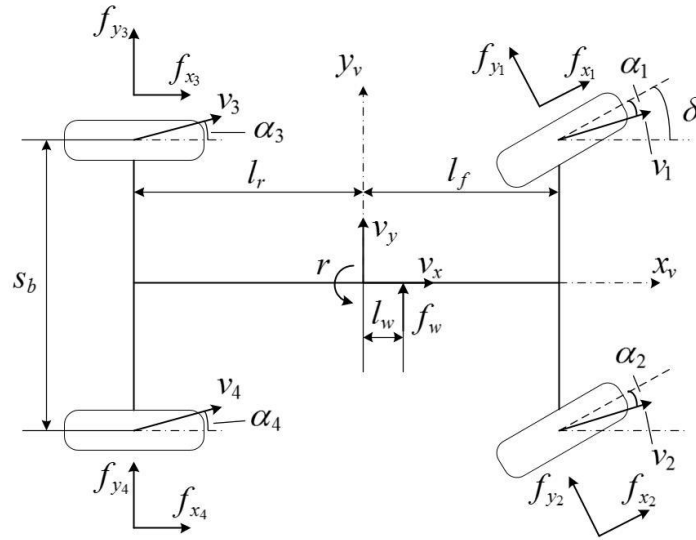


Figure 4.1 Four-wheel nonlinear vehicle model

The parameters in the model (4.1) are given in Table 4.1. Note that the model (4.1) can be applied to larger or smaller vehicles, because it is independent of the parameter values. The sideslip angle of the tire is defined as the angle between the absolute velocity and the  $x$ -direction of the wheel in the local coordinate system. Assuming that the



longitudinal velocity of the vehicle is constant, the longitudinal dynamics can be decoupled from the model.

Table 4.1 Vehicle parameters and nominal values used in stability analysis and simulations

Symbol	Parameter	Nominal value
$m$	Mass	991kg
$I_z$	Vertical inertial moment	1574kg·m <sup>2</sup>
$L$	Distance from the look-ahead point to the center of gravity (CG)	12m
$\rho$	Road curvature	Straight lane: 0m <sup>-1</sup> Curved lane: 0.003m <sup>-1</sup>
$f_w$	Wind force	300N
$l_w$	Position of the wind force	0.4m
$l_f$	Distance from the front axis to the CG	1m
$l_r$	Distance from the rear axis to the CG	1.45m
$s_b$	Wheel-base width	1.4m
$b_i$	Magic Formula parameter	$b_1 = b_2 = 8.3278, b_3 = b_4 = 11.6590$
$c_i$	Magic Formula parameter	$c_1 = c_2 = c_3 = c_4 = 1.1009$
$d_i$	Magic Formula parameter	$d_1 = d_2 = 2268.0, d_3 = d_4 = 1835.8$
$e_i$	Magic Formula parameter	$e_1 = e_2 = -1.661, e_3 = e_4 = -1.542$
$c_f$	Cornering stiffness of the front wheel	$c_f = 2b_1c_1d_1$
$c_r$	Cornering stiffness of the rear wheel	$c_r = 2b_3c_3d_3$
$n_t$	Tire-road length contact	1.3cm
$v_x$	Longitudinal velocity	25m/s
$v_y$	Lateral velocity	-
$r$	Yaw rate	-
$f_{x_i}$	Longitudinal force of the $i$ th tire	-
$f_{y_i}$	Lateral force of the $i$ th tire	-
$\alpha_i$	Sideslip angle of the $i$ th tire	-
$v_i$	Absolute velocity of the $i$ th wheel	-
$\delta$	Steering angle of the front wheels	-

The lateral tire forces can be estimated by different tire models. The linear tire model is a good approximation of the lateral tire forces when the sideslip angles are small (less than 2 degrees), where the lateral tire forces are proportional to the sideslip angles [80]. However, when the sideslip angles become large, a more sophisticated tire model is required. In the vehicle model (4.1), the Pacejka Magic Formula tire model [81], which provides accurate tire forces, is used to obtain the lateral tire forces:

$$f_{y_i}(\alpha_i) = d_i \sin\{c_i \tan[(1-e_i)b_i\alpha_i + e_i \tan(b_i\alpha_i)]\} \quad i = 1, 2, 3, 4 \quad (4.2)$$

where

$$\begin{aligned} \alpha_1 &= \delta - \tan^{-1} \left( \frac{v_y - (n_t \cos \delta) \dot{\delta} - (n_t \cos \delta - l_f) r}{v_x + (n_t \sin \delta) \dot{\delta} + (n_t \sin \delta - s_b/2) r} \right) \\ \alpha_2 &= \delta - \tan^{-1} \left( \frac{v_y - (n_t \cos \delta) \dot{\delta} - (n_t \cos \delta - l_f) r}{v_x + (n_t \sin \delta) \dot{\delta} + (n_t \sin \delta + s_b/2) r} \right) \\ \alpha_3 &= -\tan^{-1} \left( \frac{v_y - l_r r}{v_x - s_b r/2} \right); \quad \alpha_4 = -\tan^{-1} \left( \frac{v_y - l_r r}{v_x + s_b r/2} \right) \end{aligned}$$

To study the effect of road adhesion on lane keeping performance, a road adhesion coefficient  $\mu$  with  $\mu=1$  for the normal road and  $0 < \mu < 1$  for a slippery road is used to represent different road adhesions. This is incorporated into (4.2) by replacing  $b_i$  with  $(2-\mu)b_i$ ,  $c_i$  with  $(5/4-\mu/4)c_i$ , and  $d_i$  with  $\mu d_i$  [79].

To achieve automated steering for lane keeping, a look-ahead sensing system is used to estimate the lateral offset  $y_L$  between the vehicle and the road centerline at the look-ahead point, as shown in Figure 4.2. The dynamics of the look-ahead sensing system can be modeled as [11]:

$$\begin{cases} \dot{y}_L = v_x \varepsilon_L + v_y + rL \\ \dot{\varepsilon}_L = r - v_x \rho \end{cases} \quad (4.3)$$

where  $\varepsilon_L$  is the angle between the tangent to the road and the longitudinal axis of the vehicle at the look-ahead point.

Equations (4.1) to (4.3) are combined to describe the nonlinear vehicle steering system for the stability analysis and simulations. The system states are  $v_y$ ,  $r$ ,  $y_L$ , and  $\varepsilon_L$ .

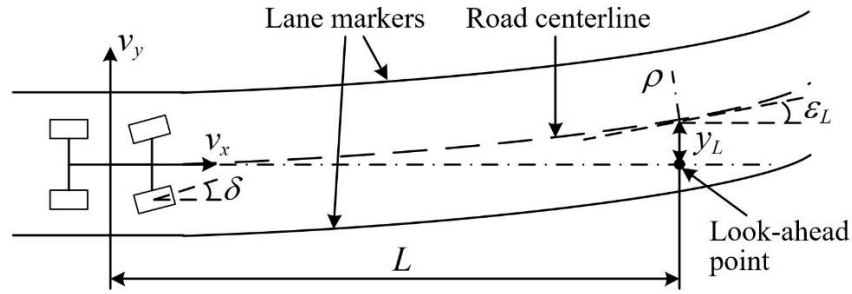


Figure 4.2 Look-ahead sensing estimation

### 4.1.2 Linear Vehicle Model

A linear vehicle model simplified from the nonlinear vehicle model is used for the purpose of designing the steering controller. The two front wheels and the two rear wheels in the linear model are respectively combined, as shown in Figure 4.3. The nonlinear terms in the nonlinear model can be linearized by assuming the steering angle and the sideslip angles are small [80]. The linear vehicle model is given as follows:

$$\begin{cases} m(\dot{v}_y + v_x r) = f_{yr} + f_{yf} + f_w \\ I_z \dot{r} = l_f f_{yf} - l_r f_{yr} + l_w f_w \end{cases} \quad (4.4)$$

with

$$\begin{cases} f_{y_f} = c_f \alpha_f = c_f \left( \delta - \frac{v_y + l_f r}{v_x} \right) \\ f_{y_r} = c_r \alpha_r = -c_r \frac{v_y - l_r r}{v_x} \end{cases}$$

where  $\alpha_f$  and  $\alpha_r$  are the sideslip angles of the front and rear tires, respectively. The lateral tire forces are proportional to the sideslip angles with coefficients  $c_f = 2b_1c_1d_1$  and  $c_r = 2b_3c_3d_3$ .

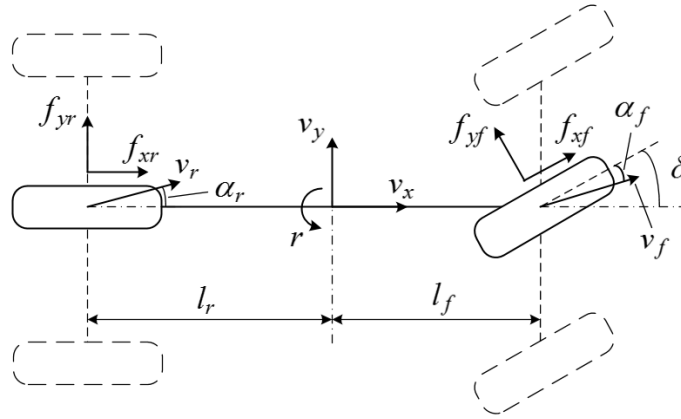


Figure 4.3 Two-wheel linear vehicle model

Combining the linear vehicle model with the look-ahead sensing dynamics, the linear vehicle steering model for the controller design is given as follows:

$$\begin{cases} \dot{Y} = AY + B_1\delta + B_2\rho + B_3f_w \\ y_L = CY \end{cases} \quad (4.5)$$

with

$$A = \begin{bmatrix} -\frac{c_f + c_r}{mv_x} & \frac{c_r l_r - c_f l_f}{mv_x} - v_x & 0 & 0 \\ \frac{c_r l_r - c_f l_f}{I_z v_x} & -\frac{c_r l_r^2 + c_f l_f^2}{I_z v_x} & 0 & 0 \\ 1 & L & 0 & v_x \\ 0 & 1 & 0 & 0 \end{bmatrix}; B_1 = \begin{bmatrix} \frac{c_f}{m} \\ \frac{c_f l_f}{I_z} \\ 0 \\ 0 \end{bmatrix}; B_2 = \begin{bmatrix} 0 \\ 0 \\ 0 \\ -v_x \end{bmatrix}; B_3 = \begin{bmatrix} \frac{1}{m} \\ \frac{l_w}{I_z} \\ 0 \\ 0 \end{bmatrix}; C = \begin{bmatrix} 0 \\ 0 \\ 1 \\ 0 \end{bmatrix}^T$$

where the states vector is  $Y = [v_y \ r \ y_L \ \varepsilon_L]^T$ .

The goal of the automated steering control for lane keeping is to keep the vehicle within the designated lane by regulating the lateral offset  $y_L$  to zero. In the steering control system shown in Figure 4.4,  $P_1(s)$  is the transfer function from the steering angle  $\delta$  to the lateral offset,  $P_2(s)$  is the transfer function from the road curvature  $\rho$  to the lateral offset, and  $P_3(s)$  is the transfer function from the wind force to the lateral offset. The reference input  $R(s)$  is set to zero. The steering angle is the control signal. The road curvature and the wind force are considered as the external disturbance [11, 18-20].

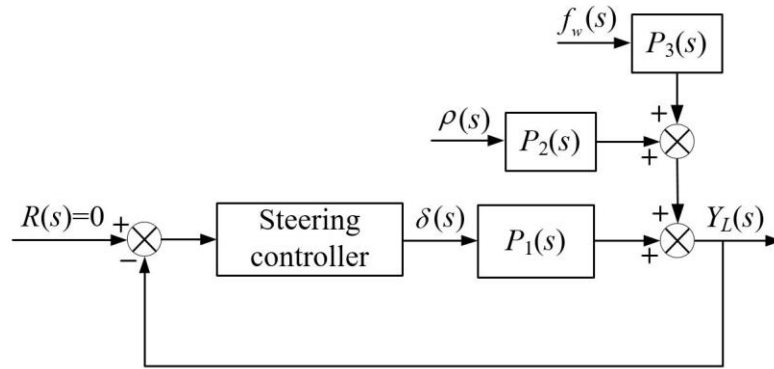


Figure 4.4 Steering control system for lane keeping

## 4.2 Controller Design

From the linear vehicle steering model (4.5), we have:

$$\ddot{y}_L = v_x \dot{\mathcal{E}}_L + \dot{v}_y + \dot{r}L = v_x(r - v_x \rho) + \dot{v}_y + \dot{r}L = v_x r - v_x^2 \rho + \dot{v}_y + \dot{r}L \quad (4.6)$$

and

$$\begin{cases} \dot{v}_y = a_1 v_y + a_2 r + b_{11} \delta + b_{31} f_w \\ \dot{r} = a_3 v_y + a_4 r + b_{12} \delta + b_{32} f_w \end{cases} \quad (4.7)$$

where

$$\begin{aligned} a_1 &= -\frac{c_f + c_r}{mv_x}, \quad a_2 = \frac{c_r l_r - c_f l_f}{mv_x} - v_x, \quad b_{11} = \frac{c_f}{m}, \quad b_{12} = \frac{c_f l_f}{I_z} \\ a_3 &= \frac{c_r l_r - c_f l_f}{I_z v_x}, \quad a_4 = -\frac{c_r l_r^2 + c_f l_f^2}{I_z v_x}, \quad b_{31} = \frac{1}{m}, \quad b_{32} = \frac{l_w}{I_z} \end{aligned}$$

Substituting (4.7) into (4.6), we have:

$$\begin{aligned} \ddot{y}_L &= v_x r - v_x^2 \rho + a_1 v_y + a_2 r + b_{11} \delta + b_{31} f_w + a_3 v_y L + a_4 r L + b_{12} \delta L + b_{32} f_w L \\ &= F + (b_{11} + b_{12} L) \delta \end{aligned} \quad (4.8)$$

where  $F$  represents the internal dynamics and external disturbances:

$$F = v_x r - v_x^2 \rho + a_1 v_y + a_2 r + b_{31} f_w + a_3 v_y L + a_4 r L + b_{32} f_w L$$

Let  $x_1 = y_L$ ,  $x_2 = \dot{x}_1$  and  $x_3 = F$ ; assuming that  $F$  is differentiable with  $\dot{h} = \dot{F}$ , (4.8)

can be expressed in the state space form as:

$$\begin{cases} \dot{x}_1 = x_2 \\ \dot{x}_2 = x_3 + (b_{11} + b_{12} L) \delta \\ \dot{x}_3 = h \end{cases} \quad (4.9)$$

The ESO for (4.9) can be designed as:

$$\begin{cases} \dot{\bar{x}}_1 = \bar{x}_2 + l_1(x_1 - \bar{x}_1) \\ \dot{\bar{x}}_2 = \bar{x}_3 + l_2(x_1 - \bar{x}_1) + (b_{11} + b_{12}L)\delta \\ \dot{\bar{x}}_3 = l_3(x_1 - \bar{x}_1) \end{cases} \quad (4.10)$$

where  $\bar{x}_1$ ,  $\bar{x}_2$ , and  $\bar{x}_3$  are the observer states.  $l_1$ ,  $l_2$ , and  $l_3$  are the observer gains. With properly tuned observer gains, the observer states  $\bar{x}_1$ ,  $\bar{x}_2$ , and  $\bar{x}_3$  track the system states  $x_1$ ,  $x_2$ , and  $x_3$ , respectively.

The control law is designed as:

$$\delta = \frac{k_1(R - \bar{x}_1) - k_2\bar{x}_2 - \bar{x}_3}{b_{11} + b_{12}L} \quad (4.11)$$

where  $k_1$  and  $k_2$  are the controller gains.

Substituting the control law (4.11) into (4.8), we have:

$$\ddot{y}_L = F - \bar{x}_3 + k_1(R - \bar{x}_1) - k_2\bar{x}_2 \quad (4.12)$$

With well-tuned observer gains, the value of  $(F - \bar{x}_3)$  is negligible.

In the ESO (4.10) and the control law (4.11), five gains are needed for tuning, i.e.,  $l_1$ ,  $l_2$ ,  $l_3$ ,  $k_1$ , and  $k_2$ . It is obvious that tuning these gains by trial and error is challenging. To reduce the tuning difficulty, the bandwidth tuning method is used to tune these gains. Because (4.8) is a second-order system, the observer gains are chosen such that the roots of the characteristic polynomial  $\lambda_o(s)$  of (4.10) are at  $-w_o$ , i.e.,  $\lambda_o(s) = s^3 + l_1s^2 + l_2s + l_3 = (s + w_o)^3$ . Therefore, the observer gains are selected as  $l_1 = 3w_o$ ,  $l_2 = 3w_o^2$ , and  $l_3 = w_o^3$ . Similarly, the controller gains are chosen such that the poles of the

approximate closed-loop characteristic polynomial  $\lambda_c(s)$  of (4.12) are at  $-w_c$ , i.e.,  $\lambda_c(s) = s^2 + k_2s + k_1 = (s + w_c)^2$ . Therefore, the controller gains are selected as  $k_1 = w_c^2$  and  $k_2 = 2w_c$ . The observer and controller gains can be obtained by tuning  $w_o$  and  $w_c$ . In the stability analysis of the ADRC system and the simulations presented in the following sections,  $w_o$  and  $w_c$  are tuned to 20 rad/s and 4 rad/s, respectively.

### 4.3 Stability Analysis

The stability of the nonlinear vehicle system controlled by the ADRC steering controller is investigated in this section. According to the concept of Lyapunov exponents [69], the number of Lyapunov exponents is equivalent to the dimension of the dynamic system. The control system has seven states, including four states in the vehicle model and three states in the ADRC controller. Therefore, the number of Lyapunov exponents is seven. The initial condition of the controller states is considered as zero. The initial condition of the vehicle states  $[v_y \ r \ y_L \ \varepsilon_L]^T$  is chosen as  $[0.1 \ 0.05 \ 0.15 \ 0.01]^T$ . The nominal values of the vehicle parameters given in Table 4.1 are used here. The equilibrium points of the control system for the  $0 \text{ m}^{-1}$  and  $0.003 \text{ m}^{-1}$  road curvatures are  $[0.039 \ 0 \ 0 \ -0.002]^T$  and  $[-0.255 \ 0.075 \ 0 \ -0.026]^T$ , respectively. Choosing the time-step of  $q=0.01\text{s}$  and the integration times of  $p=10000$ , two groups of Lyapunov exponents are calculated, which are listed from large to small in Table 4.2. Group one is for the  $0 \text{ m}^{-1}$  road curvature and Group two is for the  $0.003 \text{ m}^{-1}$  road curvature. It can be seen that all the Lyapunov exponents in both groups are negative; therefore, the control system is exponentially stable around the equilibrium points. The time histories of the Lyapunov exponents are



shown in Figure 4.5. It is shown that the exponents converge to the negative steady values, which indicates the principal axes contract monotonically. Figure 4.6 demonstrates the state trajectories for the lateral velocity, yaw rate, and lateral offset converging to the equilibrium points, respectively.

Table 4.2 Lyapunov exponents pertaining to the nonlinear vehicle system controlled by the ADRC steering controller

Lyapunov exponent	Group one $\rho=0 \text{ m}^{-1}$	Group two $\rho=0.003 \text{ m}^{-1}$
$\lambda_1$	-1.0463	-1.0494
$\lambda_2$	-1.0470	-1.0504
$\lambda_3$	-1.1862	-1.1902
$\lambda_4$	-6.6641	-6.6672
$\lambda_5$	-6.6720	-6.6958
$\lambda_6$	-7.0082	-6.9028
$\lambda_7$	-25.3034	-25.3175

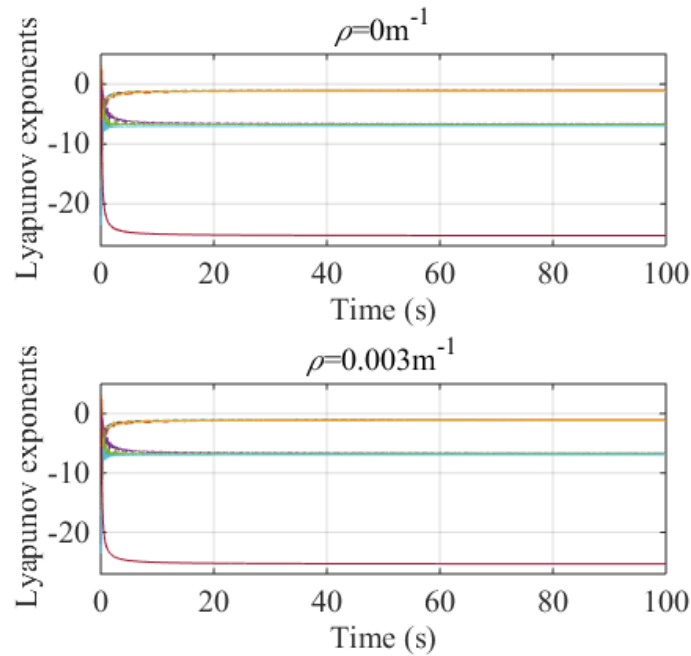


Figure 4.5 Time histories of Lyapunov exponents

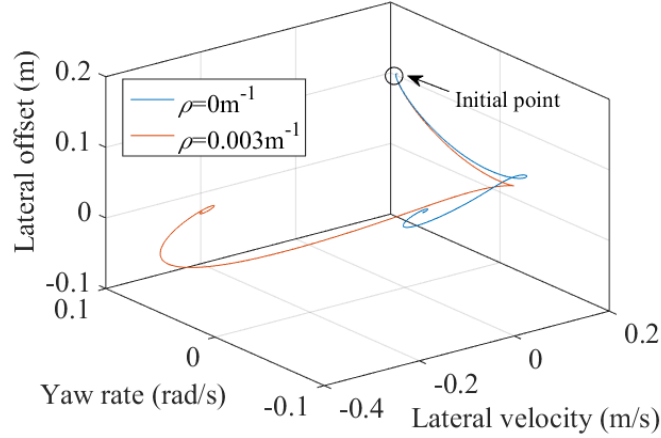


Figure 4.6 State trajectories converging to the equilibrium points

## 4.4 Simulations

The ADRC steering controller is tested on the nonlinear vehicle model. Six simulations are conducted assuming that the longitudinal velocity is unchanged during each simulation. The vehicle starts the automated steering for lane keeping at the initial condition  $[v_y \ r \ y_L \ \varepsilon_L]^T = [0.1 \ 0.05 \ 0.15 \ 0.01]^T$ . The wind force starts to act on the vehicle at the 6.5th second and ends at the 7.5th second. The road curvature changes from  $0 \text{ m}^{-1}$  at the 14th second. The nominal values of the vehicle parameters given in Table 4.1 are used in simulation S1. In each of the other five simulations, only one parameter value is changed relative to the first simulation, as shown in Table 4.3. The mass is assumed to be 991 kg when the vehicle is at full load. We consider an increase of the mass from 991 kg to 1100 kg owing to heavier passengers or extra luggage. The decrease in the look-ahead distance is based on the situation in which the vehicle is moving uphill or downhill. The tire road friction is reduced when the road surface is wet or icy. The increase in the road curvature is based on the condition that the vehicle is turning on a sharper corner. The

inertial moment  $I_z$  changes to  $1595 \text{ kg}\cdot\text{m}^2$  when the vehicle mass  $m$  increases from 991 kg to 1100 kg in simulation S2. Note that increasing the vehicle mass and the inertial moment, and decreasing the road adhesion coefficient (smaller tire forces) and the look-ahead distance degrade the lane keeping performance [20].

Table 4.3 Parameter variations in six simulations

Simulation	S1	S2	S3	S4	S5	S6
$m$ (kg)	991	1100	991	991	991	991
$L$ (m)	12	12	11	12	12	12
$\mu$	1	1	1	0.6	1	1
$v_x$ (m/s)	25	25	25	25	30	25
$\rho$ ( $\text{m}^{-1}$ )	0.003	0.003	0.003	0.003	0.003	0.004

The simulation results are shown in Figure 4.7. Overall, the vehicle controlled by the ADRC steering controller remains within the lane and the lateral offset is regulated within 0.1 m, as shown in Figure 4.7 (a). With respect to the handling of the initial condition, the vehicle with smaller tire-road friction experiences a slightly larger lateral offset compared to the other parameter variations, as shown in Figure 4.7 (b). The vehicle performs comparably in all simulations under the effect of the wind force, as shown in Figure 4.7 (c). During the cornering, it is obvious that the vehicle experiences a larger lateral offset in simulations S5 and S6, i.e., increasing the longitudinal velocity or the road curvature causes a larger lateral offset, as shown in Figure 4.7 (d). This indicates that the longitudinal velocity and the road curvature have greater effects on the lane keeping performance than the vehicle mass, look-ahead distance, and tire-road friction during the cornering.

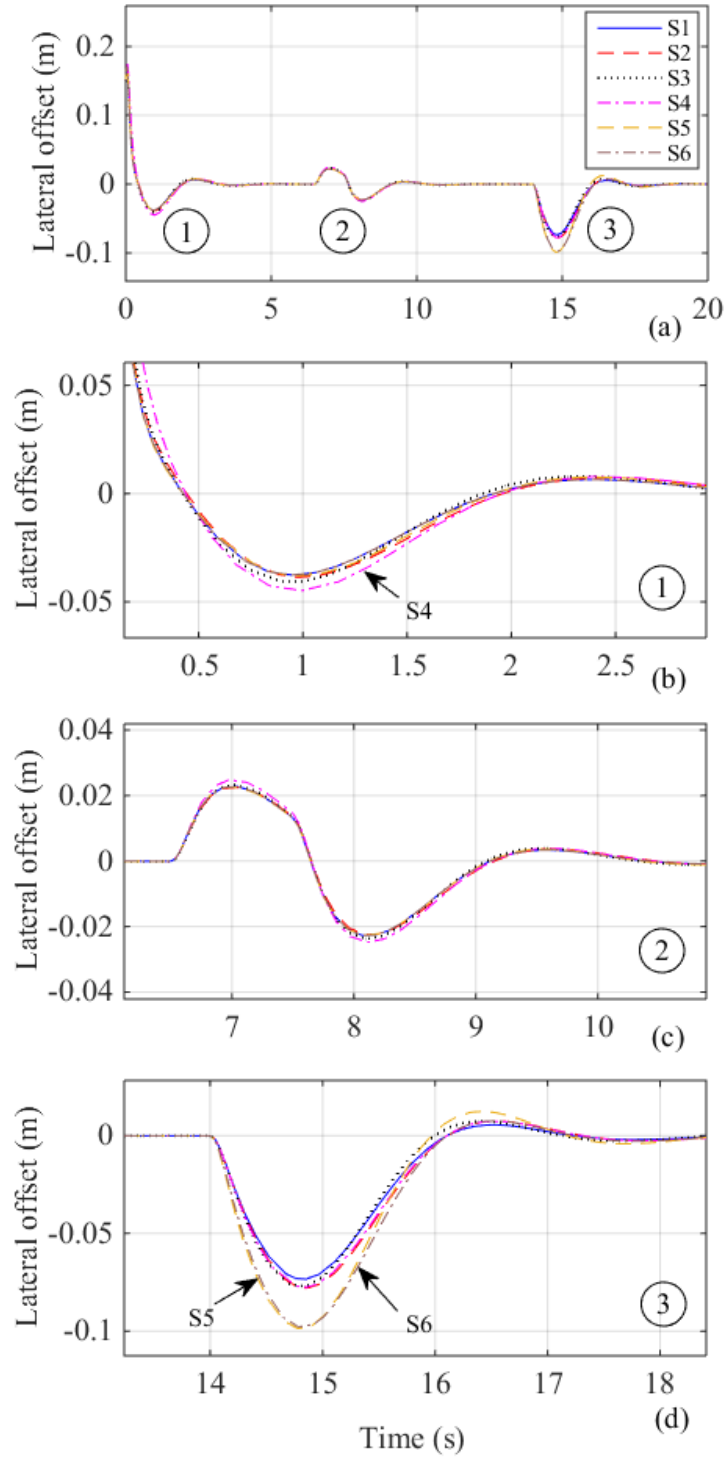


Figure 4.7 Simulations of the ADRC system with parameter variations and external disturbances: (a) overall view; (b) handling of the initial condition; (c) effect of the wind force; (d) effect of the road curvature during the cornering

## 4.5 Experimental Validation

In this section, the ADRC steering controller is implemented in a commercially available scaled vehicle. To realize the automated steering control, necessary electronic hardware and circuits are integrated into the scaled vehicle. The software for implementing the control algorithm and the computer vision program is developed. The vehicle is tested on both straight and curved lanes. The lane keeping performances of the ADRC and PID controllers are compared.

### 4.5.1 Experimental Setup

A scaled vehicle is set up to validate the ADRC controller. There are certain advantages of testing the ADRC controller on the scaled vehicle. For example, the construction of the scaled vehicle is less expensive and can be completed in a university lab in a relatively short period. During the testing, the manual control can be easily taken from the automated control, which makes the tests safer and repeatable.

The scaled vehicle is a commercial 1/5th Baja 5B scaled vehicle, as shown in Figure 4.8. The main parts of the scaled vehicle include: main chassis, drivetrain, front and rear suspensions, wheels and tires, steering mechanism, servo steering motor, direct current (DC) brushless driving motor, wireless transceiver, electronic speed controller (ESC), remote controller, two LiPo rechargeable batteries and other small components and electronics. The user can operate the steering of the front wheels and the driving of the rear wheels via the remote controller. The wireless transceiver receives commands from the remote controller and the ESC interprets the commands and controls the servo steering

motor and the DC brushless driving motor. The ESC is connected to the batteries and supplies power to the electronics and the motors.

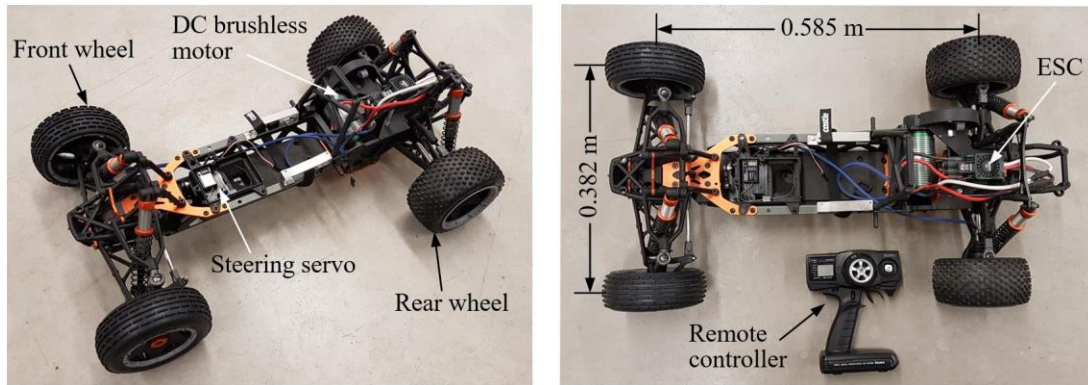


Figure 4.8 1/5th scaled vehicle

To implement the ADRC controller to the scaled vehicle and realize the automated steering control, certain design requirements are listed below to retrofit the scaled vehicle.

- 1) The lateral offset between the scaled vehicle and the road centerline at the look-ahead point must be measured. This needs a look-ahead sensing system to detect road information and a program to process the detected information.
- 2) The commands from the control algorithm should be delivered to the servo motor via a servo controller.
- 3) The longitudinal velocity of the vehicle needs to be controlled. This requires measurement of the velocity and a controller to control the DC brushless motor.
- 4) To monitor the vehicle behavior, measurements of the lateral acceleration and yaw rate are also needed.
- 5) The look-ahead sensing program and the control algorithm should be run in an onboard computer other than in an external computer to avoid signal transmission delay.


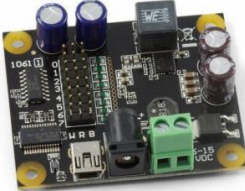


- 6) An external computer should be able to interface with the onboard computer via a local wireless network.
- 7) The software for implementing the look-ahead sensing program and the control algorithm should be portable, i.e., it should not be restricted to the scaled vehicle.

#### **4.5.1.1 Hardware**

To meet the aforementioned design requirements, some commercial electronic devices are used to retrofit the scaled vehicle. Table 4.4 lists the Phidgets electronic devices used for sensing and controlling in the scaled vehicle. The Phidgets devices communicate via USB and can be controlled by the application programming interface (API). The API provided by Phidgets supports a number of popular languages including C/C++, Python, Labview, and Java.

In order to allow the user to remotely control the execution of the software in the onboard computer and view the measured data in real-time, a wireless router is used to provide the local wireless network connection between the external computer and the onboard computer. The external computer can be any desktop, laptop, tablet or smartphone. To control the longitudinal velocity of the scaled vehicle, an encoder is mounted on the right-rear wheel to measure the rotation speed of the wheel. The measured data is collected by the Phidgets encoder board. A PID controller is tuned online to control the longitudinal velocity.

Table 4.4 Electronic devices used for sensing and controlling in the scaled vehicle

No.	Electronic device	Description
1		<p>Phidget SBC3:</p> <p>This device is a single board computer. It runs the software, collects signals from the devices No. 3 and 4, and outputs control signals to the device No. 2. The following devices are connected to this device via USB.</p>
2		<p>Phidget Advanced Servo 8-Motor:</p> <p>This device is used to control the steering servo motor and the DC brushless motor (via the ESC).</p>
3		<p>Phidget Encoder High Speed 4-Input:</p> <p>This device is used to read the encoder mounted on the right-rear wheel. The sampling speed is 125Hz.</p>
4		<p>Phidget Spatial 3/3/3 Basic:</p> <p>This device is used to measure the lateral acceleration and yaw rate of the scaled vehicle. The maximum sampling speed is 250Hz. The measurement resolutions of the lateral acceleration and yaw rate are <math>9.6\text{mm/s}^2</math> and <math>0.07^\circ/\text{s}</math>.</p>

For security reasons, a manual override switch that allows the user to take over the control of the vehicle from the software is implemented into the remote controller, as shown in Figure 4.9. The detailed control signal switch circuit is shown in Figure 4.10. The control signals generated by the onboard computer are sent to the servo controller, whereas the control signals generated by the user are sent to the radio transceiver.  $X$  represents the control signal for the DC brushless motor.  $Y$  represents the control signal



for the servo motor. Channel 3 of the transceiver is connected to an Arduino microcontroller. The Arduino microcontroller is used to control a multiplexer to switch the control signals between the servo controller and the radio transceiver.



Figure 4.9 Remote controller and automatic/manual switch

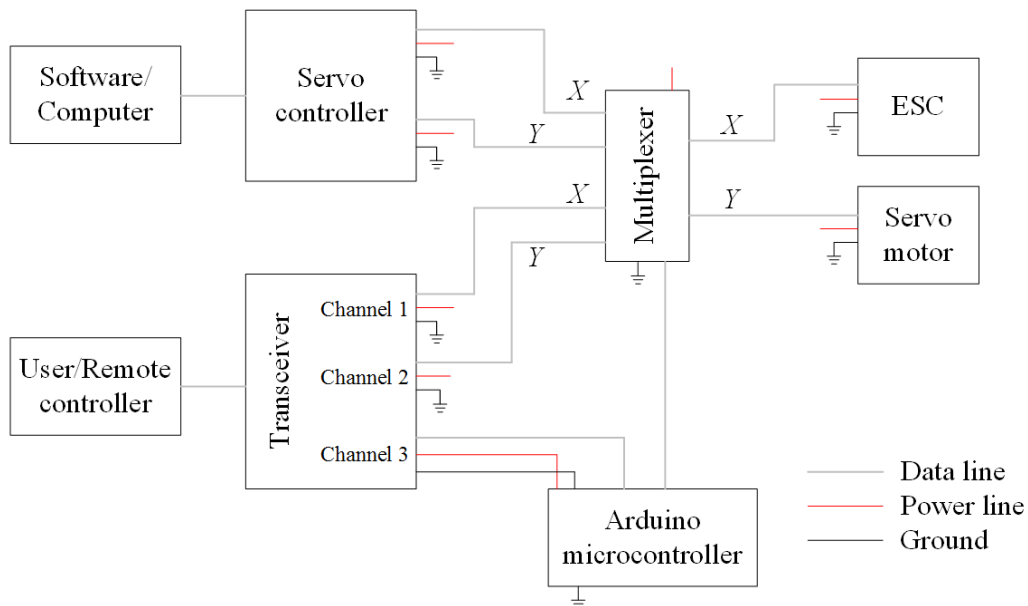


Figure 4.10 Circuit for switching control signals between the software and the user

The look-ahead sensing system is the most important component in the retrofitted scaled vehicle. To obtain the lateral offset at the look-ahead point, two different schemes for the look-ahead sensing system are developed:

- 1) Scheme A: Photoelectric sensors are installed in the front of the scaled vehicle to detect the road centerline. The lateral offset can be obtained by checking which sensor detects the road centerline.
- 2) Scheme B: A computer vision system is used to obtain the lateral offset. A camera is installed in front of the scaled vehicle to stream live video of the road. The vision program processes the video and estimates the lateral offset.

Flow charts of the automated steering control for lane keeping using the schemes A and B are shown in Figure 4.11.

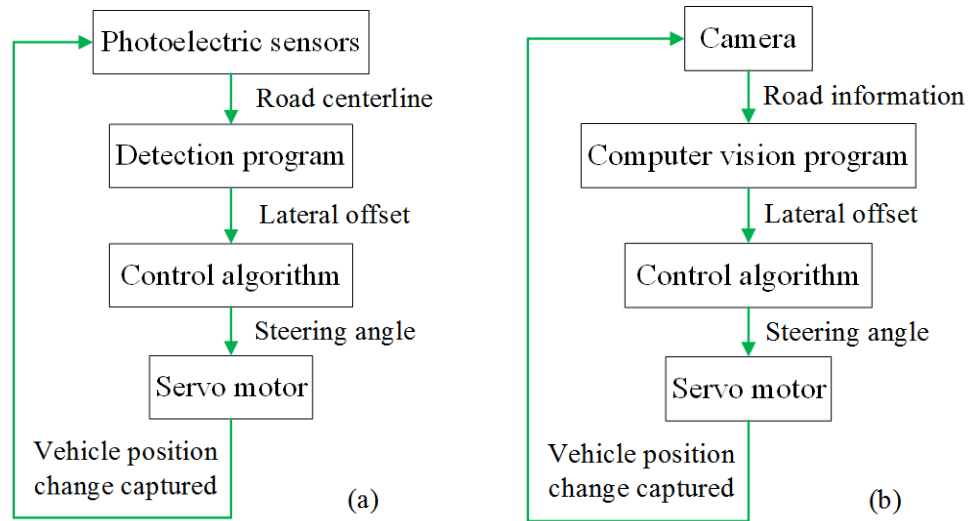

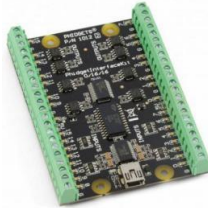



Figure 4.11 Flow charts of the automated steering control for lane keeping: (a) scheme A; (b) scheme B

In addition to the Phidgets devices mentioned above, some additional electronics are needed to realize the look-ahead sensing system. Table 4.5 shows the required electronics

for schemes A and B. In scheme A, the line sensors are connected to the digital inputs of the Phidgets Interface Kit. The Phidgets Interface Kit is able to check the status (high-level or low-level) of the signal output of each photoelectric sensor in the line sensor.

Table 4.5 Additional electronics needed for the look-ahead sensing systems

Scheme	Electronic device	Description
A		<b>Line Sensor LSS05:</b> This device has 5 infrared transmitter and receiver pairs (photoelectric sensors). It is used to detect the road centerline. The sampling speed is 100 Hz. The typical sensing distance is 2 cm.
		<b>Phidget Interface Kit 0/16/16:</b> This device has 16 digital inputs and digital outputs. It is used to check the status of the signal output of each photoelectric sensor.
B		<b>Logitech Pro Webcam:</b> This device is used to stream live video to the computer vision program. The optical resolution is 3 MP and the frame rate is 30 fps.

In the original scaled vehicle, the ESC connected to the batteries provides power to the motors and the radio transceiver. However, the embedded Phidgets devices, sensors, and other electronic devices consume more power than the ESC can supply. Therefore, an additional power supply must be built to satisfy the power requirements of these electronic devices. Figure 4.12 shows the additional power supply circuit. The input to the circuit is a 14.8 V LiPo battery, which is the same battery as that used to power the ESC. Because the operating voltage of the electronic devices is 12 V, a voltage regulator

MC7812 is used to step the battery voltage down to 12 V. The power supply diagram for the retrofitted scaled vehicle is shown in Figure 4.13.

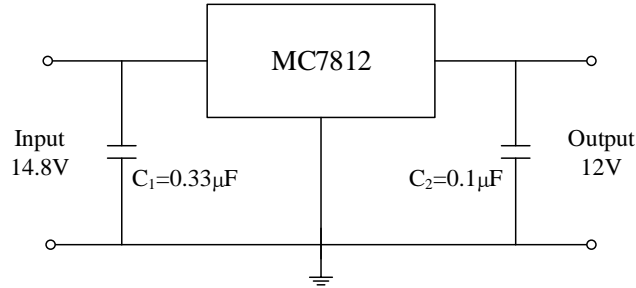


Figure 4.12 Voltage regulator circuit

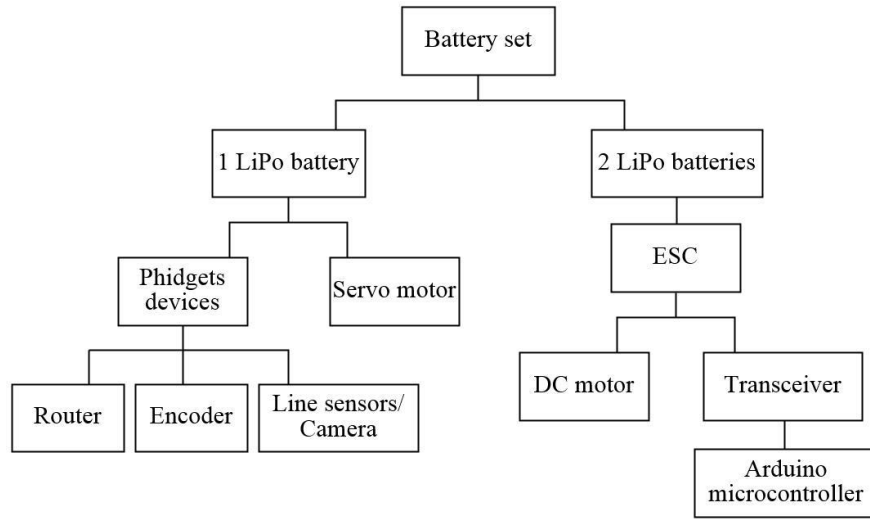


Figure 4.13 Power supply diagram for the retrofitted scaled vehicle

In the steering control system, the control signal is the steering angle of the front wheels of the vehicle. In the scaled vehicle, because the front wheels are steered by the servo motor via a steering mechanism, which is a spatial linkage, the actual control signal transmitted from the onboard computer to the servo controller is the rotation angle of the servo motor shaft. Therefore, it is necessary to determine the mathematical relationship between the steering angle of the front wheels and the rotation angle of the servo motor shaft. Figure 4.14 shows the steering mechanism of the scaled vehicle. Link 1 is driven

by the servo motor shaft. The motion is then transmitted from link 1 to the front wheels. A 3D model of the steering mechanism is built in Solidworks, which is a 3D modeling software package, widely used in both academia and industry. The 3D model is shown in Figure 4.15. Considering that the rotation angle of link 1 is  $\theta_1$  and the rotation angle of the wheel along the vertical axis is  $\theta_w$ , the relation between  $\theta_1$  and  $\theta_w$  can be obtained using the Motion Analysis function in Solidworks.

As the front wheels are turning left:

$$\theta_w = \frac{4}{5} \theta_1 \quad (4.13)$$

As the front wheels are turning right:

$$\theta_w = \frac{2}{3} \theta_1 \quad (4.14)$$

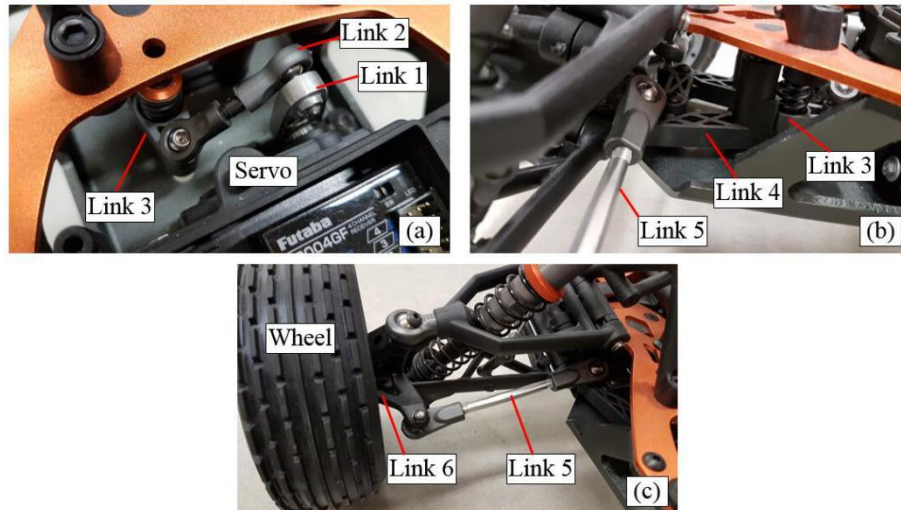


Figure 4.14 Steering mechanism of the scaled vehicle

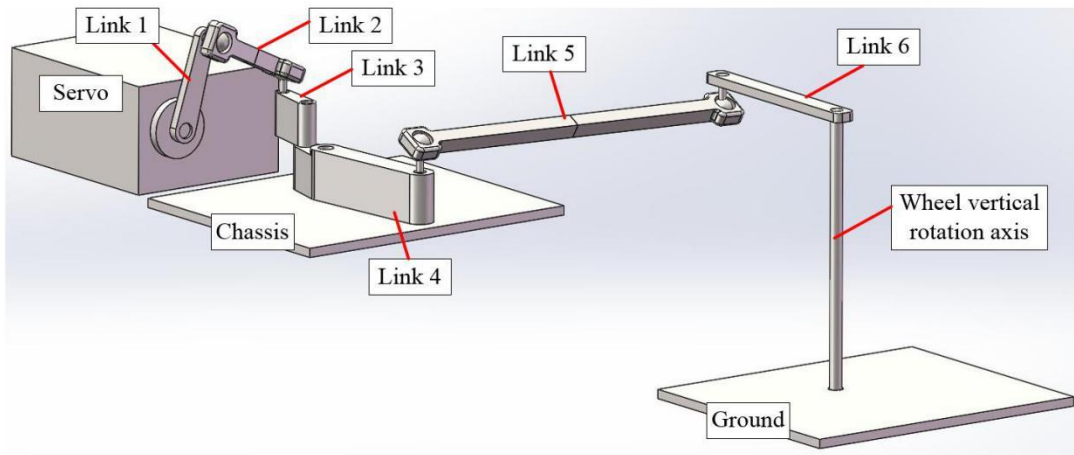


Figure 4.15 3D model of the steering mechanism in the scaled vehicle

### 4.5.1.2 Software

The system software is written in the Java programming language and runs with a sampling rate of 50 ms in the onboard computer. Because Java can run not only on Windows but also on Linux and Android, the software is not restricted to a particular platform. The software consists of two modules: the frontend and the backend. The frontend provides the interfacing between the external computer and the onboard computer. The backend implements the control scheme and the look-ahead sensing algorithm. It also communicates with the electronic hardware on the scaled vehicle and performs the data collection. Splitting up the software in this way makes the system test easier, because each module performs its own functionality, and modifications to one module do not require modifications to the other module. The frontend consists of a web server that runs on the onboard computer, and a user interface that runs on the external computer. Figure 4.16 shows the web browser-based user interface that runs on Google Chrome. The user interface allows the user start or stop the software execution, and also

displays the real-time measured data from the sensors. The commands from the user interface are first sent to the web server, and then transmitted to the backend. The high-level system software overview is shown in Figure 4.17. The backend software architecture is shown in Figure 4.18. Each block is implemented as a Java class.

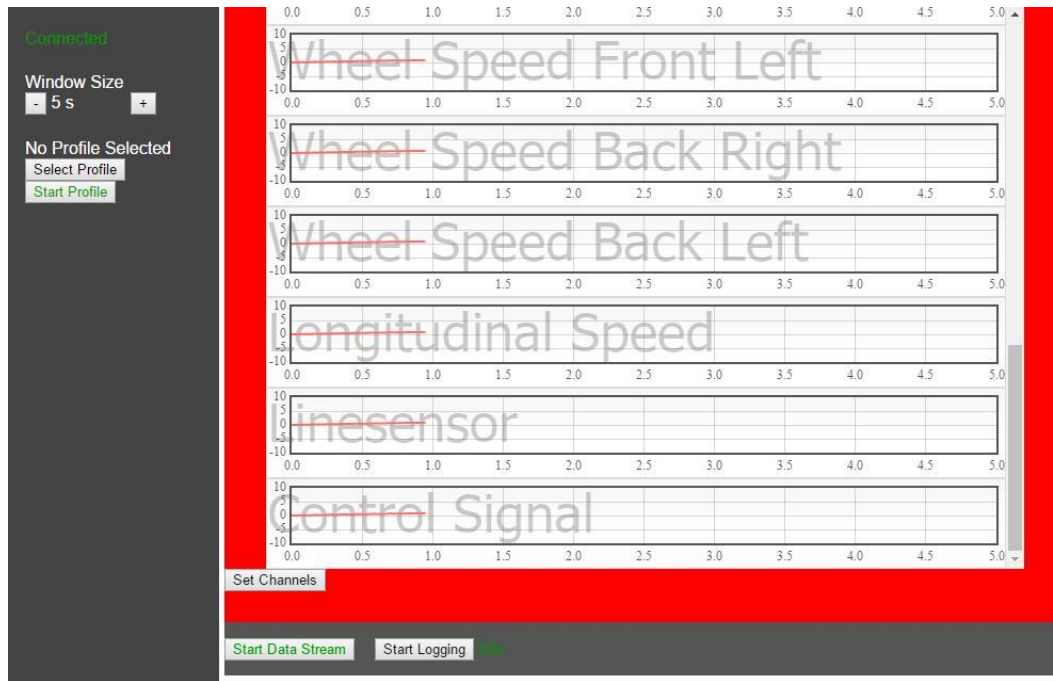


Figure 4.16 Web browser-based user interface

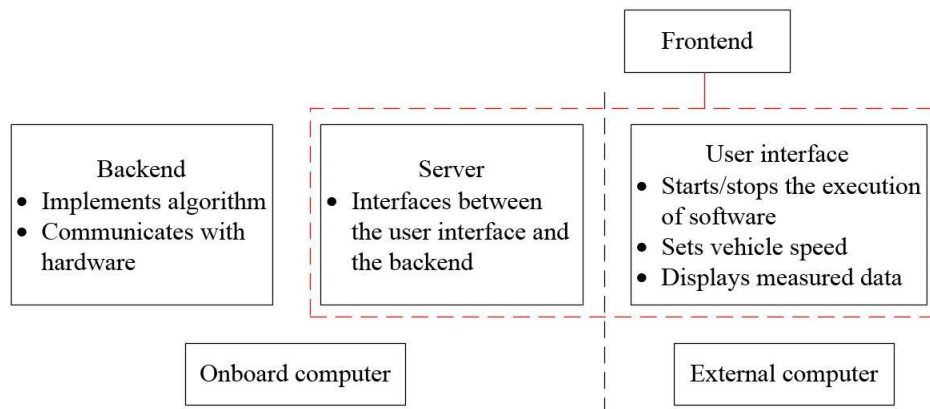


Figure 4.17 High-level system software overview

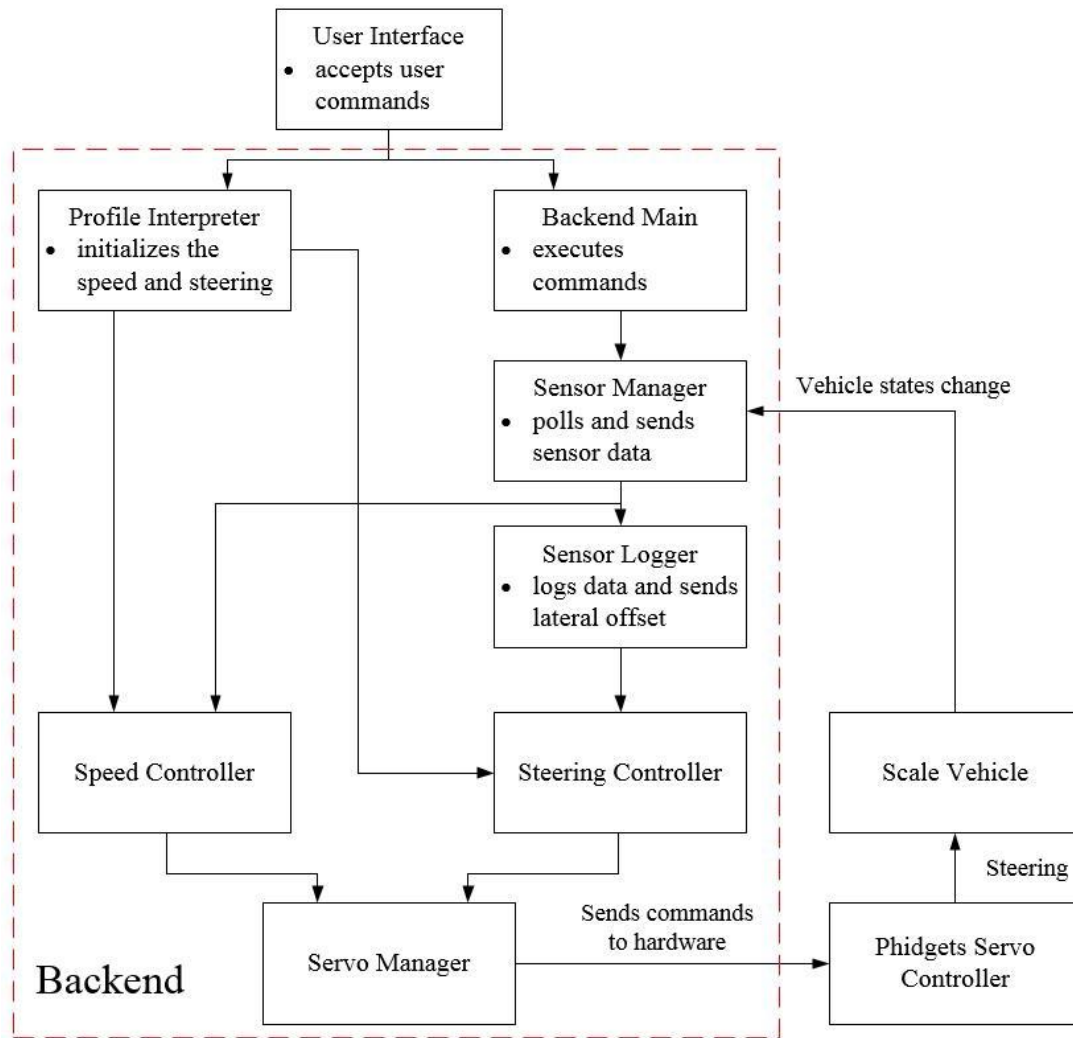


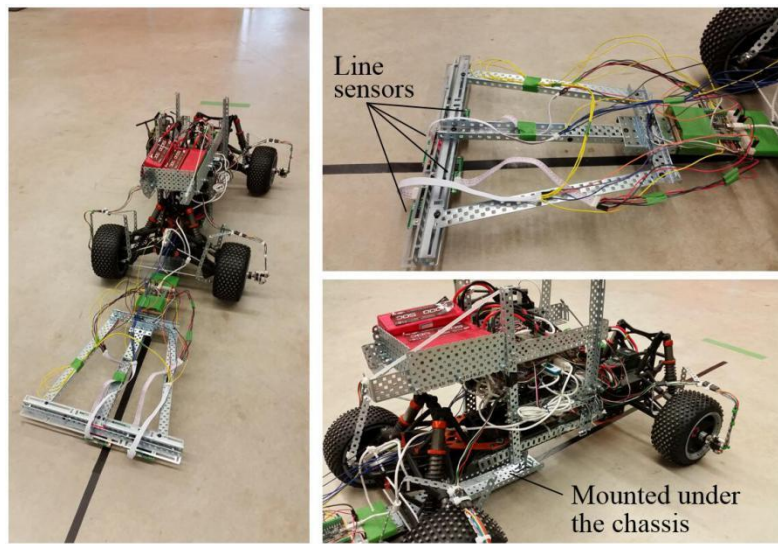
Figure 4.18 Backend software architecture

### 4.5.1.3 Look-ahead Sensing system

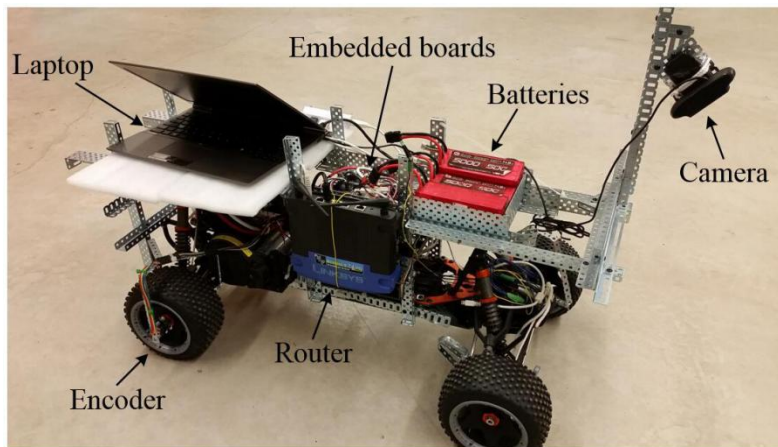
The retrofitted scaled vehicle adopting schemes A and B is respectively shown in Figure 4.19. As can be seen in Figure 4.19 (a), the line sensors are placed in the front of the scaled vehicle. A metal frame structure is mounted under the chassis to hold the line sensors. The schematic of the arrangement of the line sensors is shown in Figure 4.20. Five line sensors are mounted underneath the two parallel beams. The middle



photoelectric sensor of the third line sensor is on the longitudinal axis of the scaled vehicle, and its measurement of the lateral offset is zero when the longitudinal axis of the scaled vehicle and the road centerline are coincident. The measured lateral offsets are fixed values ranging from -12 cm to 12 cm with an increment of 1 cm. The Phidgets SBC plays the role of the onboard computer. The other Phidgets devices are connected to the SBC via USB.



(a)



(b)

Figure 4.19 Retrofitted scaled vehicle: (a) adopting scheme A; (b) adopting scheme B

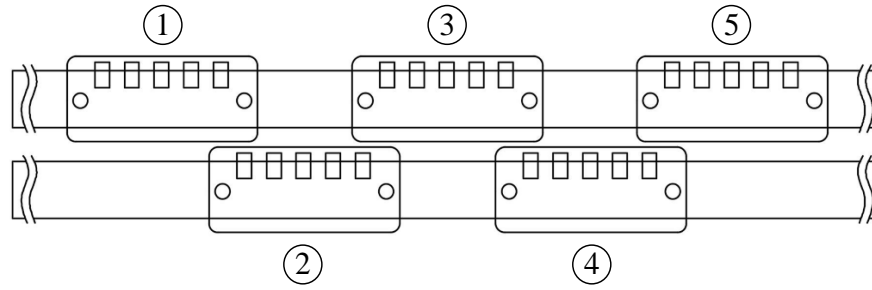


Figure 4.20 Arrangement of the line sensors underneath the beams in scheme A

In Figure 4.19 (b), a web camera is placed in the upper-front of the scaled vehicle. A metal frame structure is also built to fix the camera. Because the calculation required by the computer vision program exceeds the capacity of the Phidgets SBC, in which the CPU has only one core with a speed of 454 MHz, an laptop is used as the onboard computer. The retrofitted scaled vehicle can be seen in Figure 4.19 (b).

To choose a better look-ahead sensing scheme to estimate the lateral offset in the experiment, the advantages and disadvantages of schemes A and B are discussed as follows. The obvious advantage of scheme A is that its program implementation is much easier than that of scheme B. However, its sensing performance is easily degraded owing to the limited sensing distance of the line sensors. Specifically, because the typical sensing distance of the line sensors is 2 cm, the line sensors should be placed at a distance of 2 cm above the ground to obtain acceptable sensing performance. However, this leads to frequent collisions between the line sensors and the ground when the height of the chassis decreases owing to the turning of the front wheels. The line sensors invalidated by the collisions generate improper estimations of the lateral offset. Furthermore, the collisions could also be caused by the vibration of the metal frame structure when the scaled vehicle is running. The largest vibration amplitudes happen at the ends of the

beams. In addition, the uneven ground also causes the collisions between the line sensors and the ground.

In contrast, although the computer vision programming is more difficult, scheme B effectively avoids the above sensing difficulties of scheme A, because the detection range of the camera can be easily changed in the program or by adjusting the position of the camera. Moreover, scheme B can be easily implemented to a full-size vehicle in practice. In addition, owing to the installation restriction of the line sensors, the accuracy of the measured lateral offset is 1 cm. However, the accuracy of the computer vision can reach to 0.1 cm. Therefore, the sensing performance of scheme B is better and more consistent than that of scheme A.

The above comparisons between schemes A and B indicate that scheme B is a better choice for the look-ahead sensing system to estimate the lateral offset. The hardware diagram of the retrofitted scaled vehicle using the computer vision is shown in Figure 4.21. The estimation of the road centerline via computer vision in the experiment is shown in Figure 4.22. The computer vision program first detects the lane markers and estimates the position of the road centerline. Then the lateral offset is obtained by calculating the difference between the position of the road centerline and that of the scaled vehicle.

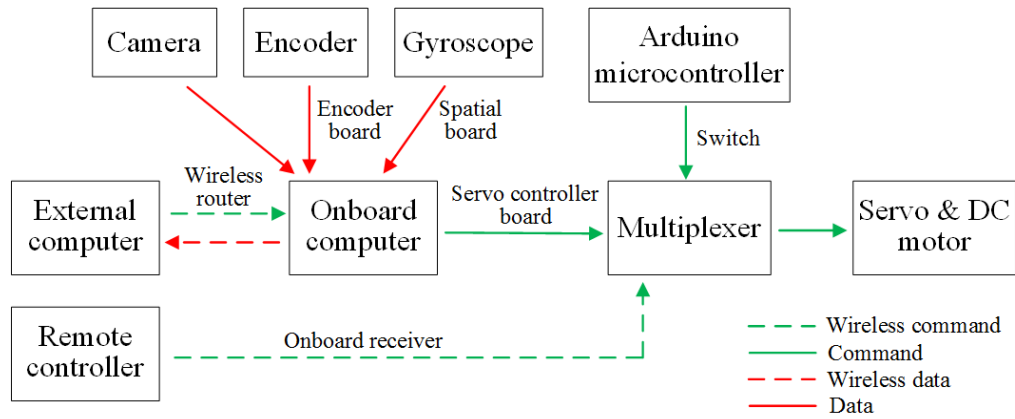


Figure 4.21 Hardware diagram of the retrofitted scaled vehicle using computer vision

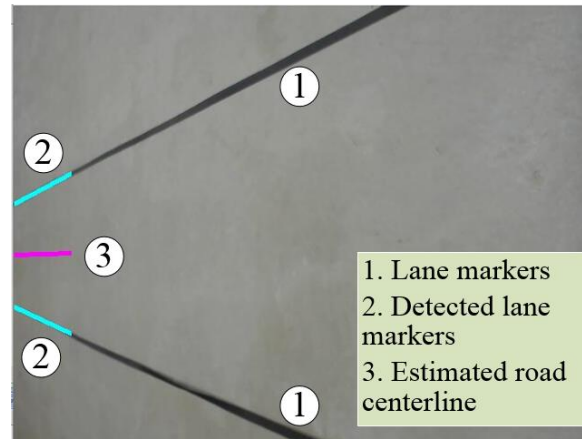


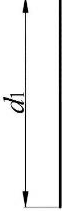
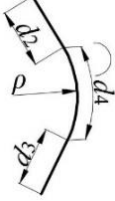
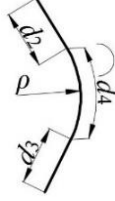
Figure 4.22 Estimation of the road centerline via computer vision in the experiment

## 4.5.2 Experimental Results

The goal of the experimental tests is to validate whether the scaled vehicle controlled by the ADRC controller can perform lane keeping. The experiments are conducted indoor in order to minimize unexpected risks. Considering that a normal road is made up of straight lanes and curved lanes, three paths are built to simulate the scenes that a vehicle would encounter on the normal road. The specifications of these three paths are described in Table 4.6. Path one is a straight lane on which the straight lane keeping ability of the

scaled vehicle is tested. Both paths two and three have two straight lanes and a curved lane in the middle, but the lengths of these two paths are different. Note that in path two and path three, the lane curvature changes twice at the two connections between the curved lane and the straight lanes. Taking path two as an example, at the connections, the lane curvature changes from  $\rho=0 \text{ m}^{-1}$  to  $\rho=0.04 \text{ m}^{-1}$  and from  $\rho=0.04 \text{ m}^{-1}$  to  $\rho=0 \text{ m}^{-1}$ , respectively. The vehicle runs from  $d_3$  to  $d_2$  on both paths. The scaled vehicle dimensions are: the mass  $m$  is 18.5 kg, the vertical inertial moment  $I_z$  is  $1.56 \text{ kg}\cdot\text{m}^2$ , the distances from the front and rear axes to the CG are 0.33 m and 0.255 m, respectively. The look-ahead distance is set to 1.5 m. The parameters of the ADRC steering controller are tuned to:  $w_o=6.6 \text{ rad/s}$ ,  $w_c=2 \text{ rad/s}$ , and  $b=40$ .

Table 4.6 Specifications of paths used in the experiments: straight lane keeping (Path one); curved lane keeping (Paths two and three).

Path one	Path two	Path three
		
$d_1=26.14 \text{ m}$	$\rho=0.04 \text{ m}^{-1}$ , $d_2=7.13 \text{ m}$ , $d_3=10.69 \text{ m}$ , $d_4=5.94 \text{ m}$	$\rho=0.05 \text{ m}^{-1}$ , $d_2=4.16 \text{ m}$ , $d_3=12.77 \text{ m}$ , $d_4=5.94 \text{ m}$

The scaled vehicle is controlled by the software in each test. Only when an unforeseen behavior occurs, the user intervenes and controls the vehicle manually. The automated steering control is activated when the vehicle starts to run from rest. Because the initial conditions of the vehicle system in different tests are different and many unmodeled

dynamics exist in the vehicle system, the lane keeping performance usually varies slightly from test to test. During the lane keeping, the lateral offset should be regulated within the acceptable range to ensure that the vehicle does not go off the road, and the oscillation period of the lateral offset should not be too small. The effectiveness of the proposed steering controller is evaluated by observing the amplitude and period of the lateral offset.

Figure 4.23 shows the lane keeping performances of the scaled vehicle controlled by the ADRC controller and a PID controller on Path one. The scaled vehicle is tested at two different longitudinal velocities. It is shown that the ADRC controller regulates the lateral offset within the small range of  $\pm 0.03$  m in both tests and the scaled vehicle is able to perform the straight lane keeping smoothly. In contrast, the PID controller regulates the lateral offset within the range of  $\pm 0.04$  m at  $v_x = 7.2$  km/h, while the lateral offset increases to larger amplitudes at  $v_x = 9$  km/h.

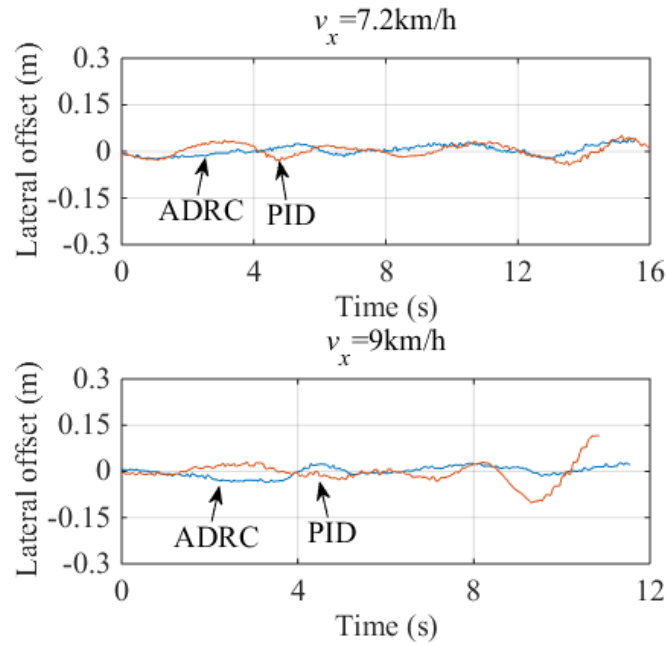


Figure 4.23 Lane keeping performances of the scaled vehicle controlled by the ADRC controller and the PID controller on path one

Figures 4.24 and 4.25 show the lane keeping performances of the scaled vehicle controlled by the ADRC controller and the PID controller on paths two and three, where the curved lane curvatures are  $0.04 \text{ m}^{-1}$  and  $0.05 \text{ m}^{-1}$ , respectively. The ADRC controller keeps the vehicle within the lane with maximum lateral offsets of 0.15 m on path two and 0.16 m on path three. The offset between the center point of the two front wheels and the road centerline is measured manually in the tests and it is less than 0.08 m. Comparing the responses of paths two and three, the increasing curvature results in slight increases in the maximum lateral offset during the cornering. After the reactions to the two curvature changes, the decreasing tendency of the lateral offset in each test shows that the lateral offset is gradually suppressed by the ADRC controller. By comparison, at  $v_x=7.2 \text{ km/h}$ , the PID controller regulates the lateral offset within the range of  $\pm 0.15 \text{ m}$  on both paths two and three. However, the oscillations of the lateral offsets are more frequent in comparison to the ADRC controller. At  $v_x=9 \text{ km/h}$ , the lateral offsets increase dramatically during the two curvature changes and the scaled vehicle cannot maintain its position within the lane.

Figure 4.26 shows the results of the steering angle, lateral acceleration, and yaw rate of the scaled vehicle, when the vehicle runs at  $9 \text{ km/h}$  on path three with  $0.05 \text{ m}^{-1}$  road curvature. The lateral acceleration and the yaw rate oscillate around zero with small amplitudes on the straight lane, increase during the cornering, and then decrease and oscillate around zero on the straight lane. Further tests are conducted over a period of time to ensure consistency of the results, as shown in Figure 4.27.

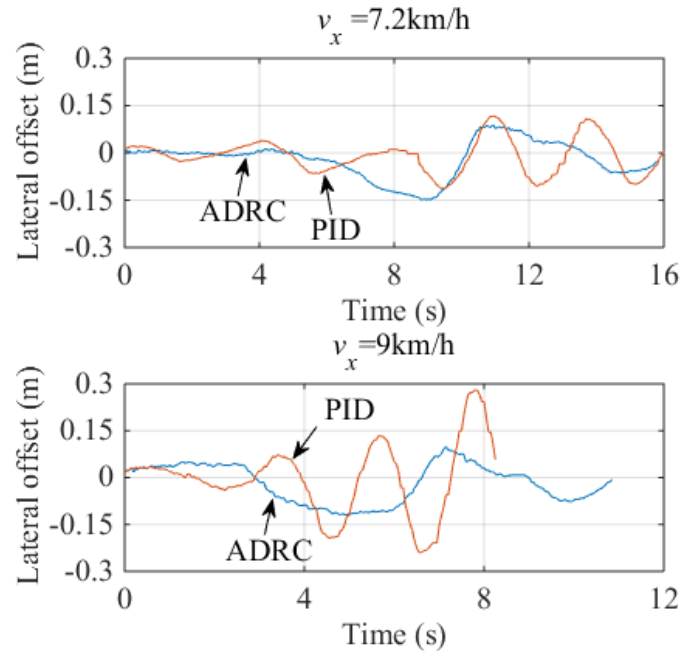


Figure 4.24 Lane keeping performances of the scaled vehicle controlled by the ADRC controller and the PID controller on path two ( $\rho=0.04 \text{ m}^{-1}$ )

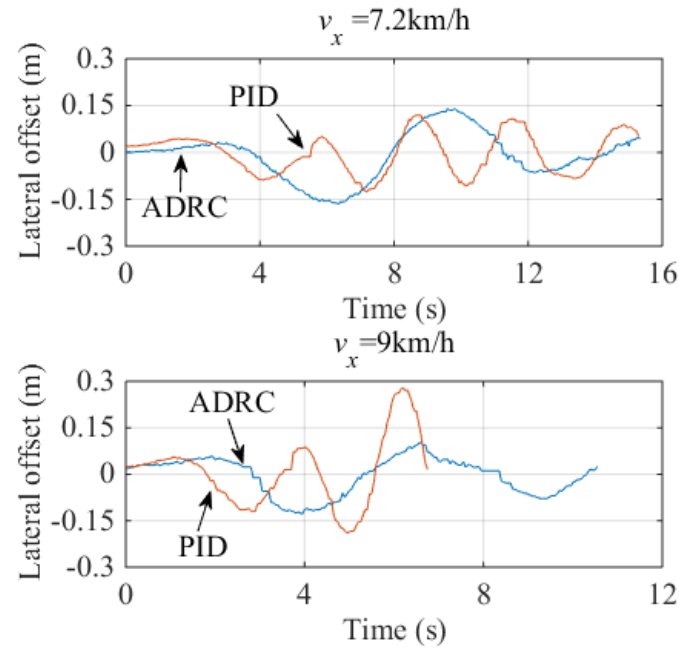


Figure 4.25 Lane keeping performances of the scaled vehicle controlled by the ADRC controller and the PID controller on path three ( $\rho=0.05 \text{ m}^{-1}$ )



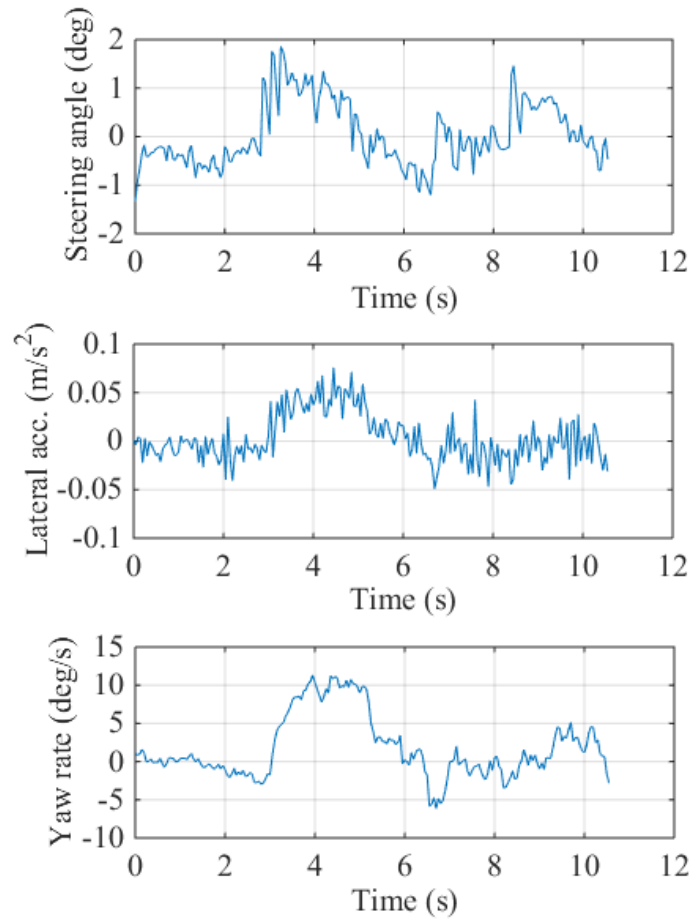


Figure 4.26 Steering angle, lateral acceleration and yaw rate of the scaled vehicle controlled by the ADRC controller during lane keeping on path three ( $v_x=9$  km/h,  $\rho=0.05$  m<sup>-1</sup>)

## 4.6 Summary

In this chapter, the ADRC was designed for the automated steering controller for lane keeping in autonomous vehicles. The ADRC controller actively estimated and compensated for the internal dynamics and the external disturbances. The stability of the control system was investigated using the concept of Lyapunov exponents. It was shown that the control system is exponentially stable around the equilibrium points. In the simulations, the vehicle controlled by the ADRC controller remained within the lane and

the lateral offset was regulated within 0.1 m. It was also shown that increasing the longitudinal velocity or the road curvature caused a larger lateral offset. The ADRC controller was further validated on the scaled vehicle. The experimental results showed that the vehicle performed the lane keeping successfully. The ADRC controller is simple, without requiring complex calculations and real-time measurements, and it is easy to implement in practice.

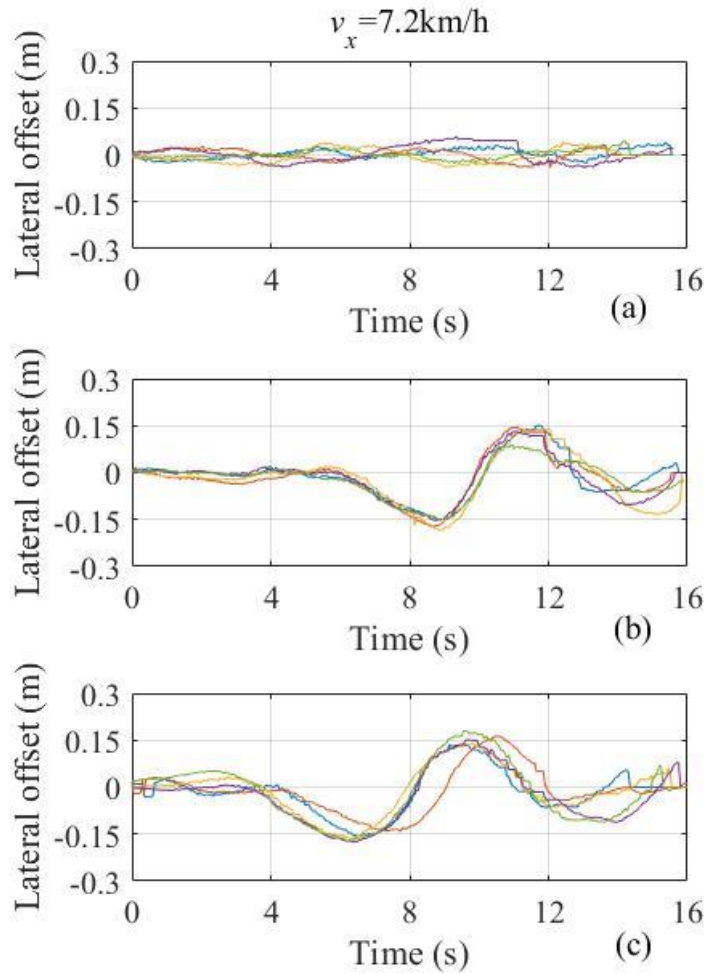


Figure 4.27 Straight and curved lane keeping results and each subfigure contains five separate tests conducted a period of time: (a) straight lane keeping; (b) curved lane keeping ( $\rho=0.04 \text{ m}^{-1}$ ); (c) curved lane keeping ( $\rho=0.05 \text{ m}^{-1}$ )

# Chapter 5

## Position Control of Hydraulic Actuators

In this chapter, the ADRC is applied to the position control of hydraulic actuators. First of all, a new method is proposed to tune the ADRC for controlling high-order systems using the QFT. Second, the ADRC is designed for the electro-hydrostatic actuator and the electro-hydraulic actuator. Third, both simulations and experiments are conducted to validate the ADRC controllers.

### **5.1 Quantitative Feedback Theory Design of ADRC**

In this section, the ADRC is transformed from the state space to the frequency domain. Based on this, a new tuning method is proposed to tune the ADRC using the QFT.

#### **5.1.1 Laplace Transform of ADRC**

Referring to Chapter 3.2, the linear ADRC is given as follows:

$$\left\{ \begin{array}{l} \text{ESO:} \\ \dot{\bar{x}} = A\bar{x} + Bu + L(y - \bar{y}) \\ \bar{y} = C\bar{x} \\ \text{Control law :} \\ u = \frac{k_1(R - \bar{x}_1) + k_2(\dot{R} - \bar{x}_2) + \dots + k_n(R^{(n-1)} - \bar{x}_n) - \bar{x}_{n+1}}{b} \end{array} \right.$$

Taking the Laplace transform of the ESO and the control law, we have:

$$s\bar{X}(s) = (A - LC)\bar{X}(s) + BU(s) + LY(s) \quad (5.1)$$

$$U(s) = K(\bar{R}(s) - \bar{X}(s)) \quad (5.2)$$

with

$$K = \frac{[k_1 \ k_2 \ \dots \ k_n \ 1]}{b}$$

$$\bar{R}(s) = R(s)[1 \ s \ \dots \ s^{(n-1)} \ 0]^T$$

where  $\bar{X}(s)$ ,  $U(s)$ ,  $Y(s)$ , and  $\bar{R}(s)$  are the Laplace transforms of  $\bar{x}$ ,  $u$ ,  $y$ , and  $\bar{R}$ , respectively.

Solving (5.1) for  $\bar{X}(s)$ , we have:

$$\bar{X}(s) = (sI - A + LC)^{-1}(BU(s) + LY(s)) \quad (5.3)$$

Substituting (5.3) into (5.2):

$$U(s) = K(\bar{R}(s) - (sI - A + LC)^{-1}(BU(s) + LY(s))) \quad (5.4)$$

Rearranging (5.4):

$$(1 + K(sI - A + LC)^{-1}B)U(s) = K\bar{R}(s) - K(sI - A + LC)^{-1}LY(s) \quad (5.5)$$

Equation (5.5) can be rewritten as:

$$U(s) = \frac{D_2(s)}{D_1(s)} \left( \frac{D_3(s)}{D_2(s)} R(s) - Y(s) \right) = G(s)(H(s)R(s) - Y(s)) \quad (5.6)$$

where

$$G(s) = \frac{D_2(s)}{D_1(s)} = \frac{K(sI - A + LC)^{-1}L}{1 + K(sI - A + LC)^{-1}B} \quad (5.7)$$

$$H(s) = \frac{D_3(s)}{D_2(s)} = \frac{K[1 \ s \ \dots \ s^{(n-1)} \ 0]^T}{K(sI - A + LC)^{-1}L} \quad (5.8)$$

Given that the transfer function of the plant is denoted as  $P(s)=Y(s)/U(s)$ , (5.6) shows that the ADRC and the plant  $P(s)$  constitute a two degree-of-freedom feedback system, as shown in Figure 3.5, where the ADRC is decomposed into two parts: the controller  $G(s)$  and the prefilter  $H(s)$ . It is also shown that the structures of the controller  $G(s)$  and the prefilter  $H(s)$  are determined by (5.7) and (5.8), as long as the order of the plant  $P(s)$  is known. For example, considering that  $P(s)$  is a second-order system, the structures of  $G(s)$  and  $H(s)$  determined by (5.7) and (5.8) are:

$$G(s) = \frac{g_1}{s} \frac{s^2 + g_2s + g_3}{s^2 + g_4s + g_5} \quad (5.9)$$

$$H(s) = \frac{h_1s^4 + h_2s^3 + h_3s^2 + h_4s + h_5}{bg_1(s^2 + g_2s + g_3)} \quad (5.10)$$

where

$$\begin{cases} g_1 = (l_3 + l_1 k_1 + l_2 k_2)/b \\ g_2 = (l_2 k_1 + l_3 k_2)/(l_3 + l_1 k_1 + l_2 k_2) \\ g_3 = l_3 k_1/(l_3 + l_1 k_1 + l_2 k_2) \\ g_4 = l_1 + k_2 \\ g_5 = l_2 + k_1 + l_1 k_2 \end{cases} \quad (5.11)$$

$$\begin{cases} h_1 = k_2 \\ h_2 = k_1 + l_1 k_2 \\ h_3 = l_1 k_1 + l_2 k_2 \\ h_4 = l_2 k_1 + l_3 k_2 \\ h_5 = l_3 k_1 \end{cases} \quad (5.12)$$

Tuning the second-order ADRC is to determine the coefficients  $g_1$ ,  $g_2$ ,  $g_3$ ,  $g_4$ , and  $g_5$  in  $G(s)$ . Once the coefficients in  $G(s)$  are determined, the coefficients in  $H(s)$  can be obtained by estimating the controller signal gain  $b$  and solving the coefficient equations (5.11). Obviously, the prefilter  $H(s)$  determined in this way relies on the estimation of  $b$ . Because  $b$  is uncertain owing to parametric uncertainties in practice, the performance of the ADRC is easily affected by an improper estimation of  $b$ . Therefore, estimating  $b$  and then obtaining  $H(s)$  causes difficulties in the tuning of the ADRC and the realization of satisfactory performance. Furthermore, note that the degree of the numerator of  $H(s)$  is greater than the degree of the denominator; the frequency response indicates that  $H(s)$  could potentially amplify the high-frequency components in the reference signal, which would cause a sudden jump in the control signal. Therefore,  $H(s)$  must be redesigned. Because the role of  $H(s)$  is to generate a smooth profile for the system to track, it can be replaced by a simpler function that acts as a low-pass filter. Doing so allows the prefilter  $H(s)$  and the controller  $G(s)$  to be designed separately in the frequency domain.

### 5.1.2 Tuning of ADRC

The decomposed controller  $G(s)$  and prefilter  $H(s)$  of the ADRC are tuned in the framework of the QFT. Given a plant with parametric uncertainties, the tuning procedure involves the following steps:

- 1) Generate the plant  $P(s)$  templates at the selected frequencies on the Nichols chart.

The template at a selected frequency denotes the collection of the frequency responses of the uncertain plant.

- 2) Define the closed-loop performance specifications and convert them into certain bounds on a nominal open-loop transfer function  $L_n(s) = P_n(s) \cdot G(s)$ , where  $P_n(s)$  is the nominal plant.

- 3) Determine the structure of the controller  $G(s)$  by using (5.7), and perform the loop shaping of  $L_n(s)$  to satisfy the bounds. Once an acceptable  $L_n(s)$  is obtained, the locations of the poles and zeroes of the controller  $G(s)$  can be obtained by  $G(s) = L_n(s) / P_n(s)$ .

- 4) Design a prefilter  $H(s)$  to shift the closed-loop frequency responses within the tracking bounds. The design of  $H(s)$  is indeed straightforward. It can be done by adding poles and zeros such that the frequency responses of the closed-loop control system fall within the tracking bounds.

In the following sections, the ADRC tuned by the proposed tuning method is applied to hydraulic actuators. The hydraulic actuators are a fourth-order electro-hydrostatic actuator and a fifth-order electro-hydraulic actuator. The test bed of the actuators is shown in Figure 5.1. The details of the electro-hydrostatic and electro-hydraulic circuits are

introduced accordingly in the following sections. Tuning the ADRC for the hydraulic actuators using the bandwidth tuning method is found to be challenging, because tuning the only two observer and controller bandwidths restricts the performance of the ADRC [33].

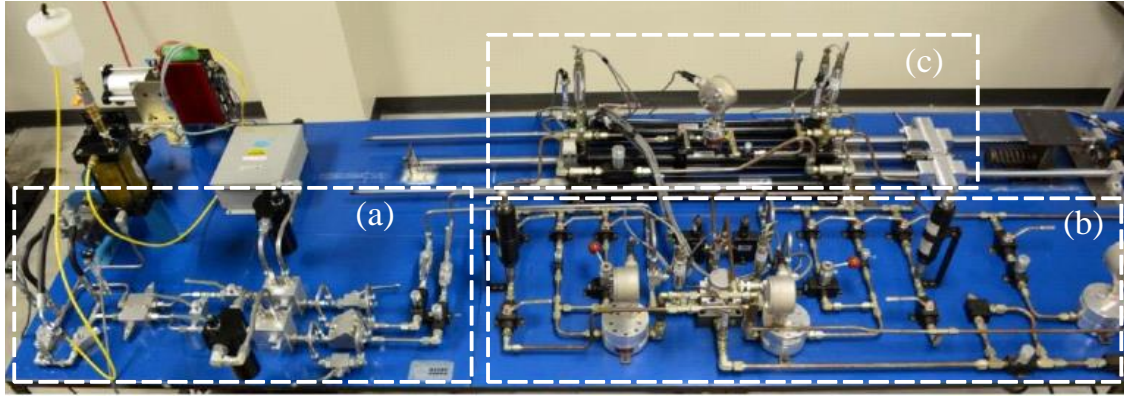


Figure 5.1 Test bed: (a) electro-hydrostatic circuit; (b) electro-hydraulic circuit; (c) hydraulic actuator

## 5.2 Position Control of Electro-Hydrostatic Actuator

An electro-hydrostatic actuator (EHA) is well-known for its simple and compact structure, easy maintenance, and low oil pollution and heat loss. It is a widely used element in vehicles and airplanes. Figure 5.2 presents a schematic of the EHA, where the servo motor actuates the fixed hydraulic pump, two ports of the pump are connected to two chambers of the actuator, and the external load is applied to one side of the actuator. The goal of the controller design is to track the desired actuator position under the influence of parametric uncertainties and internal leakage between the two chambers. The EHA model developed in [29] is considered:



$$P(s) = \frac{K_m q_b A}{\left\{ Bs \left( \frac{s^2}{w_n^2} + \frac{2\zeta s}{w_n} + 1 \right) + 2kK_i \right\}} \cdot \frac{1}{\pi \left( \frac{1}{\tau_m} s + 1 \right)} \quad (5.13)$$

where

$$B = \left[ 2A^2 + \frac{k(V_0 + V_{\text{pipe}})}{\beta} + 2K_i f \right]$$

$$w_n = \sqrt{\left[ 2A^2 \beta + k(V_0 + V_{\text{pipe}}) + 2\beta K_i f \right] / \left[ m(V_0 + V_{\text{pipe}}) \right]}$$

$$\zeta = \sqrt{\frac{\left[ 2m\beta K_i + f(V_0 + V_{\text{pipe}}) \right]^2}{4m(V_0 + V_{\text{pipe}}) \left[ 2A^2 \beta + k(V_0 + V_{\text{pipe}}) + 2\beta K_i f \right]}}$$

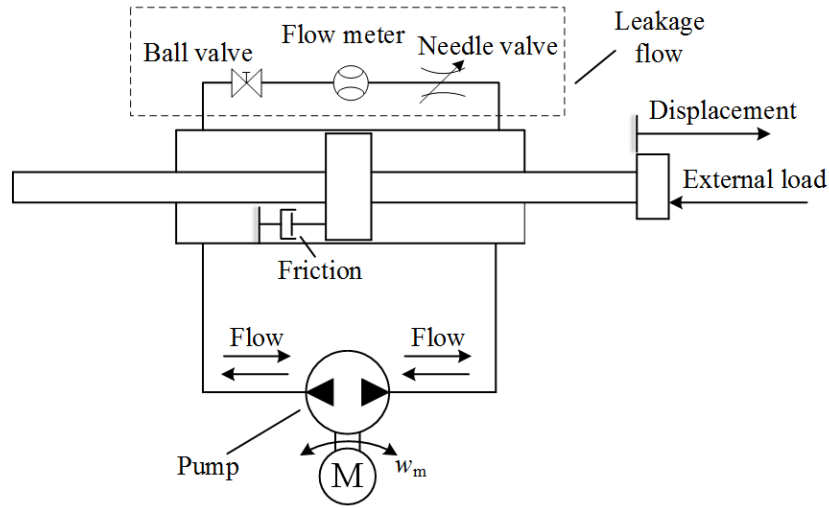


Figure 5.2 Schematic of the EHA

The parameters in the EHA model (5.13) are given in Table 5.1. To avoid conflict, the symbols are only assumed applicable for this section. Note that  $K_i$ ,  $k$ ,  $f$ ,  $\beta$ , and  $m$  are the uncertain parameters in the EHA model.

Table 5.1 Parameters of the EHA model

Symbol	Nominal	Range
$\tau_m(\text{s}^{-1})$	20	-
$K_m(\text{rad/s} \cdot \text{V})$	25	-
$q_b(\text{m}^3/\text{rev})$	$4.9 \times 10^{-6}$	-
$V_0(\text{m}^3)$	$192 \times 10^{-6}$	-
$V_{\text{pipe}}(\text{m}^3)$	$42 \times 10^{-6}$	-
$A(\text{m}^2)$	$633 \times 10^{-6}$	-
$K_i(\text{m}^3/\text{s} \cdot \text{Pa})$	0	$0-2.4 \times 10^{-11}$
$k(\text{N/m})$	$60 \times 10^3$	$0-130 \times 10^3$
$f(\text{N} \cdot \text{s/m})$	250	100-400
$\beta(\text{Pa})$	$689 \times 10^6$	$356 \times 10^6-1030 \times 10^6$
$m(\text{kg})$	12.3	11-13.5

### 5.2.1 Controller Design

Starting from the first step of the tuning procedure, the templates that characterize the parametric uncertainties are generated at the selected frequencies on the Nichols chart, as shown in Figure 5.3. Each template represents the collection of the frequency responses of the EHA model owing to the parametric uncertainties at a selected frequency. The ADRC-EHA system is designed to meet the following closed-loop performance specifications.

*Reference tracking:* the transfer function of the closed-loop control system

$$T(s) = H(s) \frac{G(s)P(s)}{1 + G(s)P(s)} \quad (5.14)$$

should satisfy the following inequality to meet the tracking requirement:

$$|T_L(jw)| \leq |T(jw)| \leq |T_U(jw)| \quad \forall w \in [0, \infty) \quad (5.15)$$

where

$$T_L(jw) = \frac{6.66 \times 10^7}{(jw + 5)(jw + 9)(jw + 37)(jw + 200)^2}$$

$$T_U(jw) = \frac{7.66(jw + 4.7)(jw + 40)}{(jw + 6)(jw + 8)(jw + 30)}$$

The lower bound  $T_L(jw)$  has no overshoot with a 2% settling time of 0.98 s. The upper bound  $T_U(jw)$  has 1.66% overshoot with a 2% settling time of 0.29 s.

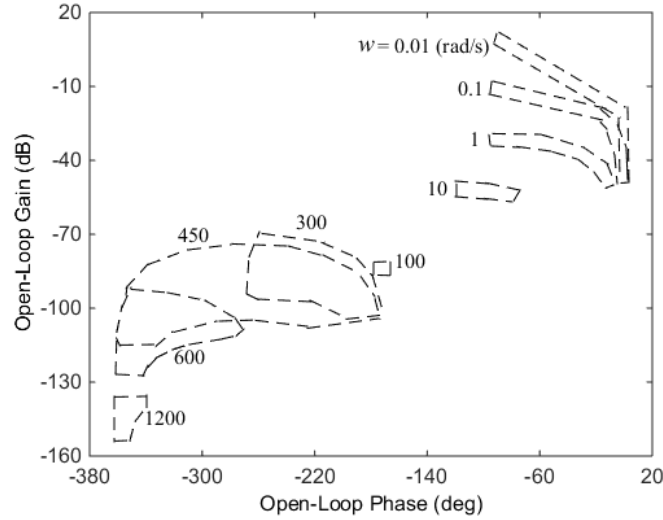


Figure 5.3 Templates of the EHA model at selected frequencies

*Closed-loop stability:* the following inequality must be also satisfied to ensure that the system has a 4.22 dB gain margin and  $36.42^\circ$  phase margin:

$$\left| \frac{G(jw)P(jw)}{1 + G(jw)P(jw)} \right| \leq \delta = 1.6 \quad \forall w \in [0, \infty) \quad (5.16)$$

The tracking and stability specifications are converted to the constraints on the normal open-loop transfer function  $L_n(s)$ . These constraints are represented as bounds at the

selected frequencies on the Nichols chart, as shown in Figure 5.4. Before performing the loop shaping of  $L_n(s)$ , because EHA is a fourth-order system, a fourth-order ADRC is used to control the EHA. The structure of the controller  $G(s)$  is determined by (5.7) as:

$$G(s) = \frac{g_1}{s} \frac{s^4 + g_2 s^3 + g_3 s^2 + g_4 s + g_5}{s^4 + g_6 s^3 + g_7 s^2 + g_8 s + g_9} \quad (5.17)$$

The nominal open-loop transfer function  $L_n(s)$  is shaped to meet all the bounds at the relevant frequencies. Specifically,  $L_n(s)$  is required to be above the tracking bounds, and be outside the stability bounds at each selected frequency on the Nichols chart. An acceptable  $L_n(s)$  is shown in Figure 5.4. The resulting controller  $G(s)$  is determined as:

$$G(s) = \frac{3600}{s} \cdot \frac{(s/68+1)(s/45+1)(s/11.5+1)(s/11+1)}{(s/77+1)(s/76+1)(s/60+1)(s/50+1)} \quad (5.18)$$

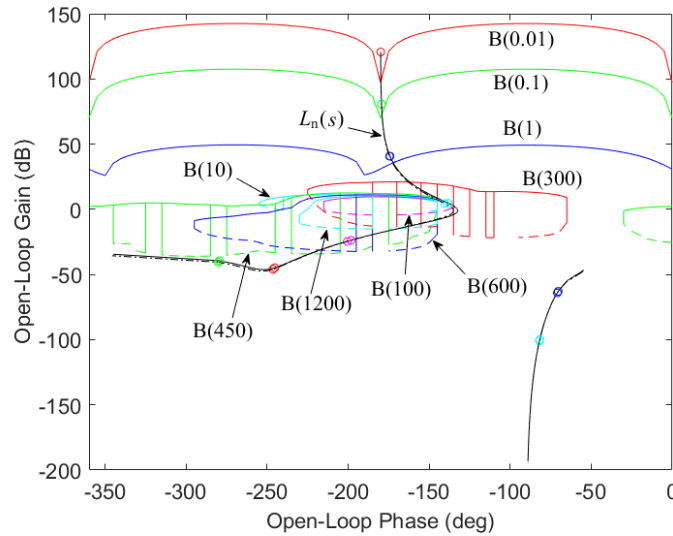


Figure 5.4 Bounds  $B(w)$ , and the acceptable nominal open-loop transfer functions  $L_n(s)$  for the fourth-order ADRC (solid line) and the second-order ADRC (dash-dotted)

To avoid the sudden jump in the control signal in practice, a prefilter  $H(s)$  is designed to shift the frequency responses of the closed-loop control system within the tracking bounds, as shown in Figure 5.5. This acceptable  $H(s)$  is shown as follows:

$$H(s) = \frac{(s/20 + 1)(s/23.5 + 1)}{(s/5 + 1)(s/8 + 1)} \quad (5.19)$$

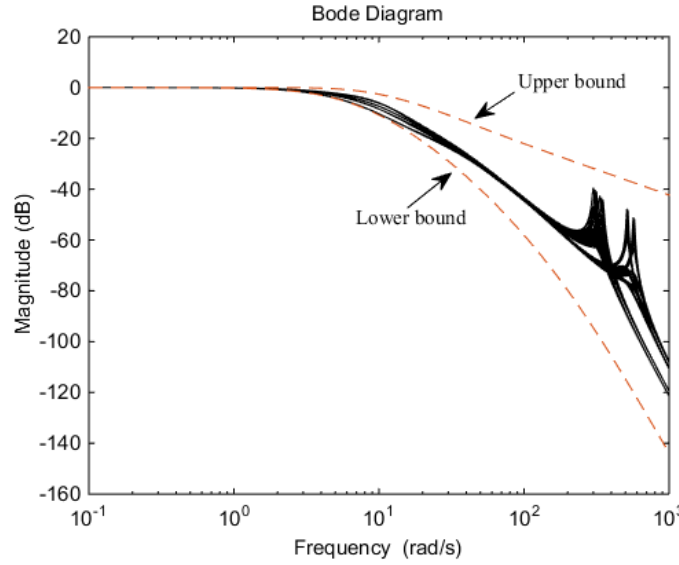


Figure 5.5 Frequency responses of the control system with parametric uncertainties

The orders of the plant and the ADRC are required to be equal in the framework of the ADRC. This feature results in a complicated controller  $G(s)$  when the plant is a high-order system. In many practical applications, real-time limitations on the computational resources require the reduction in the controller complexity [82]. It is found that tuning the ADRC using the proposed tuning method can break this constraint, i.e., the order of the ADRC can be less than the order of the plant. To illustrate this finding, in the following, a second-order ADRC is designed to control the plant (5.13). The structure of the controller  $G(s)$  is the same as (5.9). Applying the same tracking and stability

specifications of (5.15) and (5.16), an acceptable normal open-loop transfer function  $L_n(s)$  is shown in Figure 5.4. The resulting controller  $G(s)$  is given by:

$$G(s) = \frac{3600}{s} \frac{(s/12+1)(s/11+1)}{(s/75+1)(s/70+1)} \quad (5.20)$$

### 5.2.2 Bounded-Input Bounded-Output Stability

The bounded-input bounded-output (BIBO) stability of the control system in which a fourth-order EHA plant is controlled by a second-order ADRC is investigated in the following part. Note that this BIBO stability analysis can apply to control systems in which the order of the ADRC is lower than the order of the plants. Consider the EHA model (5.13) represented by the following equation:

$$\ddot{y} = F(y^{(4)}, y^{(3)}, \dot{y}, y) + bu(t) \quad (5.21)$$

which can be expressed in the state space form:

$$\begin{cases} \dot{x}_1 = x_2 \\ \dot{x}_2 = x_3 + bu \\ \dot{x}_3 = h \end{cases} \quad (5.22)$$

where  $x_1 = y$ ,  $x_2 = \dot{y}$ ,  $x_3 = F$ , and  $h = \dot{F}$ .

The ESO for (5.22) is designed as:

$$\begin{cases} \dot{\bar{x}}_1 = \bar{x}_2 + l_1(x_1 - \bar{x}_1) \\ \dot{\bar{x}}_2 = \bar{x}_3 + l_2(x_1 - \bar{x}_1) + bu \\ \dot{\bar{x}}_3 = l_3(x_1 - \bar{x}_1) \end{cases} \quad (5.23)$$

where  $\bar{x}_1$ ,  $\bar{x}_2$ , and  $\bar{x}_3$  are the observer states.  $l_1$ ,  $l_2$ , and  $l_3$  are the observer gains. With properly tuned observer gains, the observer states  $\bar{x}_1$ ,  $\bar{x}_2$ , and  $\bar{x}_3$  track the system states  $x_1$ ,  $x_2$ , and  $x_3$ ,

Let  $\hat{x}_i = x_i - \bar{x}_i$ ,  $i=1, 2, 3$ . The estimation errors between (5.22) and (5.23) can be expressed as:

$$\begin{cases} \dot{\hat{x}}_1 = \dot{x}_1 - \dot{\bar{x}}_1 = \hat{x}_2 - l_1 \hat{x}_1 \\ \dot{\hat{x}}_2 = \dot{x}_2 - \dot{\bar{x}}_2 = \hat{x}_3 - l_2 \hat{x}_1 \\ \dot{\hat{x}}_3 = \dot{x}_3 - \dot{\bar{x}}_3 = h - l_3 \hat{x}_1 \end{cases} \quad (5.24)$$

Let  $\hat{x} = [\hat{x}_1, \hat{x}_2, \hat{x}_3]^T$ , (5.24) can be written as:

$$\dot{\hat{x}} = A\hat{x} + Bh = \begin{bmatrix} -l_1 & 1 & 0 \\ -l_2 & 0 & 1 \\ -l_3 & 0 & 0 \end{bmatrix} \begin{bmatrix} \hat{x}_1 \\ \hat{x}_2 \\ \hat{x}_3 \end{bmatrix} + \begin{bmatrix} 0 \\ 0 \\ 1 \end{bmatrix} h \quad (5.25)$$

Assuming  $h$  is bounded, the observer gains are tuned such that the matrix  $A$  is Hurwitz, therefore, the estimation errors are BIBO stable [4]. Next, let  $e_i = R_i - x_i$ ,  $i=1, 2, 3$ ,  $R_1=R$ ,  $R_2=\dot{R}$ ,  $R_3=\ddot{R}$ , and  $R$  is the reference input. The control law is then designed as:

$$u = \frac{k_1(R_1 - \bar{x}_1) + k_2(R_2 - \bar{x}_2) - \bar{x}_3}{b} = \frac{k_1(e_1 + \hat{x}_1) + k_2(e_2 + \hat{x}_2) - (x_3 - \hat{x}_3)}{b} \quad (5.26)$$

The tracking errors between the reference input and system states can be expressed as:

$$\begin{cases} \dot{e}_1 = \dot{R}_1 - \dot{x}_1 = R_2 - x_2 = e_2 \\ \dot{e}_2 = \dot{R}_2 - \dot{x}_2 = R_3 - k_1(e_1 + \hat{x}_1) - k_2(e_2 + \hat{x}_2) - \hat{x}_3 \end{cases} \quad (5.27)$$

Let  $e = [e_1, e_2]^T$ , (5.27) can be written as:

$$\dot{e} = A_e e + B_e \hat{x} + R_3 \quad (5.28)$$

where

$$A_e = \begin{bmatrix} 0 & 1 \\ -k_1 & -k_2 \end{bmatrix}; \quad B_e = \begin{bmatrix} 0 & 0 & 0 \\ -k_1 & -k_2 & -1 \end{bmatrix}$$

Because  $\hat{x}$  and  $R_3$  are bounded, the controller gains are tuned such that the matrix  $A_e$  is Hurwitz; therefore, the tracking errors are BIBO stable.

### 5.2.3 Simulations and Experiments

Simulations are first conducted to validate the effectiveness of the fourth-order ADRC and the second-order ADRC. Figure 5.6 shows the step responses of the ADRC tuned by the proposed tuning method and a fourth-order ADRC tuned by the bandwidth tuning method. The uncertain parameters range from small to large values. It is shown that the responses of the ADRC tuned by the proposed tuning method fall within the upper and lower bounds, but the responses of the ADRC tuned by the bandwidth tuning method are unable to fit in the bounds. Increasing the bandwidths could ensure better tracking performance; however, according to the pole-zero maps of the closed-loop control system, shown in Figure 5.7, as the observer bandwidth  $w_o$  increases from 75 rad/s to 76 rad/s, some poles pass the imaginary axis and enter the right-half plane and the control system becomes unstable. Therefore, the ADRC tuned by the bandwidth tuning method fails to meet the tracking specification.



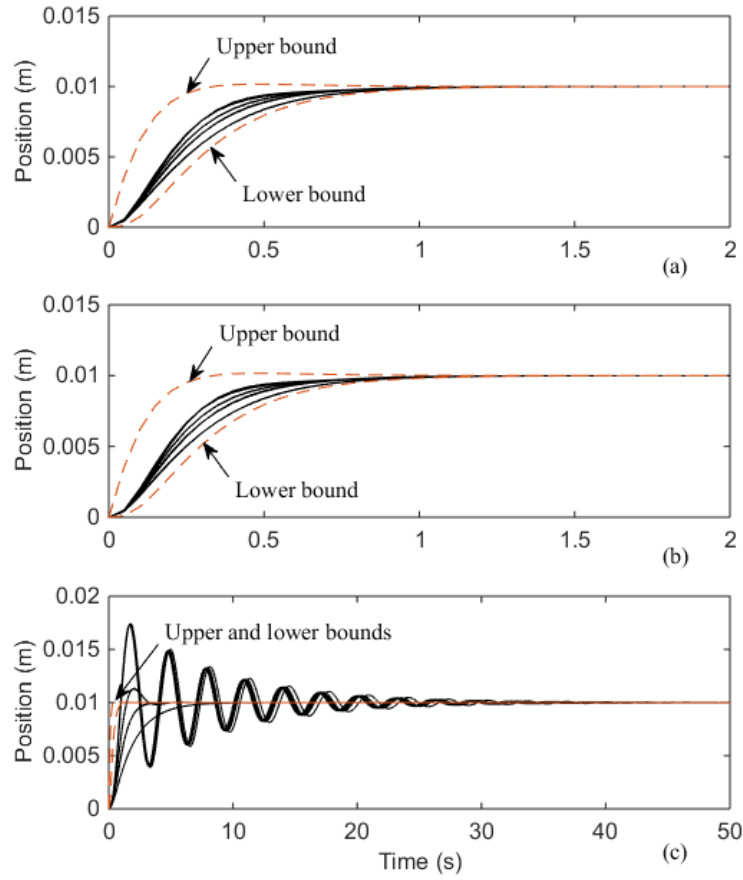


Figure 5.6 Step responses of the control system with parameter variations in the simulations: (a) fourth-order ADRC tuned by the proposed tuning method; (b) second-order ADRC tuned by the proposed tuning method; (c) fourth-order ADRC tuned by the bandwidth tuning method ( $w_o=75$  rad/s,  $w_c=71$  rad/s)

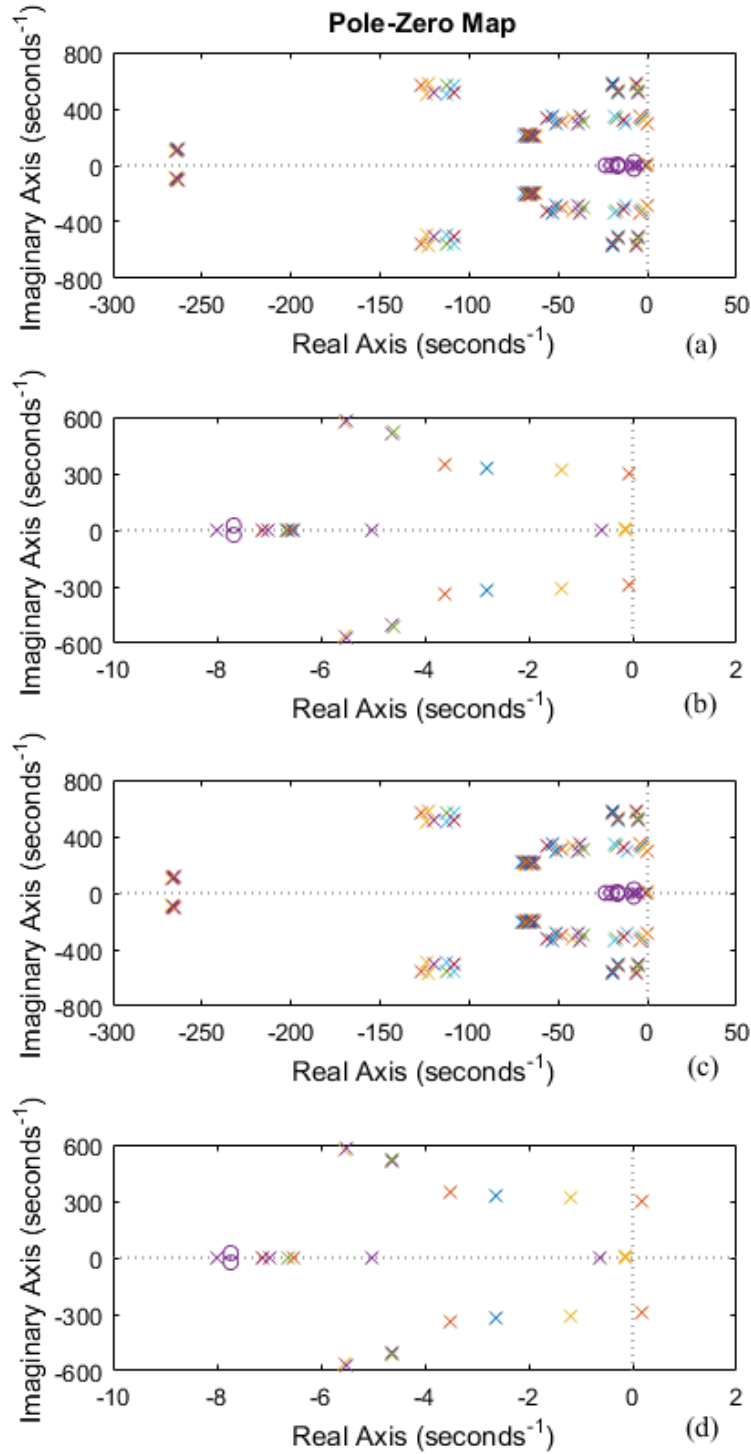


Figure 5.7 Pole-zero maps of the ADRC control system (with parameter variations) tuned by the bandwidth tuning method: (a)  $w_o=75$  rad/s,  $w_c=71$  rad/s; (b) partial enlargement of (a); (c)  $w_o=76$  rad/s,  $w_c=71$  rad/s; (d) partial enlargement of (c).

The fourth-order ADRC and the second-order ADRC, both tuned by the proposed tuning method, are applied to the EHA in the experiment. The 0.01 m square-wave responses against a 125 kN/m spring and increasing leakage flow are shown in Figure 5.8. The partial enlargements (time is from 6 s to 15 s) of the position responses shown in Figure 5.8 (a) are demonstrated in Figure 5.9. It is shown that the position responses of the actuator fall in the desired tracking bounds. The fourth-order ADRC and the second-order ADRC perform equally well with the fault-tolerant controller developed in [29].

Using the bandwidth tuning method to tune the ADRC for controlling the EHA with parametric uncertainties is challenging. The proposed tuning method considers the parametric uncertainties during the tuning stage and tunes the ADRC in the frequency domain according to the prescribed performance specifications. Therefore, the proposed tuning method eliminates the difficulties of tuning a large number of gains by trial and error, and the performance of the ADRC is improved. Furthermore, it is found that the order of the ADRC is not necessarily strictly the same as the order of the plant. In this application, the proposed tuning method tunes the ADRC whose order is lower than that of the plant. Based on the proposed tuning method, the ADRC can be applied to high-order systems with parametric uncertainties, without increasing the design and implementation difficulties.

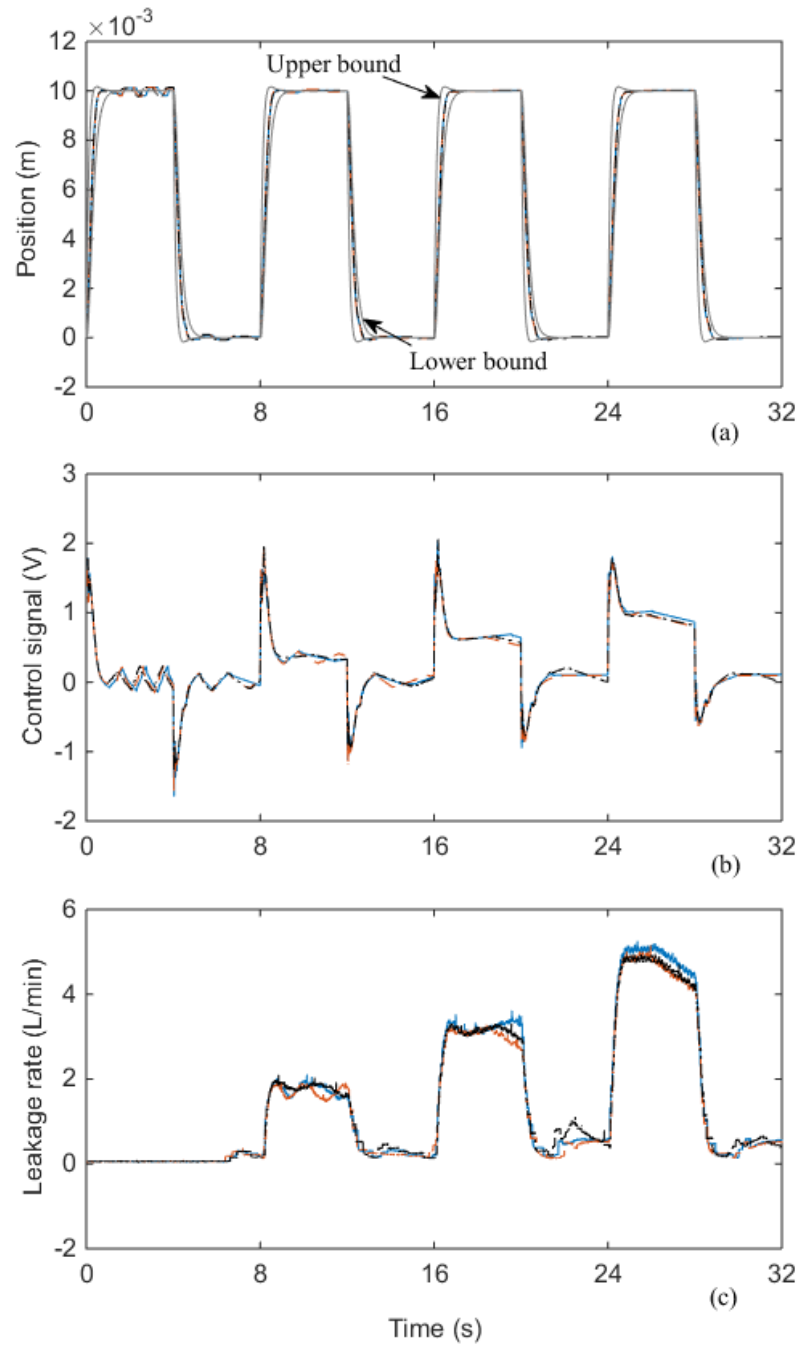


Figure 5.8 Experimental responses of 0.01 m square-wave reference against 125 kN/m spring and increasing leakage flow: (a) position; (b) control signal; (c) leakage rate. (Solid line: fourth-order ADRC tuned by the proposed tuning method; dashed: second-order ADRC tuned by the proposed tuning method; dash-dotted: fault-tolerant controller)

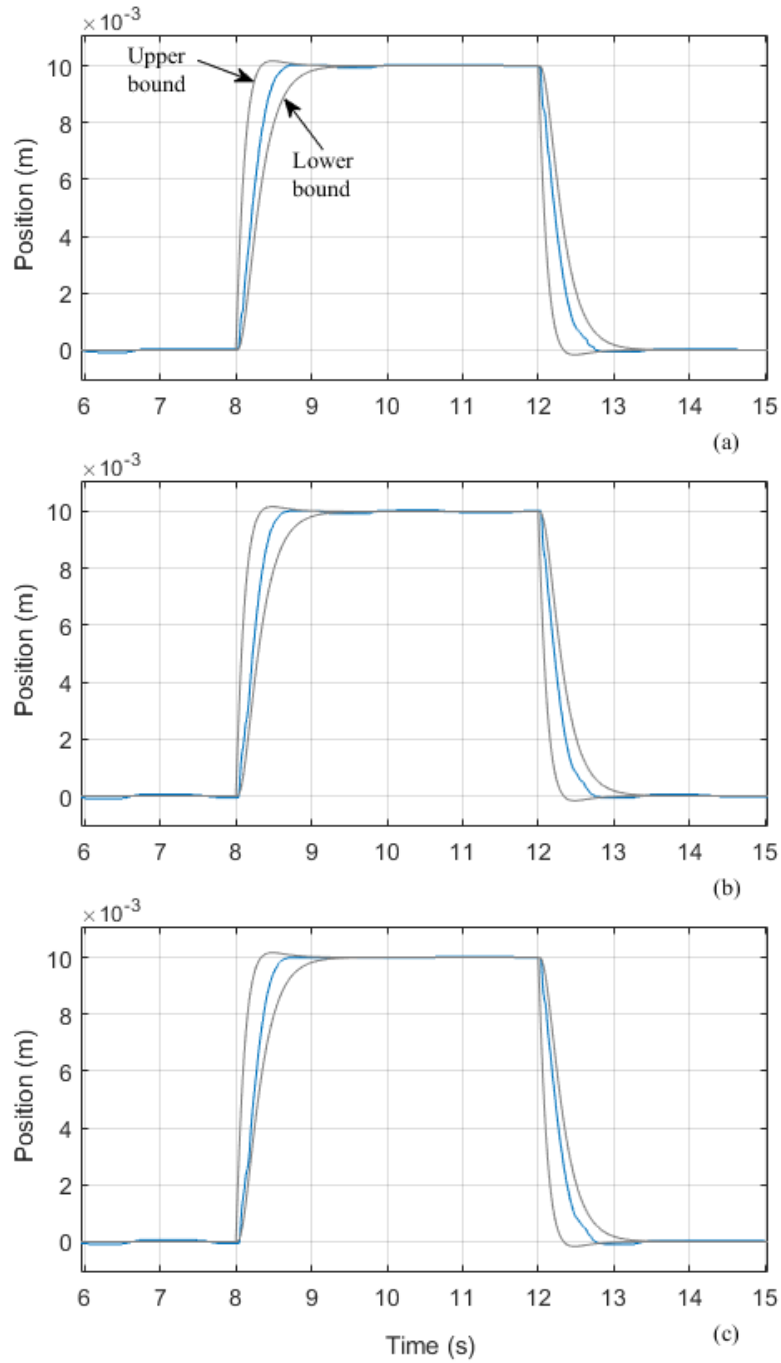


Figure 5.9 Partial enlargements of the position responses shown in Figure 5.8 (a): (a) fourth-order ADRC tuned by the proposed tuning method; (b) second-order ADRC tuned by the proposed tuning method; (c) fault-tolerant controller.

### 5.3 Position Control of Electro-Hydraulic Actuator

Different from the EHA in which the flows are controlled by a servomotor, the electro-hydraulic actuator in which the flows are controlled by a servovalve, is considered in this section. Electro-hydraulic actuators are widely used in the construction and manufacturing industries. Figure 5.10 shows a schematic of the electro-hydraulic actuator. A pressure reducing-relieving valve connected between the pump and the servovalve is used to regulate the supply pressure. A closed-center Moog servovalve is a nozzle-flapper valve. The transfer function of the model of the electro-hydraulic actuator is presented as follows [31]:

$$P(s) = \frac{4k_v w_v^2 \beta A K_f}{(s^2 + 2\zeta_v w_v s + w_v^2) \{ (ms^2 + bs + k)(Vs + 4\beta K_{tp}) + 4\beta A^2 s \}} \quad (5.29)$$

where the parameters in (5.29) are given in Table 5.2.

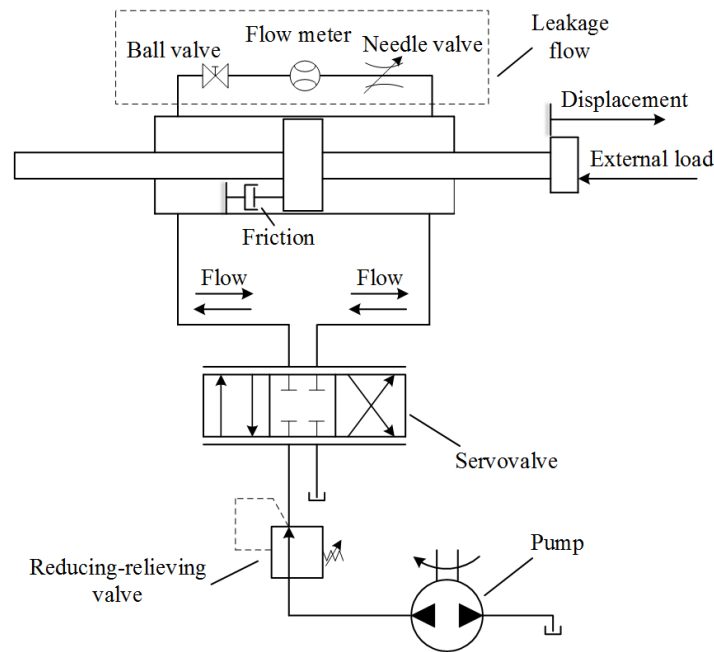


Figure 5.10 Schematic of the electro-hydraulic actuator

Table 5.2 Parameters of the model of the electro-hydraulic actuator

Symbol	Nominal	Range
$k_v(\text{m/V})$	$4.06 \times 10^{-5}$	-
$w_v(\text{rad/s})$	942.48	-
$\zeta_v$	0.7	-
$A(\text{m}^2)$	$6.33 \times 10^{-4}$	-
$m(\text{kg})$	12	-
$b(\text{N} \cdot \text{s/m})$	1000	-
$k(\text{N/m})$	$7.5 \times 10^4$	-
$V(\text{m}^3)$	$4.68 \times 10^{-4}$	-
$K_f(\text{m}^2/\text{s})$	1.02	1.02-1.76
$K_{tp}(\text{m}^3/\text{s} \cdot \text{Pa})$	0	$0-9.5 \times 10^{-11}$
$\beta(\text{Pa})$	$689 \times 10^6$	$550 \times 10^6-895 \times 10^6$

### 5.3.1 Controller Design

It is obvious that tuning the fifth-order ADRC which has eleven observer and controller gains by trial and error is quite difficult. Based on the findings from the previous section, a third-order ADRC rather than a fifth-order ADRC is used to control the electro-hydraulic actuator. The templates that represent the plant uncertainties at the selected frequencies are shown in Figure 5.11. The reference tracking and closed-loop stability specifications for the controller design are:

$$\left\{ \begin{array}{l} \left| \frac{G(jw)P(jw)}{1+G(jw)P(jw)} \right| \leq \delta = 1.06 \\ |T_L(jw)| \leq |T(jw)| \leq |T_U(jw)| \end{array} \right. \quad \forall w \in [0, \infty) \quad (5.30)$$

where

$$T_L(jw) = \frac{4 \times 10^6}{(jw+5)(jw+20)(jw+200)^2}$$

$$T_U(j\omega) = \frac{7.7(j\omega + 5.6)(j\omega + 125)}{(j\omega + 6)(j\omega + 30)^2}$$

The lower bound  $T_L(j\omega)$  has no overshoot with a 2% settling time of 0.85 s. The upper bound  $T_U(j\omega)$  has a 5% overshoot with a 2% settling time of 0.4 s. The stability specification ensures that the system has a 5.77 dB gain margin and 56.29° phase margin.

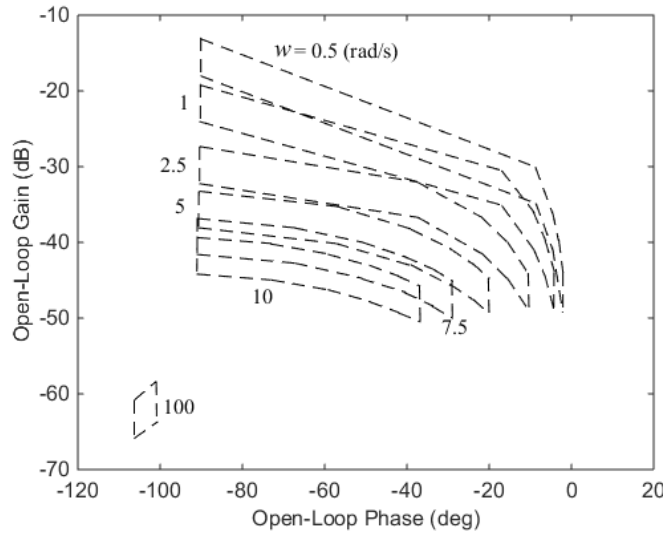


Figure 5.11 Templates of the model of the electro-hydraulic actuator at selected frequencies

The above specifications are then converted to the constraints on the nominal open-loop transfer function. The constraints are represented as the bounds in Figure 5.12. After performing the loop shaping, an acceptable nominal transfer function  $L_n(s)$  is demonstrated in Figure 5.12. The resulting controller  $G(s)$  is determined as follows:

$$G(s) = \frac{4403}{s} \cdot \frac{s^2/462.2^2 + 0.16s/462.2 + 1}{s^2/780^2 + 1.458s/780 + 1} \cdot \frac{(s/4.25 + 1)}{(s/830 + 1)} \quad (5.31)$$



As shown in Figure 5.13, a prefilter  $H(s)$  is designed to make the frequency responses of the closed-loop control system satisfy the tracking bounds. This  $H(s)$  is shown as follows:

$$H(s) = \frac{(s/22 + 1)}{(s/12 + 1)(s/25 + 1)(s/110 + 1)} \quad (5.32)$$

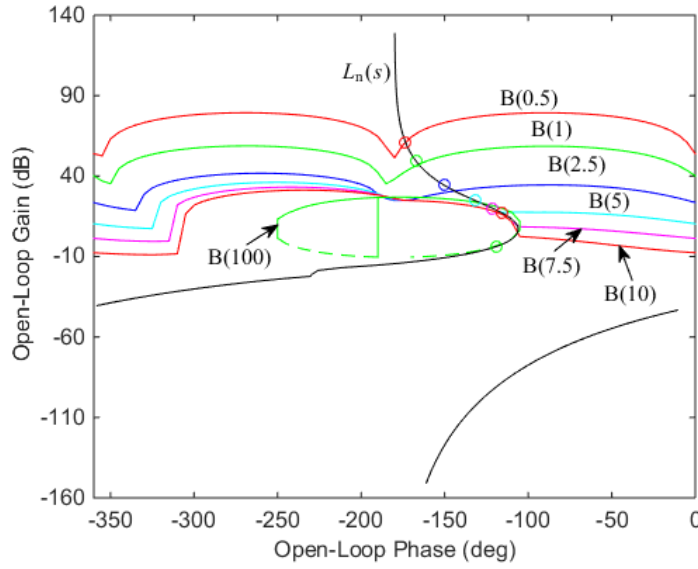


Figure 5.12 Bounds  $B(w)$  and the acceptable nominal open-loop transfer function  $L_n(s)$

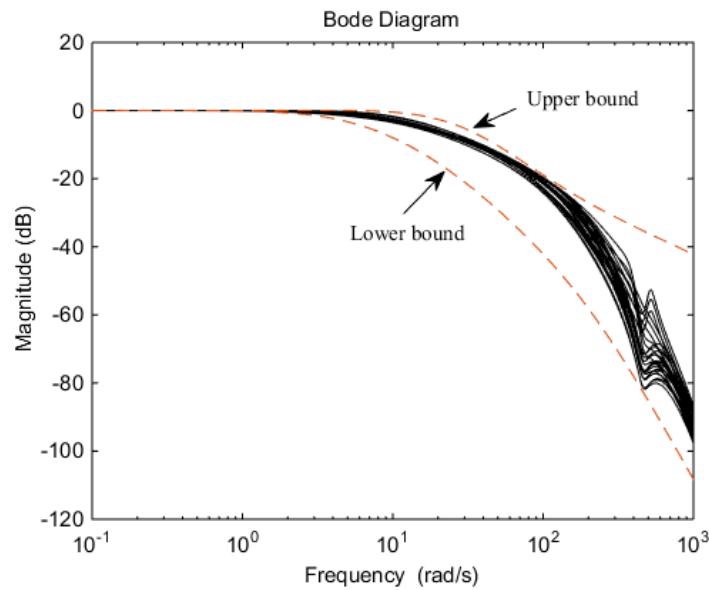


Figure 5.13 Frequency responses of the control system with parametric uncertainties

### 5.3.2 Simulations and Experiments

Simulations are conducted to validate the effectiveness of the resulting controller and prefilter of the third-order ADRC. Figure 5.14 (a) shows the step responses of the third-order ADRC tuned by the proposed tuning method. The uncertain parameters ranges from small to large values in the given ranges. It can be seen that the responses are within the prescribed lower and upper tracking bounds. Figure 5.14 (b) shows the responses of a fifth-order ADRC tuned by the bandwidth tuning method. The observer and controller bandwidths are tuned to  $w_o=4000$  rad/s and  $w_c=210$  rad/s, respectively, to ensure all the responses fall within the tracking bounds. To clearly compare the proposed tuning method with the bandwidth tuning method, simulations using only the nominal parameter values are shown in Figure 5.15. It is shown that: 1) the third-order ADRC tuned by the proposed tuning method has better tracking response than the fifth-order ADRC tuned by the bandwidth tuning method; 2) the control signal in the proposed tuning method varies smoothly, but in the bandwidth tuning method oscillates initially with a maximum voltage of 11 V, which exceeds the hardware output limitation of 10 V and results in an unstable actual response in practice; 3) for the ADRC tuned by the bandwidth tuning method, increasing the bandwidths results in a better tracking performance; however, the control signal oscillates with a larger amplitude.

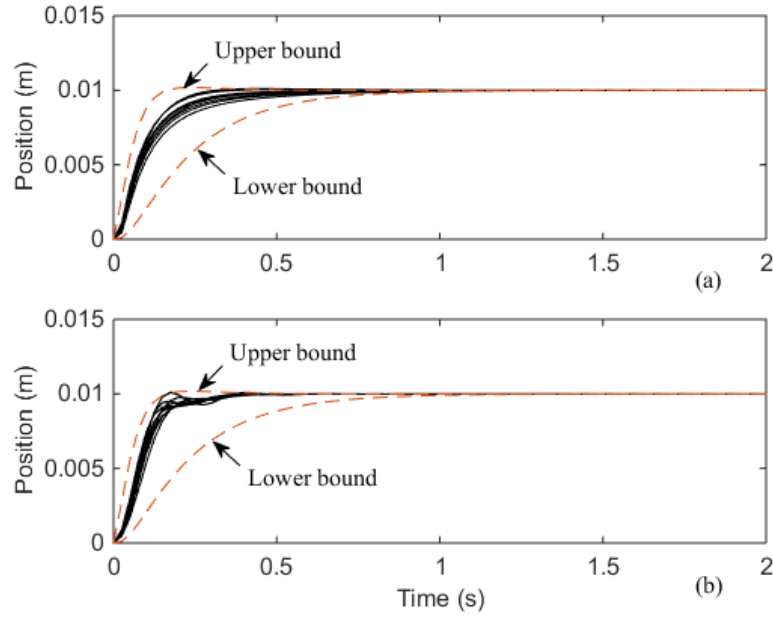


Figure 5.14 Step responses of the control system with parameter variations in simulations: (a) third-order ADRC tuned by the proposed tuning method; (b) fifth-order ADRC tuned by the bandwidth tuning method ( $w_o=4000$  rad/s,  $w_c=210$  rad/s)

The third-order ADRC tuned by the proposed tuning method is tested in the experiment. The internal leakage between the two chambers is also considered. The experimental responses of 0.01 m square-wave against a 125 kN/m spring and increasing leakage flow are shown in Figure 5.16. The partial enlargements (time from 6 s to 15 s) of the position responses shown in Figure 5.16 (a) are demonstrated in Figure 5.17. It is shown that the position response of the actuator controlled by the ADRC falls within the bounds and equally matches the response of the fault-tolerant controller proposed in [31]. In addition, it is noteworthy that the structure of the ADRC is simpler than that of the fault-tolerant controller. Obviously, the ADRC tuned by the proposed tuning method ensures the stability of the control system and guarantees the desired tracking performance. This method yields an easy-to-use and versatile tool for practical applications.

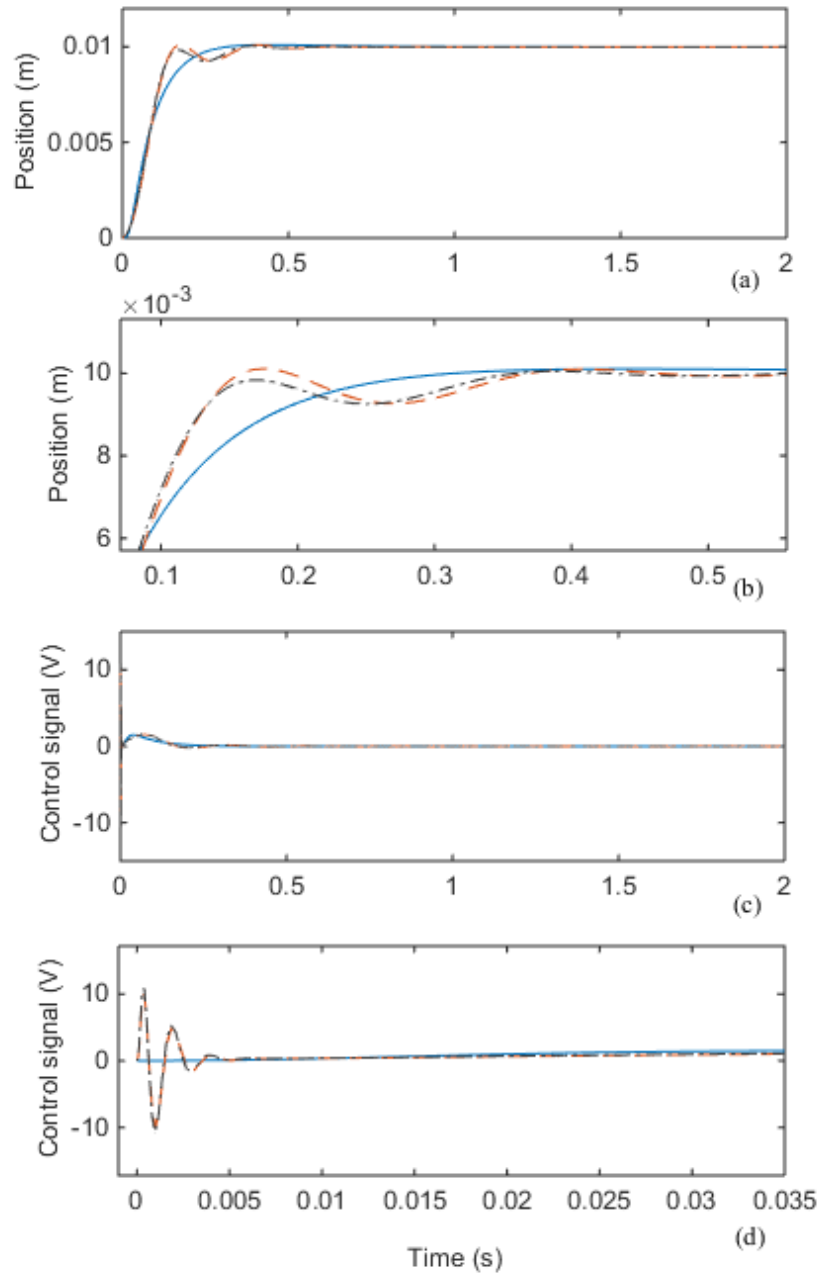


Figure 5.15 Step responses of the control system with nominal parameter values in simulations: (a) step response; (b) partial enlargement of (a); (c) control signal; (d) partial enlargement of (c). (Solid line: third-order ADRC tuned by the proposed tuning method; dashed: fifth-order ADRC tuned by the bandwidth tuning method,  $w_o=4000$  rad/s,  $w_c=210$  rad/s; dash-dotted: fifth-order ADRC tuned by the bandwidth tuning method,  $w_o=4100$  rad/s,  $w_c=215$  rad/s)

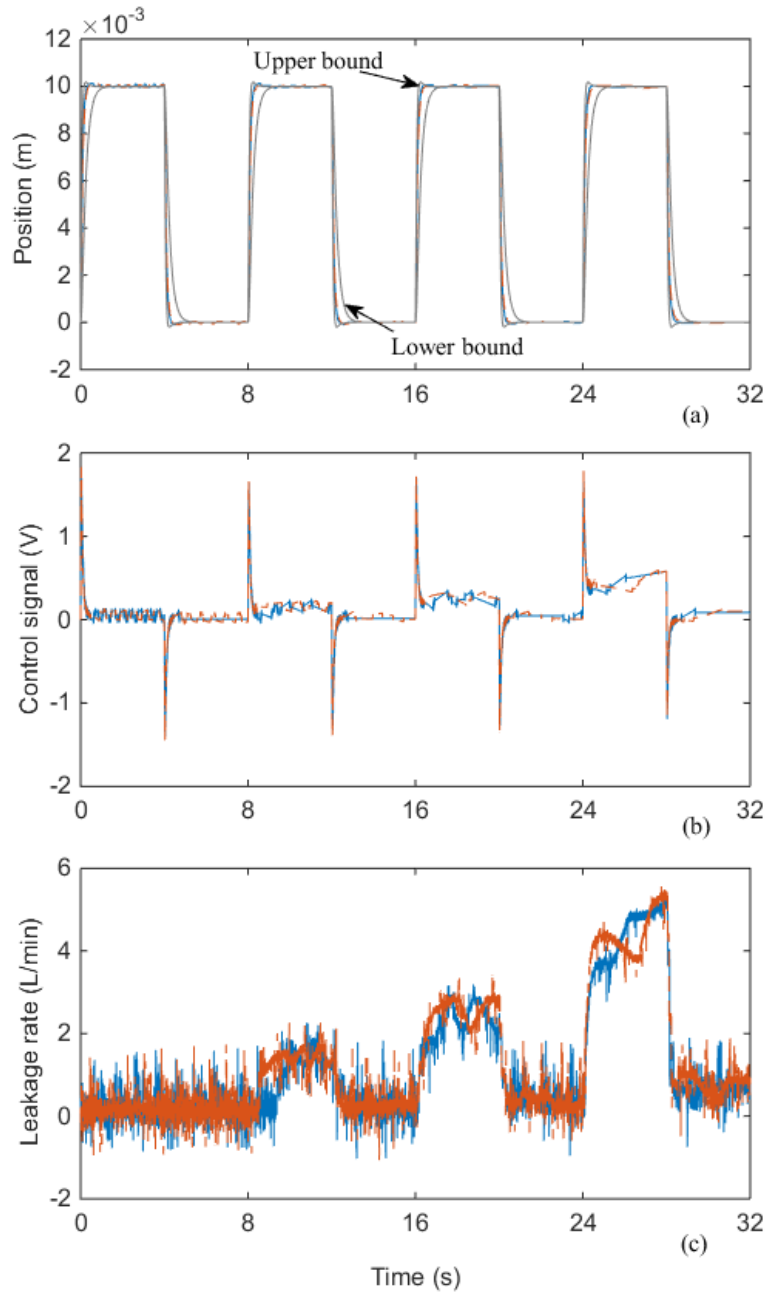


Figure 5.16 Experimental responses of 0.01 m square-wave reference against 125 kN/m spring and increasing leakage flow: (a) position; (b) control signal; (c) leakage rate. (Solid line: third-order ADRC tuned by the proposed tuning method; dashed: fault-tolerant controller)

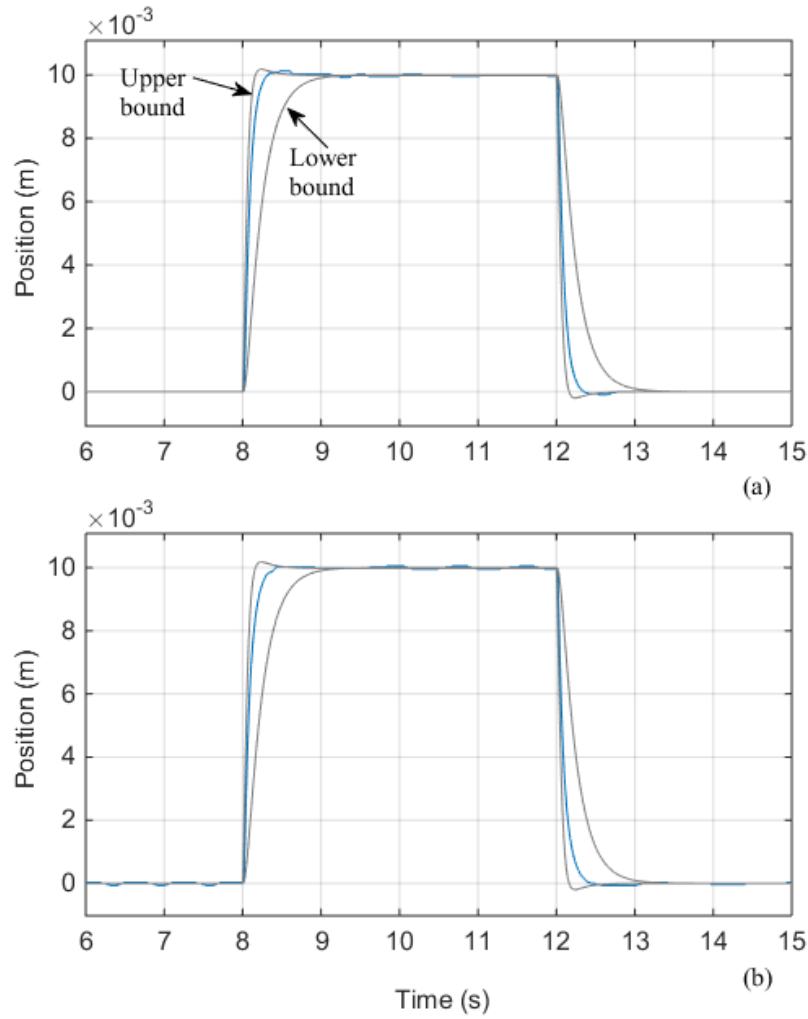


Figure 5.17 Partial enlargements of the position responses shown in Figure 5.16 (a): (a) third-order ADRC tuned by the proposed tuning method; (b) fault-tolerant controller

## 5.4 Summary

The ADRC was designed for the position control of the electro-hydrostatic actuator and the electro-hydraulic actuator, both experiencing internal leakage faults and plant uncertainties. To solve the challenge facing the use of the ADRC for controlling hydraulic actuators described by high-order systems, a new tuning method was proposed to tune the ADRC in the framework of the quantitative feedback theory. In the simulations, the

ADRC tuned by the proposed tuning method satisfied both stability and reference tracking specifications; in contrast, the bandwidth tuning method failed to meet the reference tracking specification. The experimental responses of the hydraulic actuators controlled by the ADRC (tuned by the proposed tuning method) tracked the desired positions closely. The combination of the ADRC and the QFT provides an easy-to-use and effective tool for controller design in practical applications.

# Chapter 6

## Conclusions

### 6.1 Contributions of This Thesis

In this thesis, we explored the application of the ADRC to two new areas: automated steering control for lane keeping in autonomous vehicles, and position control of hydraulic actuators. The challenges facing the use of the ADRC in the above applications were addressed and resolved. The detailed contributions of this thesis are summarized below:

An ADRC controller was designed for the automated steering for lane keeping in autonomous vehicles. It actively estimated the internal dynamics and external disturbances and rejected them in real-time. Additionally, the controller has a simple structure and does not require complex calculations and measurements of the system states, making it easy to implement and effectively improving the system reliability in practice. The stability of the nonlinear vehicle system controlled by the ADRC controller was investigated using the concept of Lyapunov exponents. For the cases of a vehicle running on a straight lane and a curved lane, the control system is exponentially stable



around the equilibrium points. In the simulations, the vehicle controlled by the ADRC controller maintained its position within the lane and the effects of the parameter variations on the lane keeping performance were discussed. Compared to the mass, the tire-road friction, and the look-ahead distance, the longitudinal velocity and the road curvature have larger effects on the lane keeping performance. A scaled vehicle integrated with different hardware was set up to validate the ADRC steering controller. Software involving the control algorithm and a computer vision program was also developed. The experimental results showed that the scaled vehicle performed the lane keeping successfully. In comparison to the PID controller, the ADRC controller is robust against variations in the longitudinal velocity and road curvature.

The ADRC was employed to design robust controllers for the position control of the electro-hydrostatic actuator and the electro-hydraulic actuator. To solve the challenge of tuning the ADRC for the hydraulic actuators described by high-order systems, a new tuning method was proposed to tune the controller parameters in the framework of the quantitative feedback theory. To do so, the ADRC was first transformed to a two degree-of-freedom feedback system structure. Based on the QFT, the decomposed controller and prefilter were designed to meet the stability and reference tracking specifications. The proposed tuning method avoids the tuning difficulty caused by the improper estimation of the observer and controller gains. The simulation results demonstrated that the ADRC tuned by the proposed tuning method satisfied both the stability and reference tracking specifications. In contrast, the ADRC tuned by the bandwidth tuning method failed to meet the reference tracking specification. In the experiments, the hydraulic actuators controlled by the ADRC (tuned by the proposed tuning method) tracked the desired

positions closely. The proposed tuning method yields an easy-to-use and versatile tool for tuning the ADRC for practical applications.

## 6.2 Future Work

The design of the ADRC steering controller and its experimental validation in the scaled vehicle are essential steps for practical implementation in a full-size vehicle. The developed software architecture in this research can be implemented in the full-size vehicle without any change. However, because the real environment of the full-size vehicle could be much more complicated than the experimental environment of the scaled vehicle, certain improvements should be made before the application of the ADRC controller to the full-size vehicle:

- 1) The computer vision program should be improved to avoid failure or improper estimation of the lateral offset caused by complicated road conditions.
- 2) The speed of the full-size vehicle could range from 0 km/h to 100 km/h. To obtain optimal lane keeping performance, a control architecture involving multiple ADRC controllers in which each controller is responsible for a speed range should be investigated.

Second, the proposed tuning method for the ADRC generates an easy-to-use and versatile tool to design the position controllers for hydraulic actuators. Hydraulic actuators are described by linear models. The recommended future work on the tuning method is given as follows:

- 1) The tuning method for the ADRC could be extended to high-order systems described by nonlinear models.
- 2) Because the nonlinear ADRC involving the nonlinear extended state observer and the nonlinear weighted sum has potential to perform better than the linear ADRC [68], the tuning method could be extended to the tuning of the nonlinear ADRC.

# References

- [1] Z. Gao, Y. Huang and J. Han, "An alternative paradigm for control system design," in *Proceedings of Decision and Control Conference*, 2001, pp. 4578-4585.
- [2] W. L. Brogan, *Modern Control Theory*, Upper Saddle River, NJ: Prentice-Hall, 1991.
- [3] S. Zhao, "Practical solutions to the non-minimum phase and vibration problems under the disturbance rejection paradigm," Ph. D thesis, Cleveland State University, 2012.
- [4] Z. Gao, "Active disturbance rejection control: A paradigm shift in feedback control system design," in *Proceedings of American Control Conference*, 2006, pp. 2399-2405.
- [5] K. Erenturk, "Fractional-order  $PI_{\lambda}D_{\mu}$  and active disturbance rejection control of nonlinear two-mass drive system," *IEEE Transactions on Industrial Electronics*, vol. 60, no. 9, pp. 3806-3813, Sept. 2013.
- [6] J. Han, "Control theory: is it a theory of model or control," *Systems Science and Mathematical Sciences*, vol. 9, no. 4, pp. 328-335, 1989. (In Chinese)
- [7] J. Han, "A class of extended state observers for uncertain systems," *Control and Decision*, vol.10, no.1, pp. 85-88, 1995. (In Chinese)
- [8] J. Han, "Auto-disturbance rejection control and it applications," *Control and Decision*, vol.13, no.1, pp. 19-23, 1998. (In Chinese)
- [9] J. Han, "Nonlinear design methods for control systems," in *Proceedings of 14th IFAC World Congress*, 1999, pp. 1531-1536.
- [10] J. Han, "From PID to active disturbance rejection control," *IEEE Transactions on Industrial Electronics*, vol. 56, no. 3, pp. 900-906, Mar. 2009.
- [11] S. Wu, H. Chiang, J. Perng, C. Chen, B. Wu and T. Lee, "The heterogeneous systems integration design and implementation for lane keeping on a vehicle," *IEEE Transactions on Intelligent Transportation Systems*, vol. 9, no.2, pp. 246-263, Jun. 2008.

- [12] W. Kim, Y. S. Son and C. C. Chung, "Torque-overlay-based robust steering wheel angle control of electrical power steering for a lane-keeping system of automated vehicles," *IEEE Transactions on Vehicular Technology*, vol. 65, no. 6, pp. 4379-4392, Jun. 2016.
- [13] Y. S. Son, W. Kim, S. Lee and C. C. Chung, "Robust multirate control scheme with predictive virtual lanes for lane-keeping system of autonomous highway driving," *IEEE Transactions on Vehicular Technology*, vol. 64, no. 8, pp. 3378-3391, Aug. 2015.
- [14] D. E. Williams, "Lane-keeping benefits of practical rear axle steer," *Vehicle System Dynamics*, vol. 52, no. 4, pp. 504-521, 2014.
- [15] H. Imine and T. Madani, "Sliding-mode control for automated lane guidance of heavy vehicle," *International Journal of Robust and Nonlinear Control*, vol. 23, pp. 67-76, Oct. 2011.
- [16] N. M. Enache, S. Mammar, B. Lusetti and Y. Sebsadji, "Active steering assistance for lane keeping and lane departure prevention," *Journal of Dynamic Systems, Measurement, and Control*, vol. 133, no. 6, Sept. 2011.
- [17] S. Chaib, M. S. Netto and S. Mammar, " $H_\infty$ , adaptive, PID and fuzzy control: a comparison of controllers for vehicle lane keeping," in *Proceedings of IEEE Intelligent Vehicles Symposium*, 2004, pp. 139-144.
- [18] R. Marino and S. Scalzi, "Nested PID steering control for lane keeping in autonomous vehicles," *Control Engineering Practice*, vol. 19, pp. 1459-1467, Sept. 2011.
- [19] R. Marino, S. Scalzi and M. Netto, "Integrated Driver and Active Steering Control for Vision-Based Lane Keeping," *European Journal of Control*, vol. 18, no. 5, pp. 473-484, 2012.
- [20] C. J. Taylor, J. Kosecka, R. Blasi and J. Malik, "A comparative study of vision-based lateral control strategies for autonomous highway driving," *International Journal of Robotics Research*, vol. 18, no. 5, pp. 442-453, May 1999.
- [21] J. Guldner, H. Tan and S. Patwardhan, "Analysis of automatic steering control for highway vehicles with look-down lateral reference systems," *Vehicle System Dynamics*, vol. 26, pp. 243-269, 1996.

- [22] E. J. Rossetter and J. C. Gerdes, "Lyapunov based performance guarantees for the potential field lane-keeping assistance system," *Journal of Dynamic Systems, Measurement, and Control*, vol. 128, no. 3, Aug. 2005.
- [23] S. Suryanarayanan and M. Tomizuka, "Appropriate sensor placement for fault-tolerant lane-keeping control of automated vehicles," *IEEE/ASME Transactions on Mechatronics*, vol. 12, no. 4, pp. 465-471, Aug. 2007.
- [24] S. Ibaraki, S. Suryanarayanan and M. Tomizuka, "Design of Luenberger state observers using fixed-structure  $H$ -infinity optimization and its application to fault detection in lane-keeping control of automated vehicles," *IEEE/ASME Transactions on Mechatronics*, vol. 10, no. 1, pp. 34-42, Feb. 2005.
- [25] S. Suryanarayanan, M. Tomizuka and T. Suzuki, "Design of simultaneously stabilizing controllers and its application to fault-tolerant lane-keeping controller design for automated vehicles," *IEEE Transactions on Control Systems Technology*, vol. 12, no. 3, pp. 329-339, May 2004.
- [26] L. Zhao, Y. Yang, Y. Xia and Z. Liu, "Active disturbance rejection position control for a magnetic rodless pneumatic cylinder," *IEEE Transactions on Industrial Electronics*, vol. 62, no. 9, pp. 5838-5846, Sept. 2015.
- [27] Q. Zhang, L. Q. Gao and Z. Gao, "On stability analysis of active disturbance rejection control for nonlinear time-varying plants with unknown dynamics," in *Proceedings of IEEE conference on Decision and Control*, 2007, pp. 3501-3506.
- [28] Q. Zheng, Z. Chen and Z. Gao, "A practical approach to disturbance decoupling control," *Control Engineering Practice*, vol. 17, no. 9, pp. 1016-1025, Sept. 2009.
- [29] G. Ren, M. Esfandiari, J. Song and N. Sepehri, "Position control of an electrohydrostatic actuator with tolerance to internal leakage," *IEEE Transactions on Control Systems Technology*, vol. 24, no. 6, pp. 2224-2232, Nov. 2016.
- [30] G. Ren, J. Song and N. Sepehri, "Fault-tolerant actuating pressure controller design for an electrohydrostatic actuator experiencing a leaky piston seal," *Journal of Dynamic Systems, Measurement, and Control*, vol. 139, no. 6, Jun. 2017.
- [31] M. Karpenko and N. Sepehri, "Fault-tolerant control of a servohydraulic positioning system with crossport leakage," *IEEE Transactions on Control Systems Technology*, vol. 13, no. 1, pp. 155-161, Jan. 2005.

- [32] Z. Gao, "Scaling and bandwidth-parameterization based controller tuning," in *Proceedings of American control conference*, 2003, pp. 4989-4996.
- [33] C. Fu and W. Tan, "Tuning of linear ADRC with known plant information," *ISA Transactions*, vol. 65, pp. 384-393, Nov. 2016.
- [34] W. Tan and C. Fu, "Linear active disturbance-rejection control: analysis and tuning via IMC," *IEEE Transactions on Industrial Electronics*, vol. 63, no. 4, pp. 2350-2359, Apr. 2016.
- [35] C. Borghesani, Y. Chait and Oded Yaniv, *The QFT Frequency Domain Control Design Toolbox User's Guide*, Terasoft, Inc.
- [36] O. Yaniv, *Quantitative Feedback Design of Linear and Nonlinear Control Systems*. USA: Kluwer, 1999.
- [37] N. Niksefat and N. Sepehri, "Designing robust force control of hydraulic actuators despite system and environmental uncertainties," *IEEE Control Systems Magazine*, vol. 21, pp. 66-77, Feb. 2001.
- [38] M. Esfandiari, "Hydraulic Actuator Force Control: Quantitative Design and Stability Analysis," Ph. D thesis, University of Manitoba, 2015.
- [39] [https://www.kbb.com/car-news/all-the-latest/toyota-previews-new-automated-driver\\_assist-systems/2000009775/](https://www.kbb.com/car-news/all-the-latest/toyota-previews-new-automated-driver_assist-systems/2000009775/)
- [40] H. Z. Tan and N. Sepehri, "Parametric fault diagnosis for electrohydraulic cylinder drive units," *IEEE Transactions on Industrial Electronics*, vol. 49, no. 1, pp. 96-106, Feb. 2002.
- [41] Y. Gao, Q. Zhang, and X. Kong, "Wavelet-based pressure analysis for hydraulic pump health diagnosis," *Transactions of the ASAE*, vol. 46, no. 4, pp. 969-976, 2003.
- [42] Z. Mao, B. Jiang, and P. Shi, "Observer-based fault-tolerant control for a class of networked control systems with transfer delays," *Journal of the Franklin Institute*, vol. 348, no. 4, pp. 763-776, May 2011.
- [43] L. Y. Hao and G. H. Yang, "Robust fault tolerant control based on sliding mode method for uncertain linear systems with quantization," *ISA Transactions*, vol. 52, no. 5, pp. 600-610, Sept. 2013.

- [44] L. F. Mendonça, J. M. C. Sousa, and J. M. G. S. da Costa, “Fault tolerant control using a fuzzy predictive approach,” *Expert Systems with Applications*, vol. 39, no. 12, pp. 10630–10638, Sept. 2012.
- [45] M. Karpenko and N. Sepehri, “Robust position control of an electrohydraulic actuator with a faulty actuator piston seal,” *Journal of Dynamic Systems, Measurement, and Control*, vol. 125, no. 3, pp. 413–423, Sept. 2003.
- [46] K. K. Ahn and Q. T. Dinh, “Self-tuning of quantitative feedback theory for force control of an Electro-hydraulic test machine,” *Control Engineering Practice*, vol. 17, no. 11, pp. 1291–1306, Nov. 2009.
- [47] D. Q. Truong and K. K. Ahn, “Self-tuning quantitative feedback theory for parallel force/position control of electro-hydrostatic actuators,” *Proceedings of the Institution of Mechanical Engineers Part I Journal of Systems and Control Engineering*, vol. 223, no. 4, pp. 537–556, Jun. 2009.
- [48] X. Chang, Y. Li, W. Zhang, N. Wang and W. Xue, “Active disturbance rejection control for a flywheel energy storage system,” *IEEE Transactions on Industrial Electronics*, vol. 62, no. 2, Feb. 2015.
- [49] H. Tang and Y. Li, “Development and active disturbance rejection control of a compliant micro-/nanopositioning piezostage with dual mode,” *IEEE Transactions on Industrial Electronics*, vol. 61, no. 3, pp. 1475-1492, Mar. 2014.
- [50] L. M. Belmonte, R. Morales, A. Fernandez-Caballero and J. A. Somolinos, “A tandem active disturbance rejection control for a laboratory helicopter with variable-speed rotors,” *IEEE Transactions on Industrial Electronics*, vol. 63, no. 10, pp. 6395-6406, Oct. 2016.
- [51] N. Lotfi, H. Zomorodi and R. G. Landers, “Active disturbance rejection control for voltage stabilization in open-cathode fuel cells through temperature regulation,” *Control Engineering Practice*, vol. 56, pp. 92-100, Nov. 2016.
- [52] B. Du, S. Wu, S. Han and S. Cui, “Application of linear active disturbance rejection controller for sensorless control of internal permanent-magnet synchronous motor,” *IEEE Transactions on Industrial Electronics*, vol. 63, no. 5, pp. 3019-3027, May 2016.



- [53] H. Sira-Ramirez, J. Linares-Flores, C. Garcia-Rodriguez and M. A. Contreras-Ordaz, "On the control of the permanent magnet synchronous motor: an active disturbance rejection control approach," *IEEE Transactions on Control Systems Technology*, vol. 22, no. 5, pp. 2056-2063, Sept. 2014.
- [54] Y. Xia, F. Pu, S. Li and Y. Gao, "Lateral path tracking control of autonomous land vehicle based on ADRC and differential flatness," *IEEE Transactions on Industrial Electronics*, vol. 63, no. 5, pp. 3091-3099, May 2016.
- [55] A. Rodriguez-Angeles and J. A. Garcia-Antonio, "Active disturbance rejection control in steering by wire haptic systems," *ISA Transactions*, vol. 53, no. 4, pp. 939-946, Jul. 2014.
- [56] Q. Zheng, L. Dong, D. H. Lee and Z. Gao, "Active disturbance rejection control for MEMS gyroscopes," *IEEE Transactions on Control Systems Technology*, vol. 17, no. 6, pp. 1432-1438, Nov. 2009.
- [57] L. A. Castaneda, A. Luviano-Juarez and I. Chairez, "Robust trajectory tracking of a Delta robot through adaptive active disturbance rejection control," *IEEE Transactions on Control Systems Technology*, vol. 23, no. 4, pp. 1387-1398, Jul. 2015.
- [58] C. Zhang, J. Yang, S. Li and N. Yang, "A generalized active disturbance rejection control method for nonlinear uncertain systems subject to additive disturbance," *Nonlinear Dynamics*, vol. 83, no. 4, pp. 2361-2372, Mar. 2016.
- [59] D. Li, P. Ding and Z. Gao, "Fractional active disturbance rejection control," *ISA Transactions*, vol. 62, pp. 109-119, May 2016.
- [60] J. Cortes-Romero, G. Ramos and H. Coral-Enriquez, "Generalized proportional integral control for periodic signals under active disturbance rejection approach," *ISA Transactions*, vol. 53, no. 6, pp. 1901-1909, Nov. 2014.
- [61] S. Zhao and Z. Gao, "Modified active disturbance rejection control for time-delay systems," *ISA Transactions*, vol. 53, no. 4, pp. 882-888, Jul. 2014.
- [62] Q. Zheng and Z. Gao, "Predictive active disturbance rejection control for processes with time delay," *ISA Transactions*, vol. 53, no. 4, pp. 873-881, Jul. 2014.

- [63] W. Xue and Y. Huang, "Performance analysis of active disturbance rejection tracking control for a class of uncertain LTI systems," *ISA Transactions*, vol. 58, pp. 133-154, Sept. 2015.
- [64] G. Herbst, "Practical Active Disturbance Rejection Control Bumpless Transfer, Rate Limitation, and Incremental Algorithm," *IEEE Transactions on Industrial Electronics*, vol. 63, no. 3, pp. 1754-1764, Mar. 2016.
- [65] M. S. Fadali, "On the Stability of Han's ADRC", in *Proceedings of American Control Conference*, 2014, pp. 3597-3601.
- [66] J. Li, X. Qi, Y. Xia and Z. Gao, "On asymptotic stability for nonlinear ADRC based control system with application to the ball-beam problem", in *Proceedings of American Control Conference*, 2016, pp. 4725-4730.
- [67] Q. Zheng, L. Q. Gao and Z. Gao, "On validation of extended state observer through analysis and experimentation," *Journal of Dynamic Systems, Measurement, and Control*, vol. 134, no. 2, Jan. 2012.
- [68] J. Li, Y. Xia, X. Qi and Z. Gao, "On the necessity, scheme, and basis of the linear–nonlinear switching in active disturbance rejection control," *IEEE Transactions on Industrial Electronics*, vol. 64, no. 2, pp. 1425-1435, Feb. 2017.
- [69] A. Wolf, J. B. Swif, H. L. Swinney and J. A. Vastano, "Determining Lyapunov exponents from a time series," *Physica D: Nonlinear Phenomena*, vol. 16, no. 3, pp. 285–317, Jul. 1985.
- [70] V. I. Oseledec, "A multiplicative ergodic theorem: Lyapunov characteristic numbers for dynamic system," *Trans. Moscow Math. Soc.*, vol. 19, pp. 197–231, 1968.
- [71] Y. Sun, "Energy efficient stability control of a biped based on the concept of Lyapunov exponents," Ph. D thesis, University of Manitoba, 2013.
- [72] C. Yang, "Balance control of constrained bipedal standing and stability analysis using the concept of Lyapunov exponents," Ph. D thesis, University of Manitoba, 2007.
- [73] C. Yang and Q. Wu, "Effects of constraints on bipedal balance control," in *Proceedings of American Control Conference*, 2006, pp. 2510-2515.

- [74] Y. Sun and C. Wu, "Stability analysis via the concept of Lyapunov exponents: a case study in optimal controlled biped standing," *International Journal of Control*, vol. 85, no. 12, pp. 1952-1966, Aug. 2012.
- [75] S. Sadri, "On Dynamic and Stability Analysis of the Nonlinear Vehicle Models Using the Concept of Lyapunov Stability," Ph. D thesis, University of Manitoba, 2015.
- [76] S. Sadri and C. Wu, "Stability analysis of a nonlinear vehicle model in plane motion using the concept of Lyapunov exponents," *Vehicle System Dynamics*, vol. 51, no. 6, pp. 906-924, 2013.
- [77] G. Tian and Z. Gao, "Frequency response analysis of active disturbance rejection based control system," in *Proceedings of 16th IEEE International Conference on Control Applications*, 2007, pp. 1595-1599.
- [78] L. Dong, P. Kandula and Z. Gao, "On a robust control system design for an electric power assist steering system," in *Proceedings of American Control Conference*, 2010, pp. 5356-5361.
- [79] S. Mammar and D. Koenig, "Vehicle handling improvement by active steering," *Vehicle System Dynamics*, vol. 38, no. 3, pp. 211-242, 2002.
- [80] R. Rajamani, *Vehicle Dynamics and Control*. Minneapolis, MN: Springer, 2012.
- [81] H. B. Pacejka and E. Bakker, "The Magic Formula Tyre Model," *Vehicle System Dynamics*, vol.21, pp. 1-18, 1992.
- [82] I. D. Landau, T. Airimitoie, A. Castellanos-Silva and A. Constantinescu, *Adaptive and Robust Active Vibration Control*, Switzerland: Springer, 2017.